UNIVERSITY OF OKLAHOMA

GRADUATE COLLEGE

REAL-TIME HYBRID SIMULATION STUDY OF A ROLLING PENDULUM EQUIPMENT ISOLATION SYSTEM

A THESIS

SUBMITTED TO THE GRADUATE FACULTY

in partial fulfillment of the requirements for the

Degree of

MASTER OF SCIENCE

By

BRAULIO A. COVARRUBIAS VARGAS
Norman, Oklahoma
2021

REAL-TIME HYBRID SIMULATION STUDY OF
A ROLLING PENDULUM EQUIPMENT ISOLATION SYSTEM

A THESIS APPROVED FOR THE
SCHOOL OF CIVIL ENGINEERING AND ENVIRONMENTAL SCIENCE

BY THE COMMITTEE CONSISTING OF

Dr. Philip Scott Harvey Jr., Chair

Dr. Jeffery Scott Volz

Dr. James M. Ricles

© Copyright by BRAULIO A. COVARRUBIAS VARGAS 2021
All Rights Reserved.

Para mis padres, Hugo y Epi por siempre apoyarme, creer y confiar en mi.
Para Hugo, Valeria y Doria.
To my OU family.

Acknowledgements

I would like to thank and recognize the support, guidance and mentorship of Dr. Philip Scott Harvey Jr. for the completion of this project, as well as Drs. James Ricles and Jeffery Volz for the positive feedback shared for the last draft of these pages.

I would also like to recognize the help provided before, during and after testing by Liang Cao, Safwan Al-Subaihawi, Tommy Marullo, Darrick Fritchman, and the rest of the staff at the NHERI Engineering Facility and ATLSS Engineering Research Center at Lehigh University.

The experimental testing was performed at the NHERI Lehigh Experimental Facility, whose operation is supported by a grant from the NSF under Cooperative Agreement Nos. CMMI-1520765 and CMMI-2037771.

This material is based upon work supported by the National Science Foundation under Grant Nos. CMMI-1663376, OIA-1929151, and CMMI-1943917.

Table of Contents

List of Figures

List of Tables

Abstract

Damage caused by earthquakes to buildings and their contents (e.g., sensitive equipment) can impact life safety and disrupt business operations following an event. The resulting social and economic losses can be minimized, or even eliminated, by reducing the seismic forces on building contents through vibration isolation. Floor isolation systems (FISs), in particular, are a promising retrofit strategy for protecting vital building contents. In this study, real-time hybrid simulation (RTHS) is utilized to validate mathematical models of isolation systems that incorporate multi-scale (building-FIS-equipment) interactions. For this, an experimental setup representing one bearing of a rolling pendulum (RP) based FIS is studied—first through characterization tests and then through RTHS. RHTS allows for numerically compensating for the extra mass in the experimental setup (m) through the equation of motion's integration in MATLAB scripts and Simulink models. A series of both type of tests were conducted at the Natural Hazards Engineering Research Infrastructure (NHERI) Experimental Facility at Lehigh University. Multiple excitations were used to study the experimental setup under uni-axial loading. In total, 240 tests among characterization and RTHS were performed. Details of the experimental testbed and test protocols for the characterization and RTHS tests are presented, along with results from these tests focused on the effect of enhanced damping on the rolling surface of a bearing, the FIS-equipment and building-FIS interactions and rigorous evaluation of different RP isolation bearing designs through RTHS. All in all, it was found that the most optimal RP bearing configurations are those with coated with elastomeric rubber and higher tributary mass. For isolated equipment with a

frequency of its own, it was found that the bearing's performance was affected for low-frequency equipment (i.e., 1 and 2 Hz at the base of the equipment). On the other hand, the effects of a FIS composed of 350 bearings and accounting for 5% of the structural floor mass were found to be negligible on the building studied (i.e., 3-story moment resisting frame).

Chapter 1
Introduction

1.1 Overview

Earthquakes can heavily damage civil structures causing great economic and, in the worst cases, human losses. Several design strategies have been developed to minimize and mitigate the impact of the forces these natural hazards put on structures. For instance, base isolation systems mitigate the inertial loads caused by an earthquake excitation and, ultimately, reduce floor and structural sidesway (Warn and Ryan, 2012). Floor isolation systems (FISs) are gaining popularity over base isolation systems as they have shown to be a valuable retrofitting approach for protecting vital building contents and the post-event functionality of the structure.

FISs are designed under the premise that an object (e.g., telecommunications apparatus, a raised floor of a building, etc.) can be decoupled (isolated) from the rest of a structure and its respective disturbances (see Figure 1.1). Thus, these systems decrease the transmitted vibrations and ultimately protect the sensitive objects from damaging effects. A system of rolling pendulum (RP) isolation bearings* can comprise a FIS. RP-based isolation systems were first patented in the 19th century. Touaillon (1870) arranged a ball in-between two counter facing spherical surfaces. The theory under which this first rolling isolation system for a building was developed is simple; the ball

*Let it be noted that "isolator unit," "isolation bearing," "unit," and "bearing" are used interchangeably to refer to the same thing in this thesis.

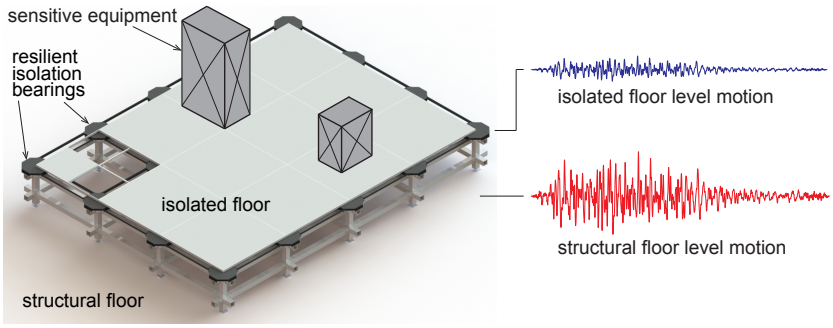

Figure 1.1: Floor isolation system utilizing RP bearings to protect sensitive equipment from harsh structural floor level motions.

comprised between the plates acts like a pendulum (Harvey and Gavin, 2013). Since then, other models have been designed under the same premise: The restoring force is proportional to the mass of the system, while the natural period is independent of this—unlike spring-based isolation systems (Harvey and Kelly, 2016).

Besides innovative design strategies, state-of-the-art testing techniques play an important role in the study of earthquakes and their effects on buildings' structural and non-structural elements. Real-time hybrid simulation (RTHS) has shown to successfully overcome limitations related to more traditional methods like shake-table testing, specifically those related to test specimen sizes and their economic constraints (Mahin and Shing, 1985). RTHS is an innovative, cost-effective, and efficient testing technique that was first developed in the mid-1970s in Japan (Takanashi et al., 1975). While some seismic simulation techniques use either analytical models or experimental methods because of size and computational capacity constraints, RTHS was developed to combine both experimental and analytical tools into a single simulation technique (Nakashima, 2020). Furthermore, as its name implies, RTHS is intended to be performed in real-time, which is critical for rate-dependent systems. Although this can translate to further challenges and limitations, a thorough understanding of this technique's fundamental procedure and a proper configuration of an experimental system can account for these, making RTHS a viable testing alternative for the study of RP-based FISs.

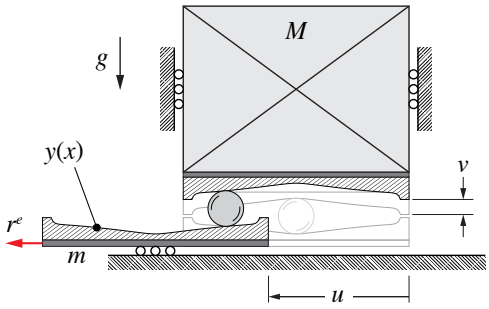

Figure 1.2: Schematic for an idealized RP unit for dynamic analysis

For this project, a RP isolator unit of a FIS like the one shown in Figure 1.1 will be studied. Characterization and RTHS tests are proposed to calibrate and validate mathematical models of the RP isolation unit. An evaluation of the effect of enhanced damping is also to be researched, as well as multi-scale interactions between the proposed system and both the mission-critical equipment being isolated and the building in which the isolation system is installed.

The experimental setup designed to characterize a RP unit is made up of two counter facing concave rolling surfaces and a steel ball rolling in-between these. The top rolling surface is constrained to move only vertically (v) while the lower one is to do so only horizontally (u). Due to their concavities, a vertical displacement is induced in the top surface given a horizontal displacement in the lower one. An idealized schematic is presented in Figure 1.2. Experimental validation of physics-based mathematical models of this type of RP isolation bearing through RTHS has never been performed, for which a full and thorough evaluation and recommendations for improvements are expected.

1.2 Literature Review

The testing of a single rolling pendulum (RP) isolation unit through a series of real-time hybrid simulation (RTHS) tests has no precedent. However, there is extensive work around the different components of this innovative approach. Specifically, RP and friction pendulum (FP) isolation systems have gained relevance over the last 30 years

because of the simplicity of the theory behind them. Moreover, interactions between equipment and isolation systems have previously been studied too. With regards to RTHS, there is evidence backing up that it is highly effective, cost-efficient, relatively new technique adequate to account for inertial effects of non-linear RP bearings. Further applications, design guidelines, recommendations, and areas of improvement have been extensively discussed for large-scale RP and FP isolation too.

1.2.1 Isolation Systems

The concept of building isolation was thought about more than one hundred years ago. The first-ever system was a double concave rolling ball bearing and dates back to 1870 in San Francisco, CA (Warn and Ryan, 2012). While rolling isolation systems were conceptualized before other isolation techniques—namely sliding bearing isolation and elastomeric isolation—its research and development was slower to mature (Harvey and Kelly, 2016).

While base isolation is an accepted approach for earthquake protection, equipment and floor isolation systems (FISs) are gaining popularity as alternative methods to mitigate earthquake hazards on critical equipment (Jia et al., 2014). In order to isolate entire buildings, larger loads and isolator units need to be considered—making its testing both physically and economically challenging. Generally, it has been found that the challenges pertaining to FISs are related to providing enough capacity to meet the isolated body's acceleration and displacement demands caused by ground excitation. As well, the non-linear behavior, the high stress concentration on these systems, and the need for supplemental damping to meet those demands are factors needing investigation in this realm of isolation.

Typically, both FP and RP isolation systems, due to their hardware configuration and their pendulum-like behavior, are considered within the context of sliding bearing isolation systems (Warn and Ryan, 2012). However, it is of interest here to compare

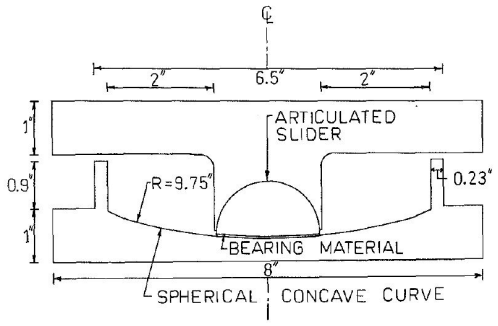

Figure 1.3: Friction Pendulum Bearing basic configuration. Source: Mokha et al. (1991)

and contrast these as to understand their applicability relevant to FISs.

1.2.1(a) Sliding Bearing Isolation

Sliding or FP isolation is defined as a bearing resting on a sliding surface which supports the weight of a body to be isolated. Apart from elastomeric devices, FP isolation is the most widely accepted and used base isolation technique (Deringöl and Güneyisi, 2019). The interaction between these—sliding surface and isolated weight—develops a restoring force opposite to the seismic motion which causes sliding friction and, ultimately, dissipates energy. At its most basic configuration, a FP bearing is comprised of a concave surface, a concave slider and a bearing material (typically coated) inducing friction between these, as presented by Mokha et al. (1991) and shown in Figure 1.3. Several sliding bearing isolation systems have been developed and experimentally studied in more recent years.

Other innovative approaches to FP isolator units have also been adopted. Sarlis and Constantinou (2016) developed a triple-friction pendulum in which sliding friction would appear at three different levels in an attempt to optimize the resistance given by it. A free-body diagram of the components of this type of FP unit is shown in Figure 1.4. This system was analytically modeled and dynamically analyzed. It was proven that it could be used for special cases of unusual friction combinations and showed that the inertial effects of the moving parts were significant to the analysis performed.

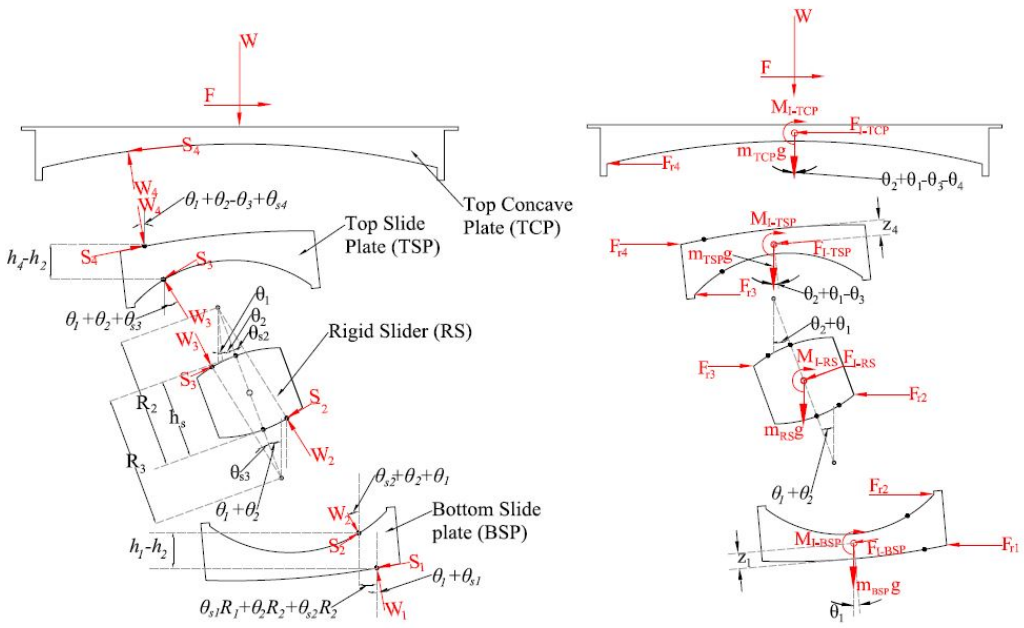

Figure 1.4: Free-body diagrams of components of a triple friction pendulum bearing. Source: Sarlis and Constantinou (2016)

Similar double FP units have also been studied by Fenz and Constantinou (2006). It was determined that for non-special cases a simple FP bearing is equally reliable as the double and triple FP bearings (Fenz and Constantinou, 2006).

Besides analytically studying their hardware configuration and characteristics, FP bearings have been extensively modeled, tested, and applied for earthquake resilience of buildings and bridges. For these superstructures, it has been shown that the isolated structure's fundamental period is dependant on the curvature of the sliding surface of a FP bearing and independent to the mass resting on it. It was also demonstrated that isolators with larger periods resulted in larger displacement demands, and consequently required increases in energy dissipation capabilities for large scale structures (Deringöl and Güneyisi, 2019).

Further studies on the performance of FP isolation have been done involving non-linear structures aiming to understand specific effects. Almazán and Llera (2003) did this by evaluating large deformations, sticking, uplifting, and impact. To adapt their

FP model, they added gap elements and tested their bearings on a 4-story building and a R/C bridge spanning 120 m. Implementing a Park-Wen model was proven to be an effective way of replacing the experimental Coulomb friction of the slider (Almazán and Llera, 2003). More literature points to successful implementation of hysteretic models for isotropic behavior of FISs. For instance, a revised version of the Park-Wen model, the Bouc-Wen model, has shown to be highly efficient for non-linear hysteretic dampers (Solovyov et al., 2017) for bi-axial hysteresis (Harvey and Gavin, 2014).

FP isolator units have successful been studied for building and bridge base isolation. FP isolator units have characteristics and properties similar to the ones of interest for the proposed RP isolator unit—like their restoring capability, influence of the rolling surface's friction, non-linear behavior, etc. However, adapting FP bearings to isolation of smaller systems (i.e., FISs) has been challenging. This is especially true for protecting sensitive equipment since these have threshold accelerations (usually small) to ensure their post-event functionality. Because of the FP bearings friction-slope relations, producing small accelerations requires small slopes in the concave surfaces. At the same time, small slopes relate to the presence of substantial residual deflections, making FP bearings not suitable for this type of FIS. Alternatively for damping, RP isolator units rely on rolling resistance rather than sliding friction coefficient—the former being significantly smaller than the latter—and thus, adapting better to smaller residual displacements. All in all, there are interesting takeaways from previously modeled and experimentally tested RP bearings, like implementing Bouc-Wen (Bouc, 1971; Harvey and Gavin, 2014) models for representing hysteric behaviors.

1.2.1(b) Rolling Bearing Isolation

RP bearings were the first-ever base isolation systems implemented in base isolation of structures. Since then, their study and implementation for base isolation has been proven to be efficient and has expanded to FISs. Rolling isolation systems are similar

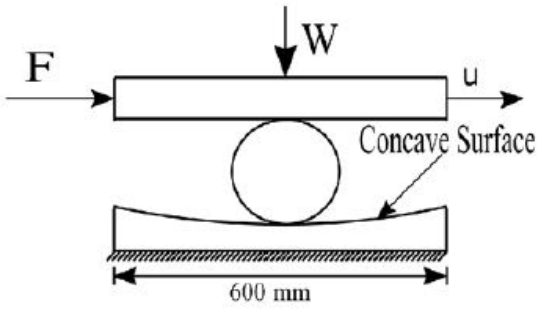

Figure 1.5: Basic configuration of a single concave RP isolator unit. Source: Cilsalar and Constantinou (2019)

in behavior to FP-based systems. The main difference between these is that damping for the former relies on its rolling resistance while the latter's does so on its sliding friction. The components of a basic single RP isolator unit (see Figure 1.5) are two rolling surface and a ball or cylinder in between these (Cilsalar and Constantinou, 2019).

The single concave surface has been studied to optimize its configuration (Wang et al., 2017). A conical surface was developed (see Figure 1.6), in which the middle portion of the rolling surface is concave and the rest has a constant slope. Wang et al. (2017) demonstrates that the shape difference causes a different force-displacement relationships too. On the one hand, it was found that the residual displacements of the conical configuration are smaller thus improving its serviceability as per ASCE 7-16 (ASCE, 2017). On the other hand, the concave configuration is attractive as it produces lower shear forces than the conical one. Other bearing configurations in which neither plate is flat have also been developed and studied. Positive aspects of this include more rolling area available in less horizontal space, while some negative arguments against double concavity indicate the presence of greater torsional effects (Cilsalar and Constantinou, 2019).

Similarly to FP bearings, RP ones have been extensively studied for base isolation. For instance, a double concave bearing was shown to effectively reduce structural

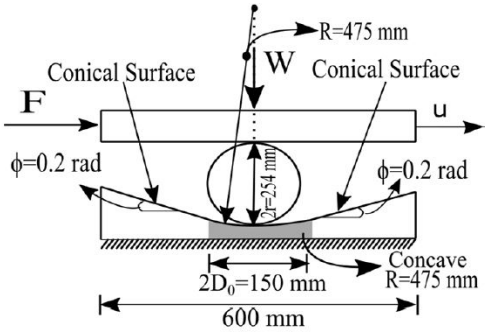

Figure 1.6: Conical configuration of a single RP isolator unit. Source: Cilsalar and Constantinou (2019)

displacement response compared to bare frame testing (Vargas and Bruneau, 2009). Moreover, several applications have been developed related to FISs and the protection of non-structural components.

Ismail et al. (2010) described the development of a novel isolation system—static dynamics interchangeable-ball pendulum system (SDI-BPS)—that is both physically and mathematically suitable for safeguarding vibration sensitive equipment during earthquakes. The design of this bearing is shown in Figure 1.7, and consists of one upper and one lower concave surface, several supporting steel balls, housing holes for said balls, and a damped steel ball. The supporting balls with relatively low rolling resistance stabilize the system under static loading and small isolator displacements. The larger damped ball is to provide the gravitational restoring force under larger displacements and dynamic loading. The SDI-BPS was subjected to tri-axial shake-table testing for three earthquake records. It was conclusively described as a good tool to protect sensitive equipment. It efficiently rectified some of the usual drawbacks associated to RP bearings like "little damping provided by the system, highly concentrated stress produced by the rolling ball due to the small contact area between the rolling ball and scratches and damage to the concave surfaces caused by the ball motions during earthquakes" (Ismail et al., 2010).

Another approach to improving the performance of these RP isolator units was stud-

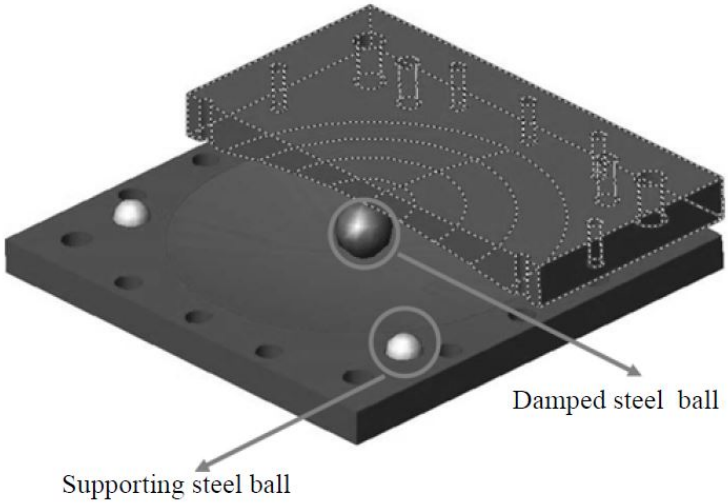

Figure 1.7: Schematic of a SDI-BPS bearing. Source: Ismail et al. (2010)

ied by Harvey et al. (2014) in which a double conical configuration was modeled and validated. To increase the rolling resistance of the system, viscoelastic layers were bonded to both surfaces. The validation of this model was given for a "lightly damped" and a "heavily damped" configuration. The design spectrum for 20 random initial conditions of each configuration was compared to the design spectra at ground ($z/h = 0$), mid-height ($z/h = 0.5$) and roof ($z/h = 1$) levels as per ASCE 7-10 (ASCE, 2010). The "heavily damped" configuration performed better for non-ground levels, effectively meeting the displacement demands of mid-height and roof levels for periods over 2.5 and 4 s, respectively.

Based on the recommendations made by Harvey et al. (2014), a parametric analysis of the effect of the aforementioned viscoelastic layers is proposed for this project. Additionally, while some challenges of RP-bearing FISs have been thoroughly studied and rectified, there is room for advancement in the understanding of FISs' multi-scale interactions by implementing RTHS testing.

1.2.2 Real-Time Hybrid Simulation

Real-time hybrid simulation is a suitable technique for large structure, multi-axial testing. It combines analytical and physical approaches to model and test structures and could be used to study FISs. However, as discussed in Section 1.2.1(b), little to no literature was found related to the implementation of such tests for FISs.

RTHS is a relatively new testing technique, which can potentially help overcome the issues involved in full-scale shake-table testing of isolation systems comprised of RP isolator units. In its early stages, the development of RTHS testing took place in Japan. After a successful United States-Japan collaborative research project, this technique has become increasingly popular worldwide for showing a wide variety of applications in the field of earthquake engineering. Its theoretical basis comes from hybrid simulation, which in turn was developed from quasi-static testing. The idea behind this technique is to numerically compute the displacement response to a quasi-statically imposed specified dynamic excitation. Using analytically established characteristics of the system or structure (i.e., viscous damping and prescribed inertia), hybrid simulation allows for inputting command displacements and outputting restoring forces, which are then added to the next displacement to be imposed using numerical integration algorithms (Mahin and Shing, 1985). Figure 1.8 shows the explicit Newmark algorithm used for the first hybrid simulation tests.

Hybrid simulation testing was proven to be an effective alternative to shake-table testing. This led to improving this testing technique by implementing a dynamic actuator, a digital displacement transducer and a digital servo-mechanism, until developing what is know today as RTHS. The first ever RTHS test was performed using a single degree-of-freedom (DOF) system and a viscous damper (Nakashima et al., 1992). The sub-structuring capabilities of RHTS allowed for analytically modeling the single DOF structure while experimentally testing only the viscous damper. The test was demon-

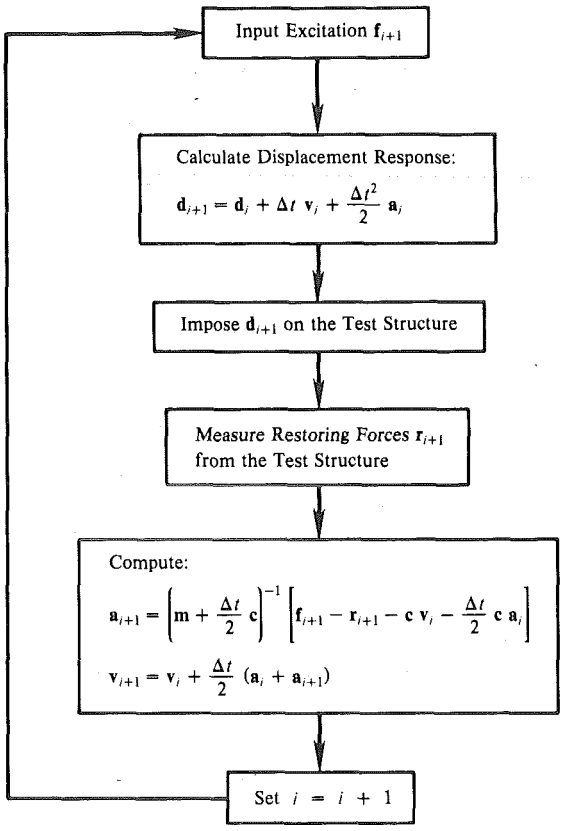

Figure 1.8: Explicit Newmark algorithm used in the first hybrid simulation tests in Mahin and Shing (1985)

strated to be accurate and reliable, so RTHS has been refined for different purposes ever since.

Some majors areas of improvement for RTHS were related to the actuator's delay. These were studied in Horiuchi et al. (1999), in which a model predicts a displacement based on an extrapolation of previous and present displacements. This method was shown to be reliable while showing that the delay effect must be considered in a case-by-case basis, as each actuator has its own response delay, which can destabilize the integration algorithm or show inaccurate predictions.

Other authors have developed unconditionally stable algorithms based on explicit expressions of displacement and velocity. Chen and Ricles (2008) posit that their CR algorithm for a single DOF with positive viscous damping yields zero algorithmic damp-

ing. In Chen et al. (2009), such algorithm was successfully applied to RTHS when testing single and multiple DOF structures with a passive elastomeric damper subjected to earthquake ground motions. The results show that their algorithm remains unconditionally stable for linear-elastic and nonlinear structures with softening behavior, as well as conditionally stable for nonlinear structures with stiffening behavior. Thus, the implementation of this algorithm or more recent advancements (Kolay and Ricles, 2019) for the proposed RTHS FIS tests seems feasible.

With regards to the implementation of RTHS for isolation systems, Shao and Griffith (2013) compile a series of tests in which RTHS is implemented in Network for Earthquake Engineering Simulation (NEES) projects. However, the tests listed by Shao and Griffith (2013) include magneto-rheological (MR) fluid dampers, FP bearings and a base isolation system—not a single RP isolation system was reported to be tested. At last, the implementation of RTHS on a variety of seismic resilience tests provide a broad insight into the capabilities of using such technique to test base isolation systems.

In more recent years, RTHS was successfully applied to FISs using MR dampers in the ninth floor of a fourteen-story building (Zhang et al., 2017). The MR dampers were modeled and then evaluated, similarly to the RP isolator units project herein proposed. Moreover, the RTHS sub-structuring capabilities were demonstrated to be accurate for evaluating large-scale experimental specimens as a substructure of an even larger structural system. Thus, the study of RP-based FISs, as per Zhang et al. (2017), has promising areas of opportunity through the implementation of RTHS tests.

1.3 Summary

Sensitive equipment can be heavily damaged by seismic activity. FISs are gaining popularity to protect non-structural components versus the more classical base isolation. From these, RP isolation bearings are an effective retrofitting technique for safeguarding such equipment, but additional research is needed.

Typically, economical limitations have allowed for scaled-down experimental studies of RP isolation bearings. RTHS tests have efficiently overcome such limitations for large-scale base isolation and is expected to be equally successful for testing RP isolator units. RTHS testing of the proposed RP-based FIS will allow for gaining a better understanding of the underlying physics of RP isolation units with enhanced damping. By doing so, the testing and model validation herein proposed will, ultimately, enable for simulations of uni-axial RP-based FISs.

Chapter 2
Experimental Setup

2.1 Overview

This chapter describes the testing facilities and the experimental setup designed and developed to represent a rolling pendulum (RP) isolator unit. The unit is comprised of two conical steel rolling surfaces (upper and lower) and a steel ball in-between these. A detailed depiction of the physical characteristics of the rolling surfaces as well as the rest of the assembly is given in this chapter. An array of sensors were implemented in the setup to measure and record load, acceleration, and displacement data. The experimental setup and facilities discussed in this chapter were used for the tests in Chapters 3, 4 and 5.

2.2 Testing Facilities

The design and fabrication of the test specimen took place at the Donald G. Fears Structural Engineering Laboratory at the University of Oklahoma. The design was revised and subjected to characterization and real-time hybrid simulation (RTHS) tests at the National Hazards Engineering Research Infrastructure (NHERI) Experimental Facility (EF) at Lehigh University. The NHERI Lehigh EF has world-class state-of-the-art equipment able to perform real-time hybrid simulations involving large-scale physical models and computer-based numerical simulations (Cao et al., 2020). These capabilities were implemented in a novel approach for full-scale testing of a RP isolator unit.

2.3 Experimental Setup

To study a floor isolation system (FIS), an experimental system was designed to characterize and replicate the behavior of a RP isolator unit subjected to uniaxial lateral loading (see Figure 2.1). By studying a single unit through RTHS tests, it is attempted to simulate and understand the behavior of a FIS comprised of multiple of these units when loaded laterally (see Figure 2.2 for a FIS comprised of four units).

A single RP isolator unit is made up of two conical steel plates (upper and lower) and a steel ball that rolls between these. The proof mass represents a tributary load on one isolator unit. The lower rolling surface is constrained to move only horizontally while the upper is to do so vertically by horizontal and vertical guides, respectively. Due to said constraints and the rolling surfaces' geometry, a horizontal displacement in the lower of these causes a vertical displacement in the upper one.

The rolling surfaces are based on the ball-n-cone design used in the ISO-Base platform manufactured by WorkSafe Technologies. The upper and lower rolling surfaces are identical in shape as shown in Figure 2.3. Nominally, each rolling surface is 10.5 by 10.5-in. with a centered conical section of approximately 7-in. in diameter. In this conical section, the outermost regions have a 1:10 slope that combines with a spherical center region with a 5-in. radius. Given this geometry, the displacement relation

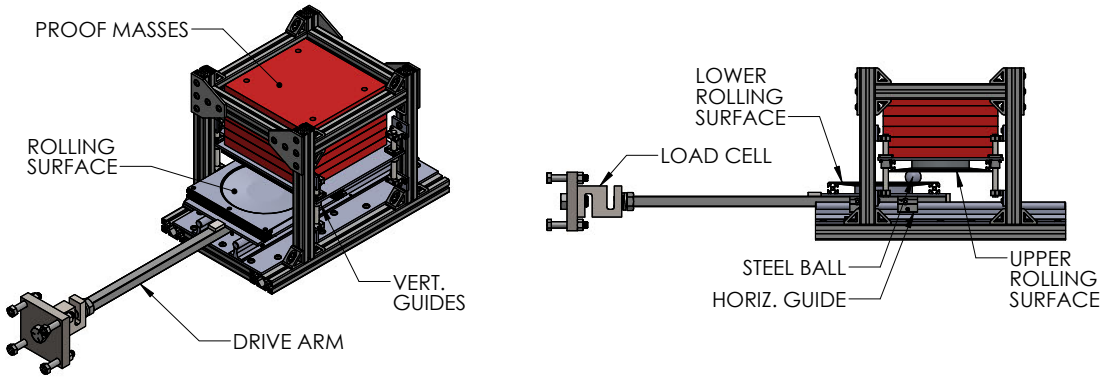

Figure 2.1: Setup used for real-time hybrid simulation tests of a single rolling pendulum bearing.

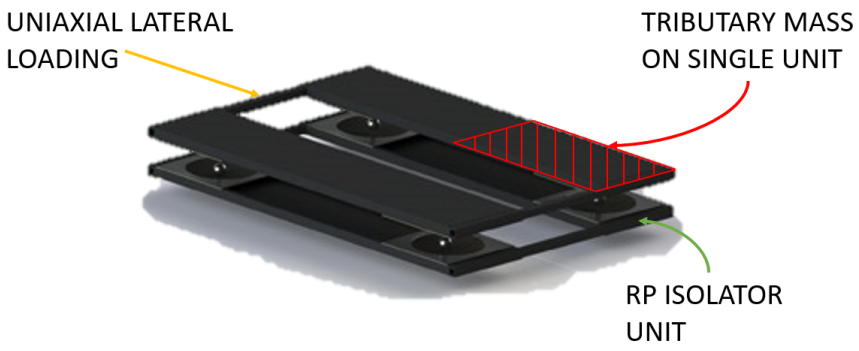

Figure 2.2: ISO-Base assembly of a FIS comprised of 4 RP isolator unit

between the both upper and lower rolling surfaces allows for a maximum horizontal displacement of approximately 7 in. and a maximum vertical displacement of approximately 3/4 in.

To assure the rolling surfaces were properly connected and constrained, each was attached to an assembly, and a frame setup (see Figure 2.6) was built around the isolator unit, to interface the lower and upper assemblies. Each of the rolling surfaces was attached to an aluminum plate through 1-in. T-slotted framing rails along two edges (see Figures 2.4 and 2.5). A hard plastic puck was inserted between the rolling surface and the aluminum plate to provide support at the rolling surface's center. The lower

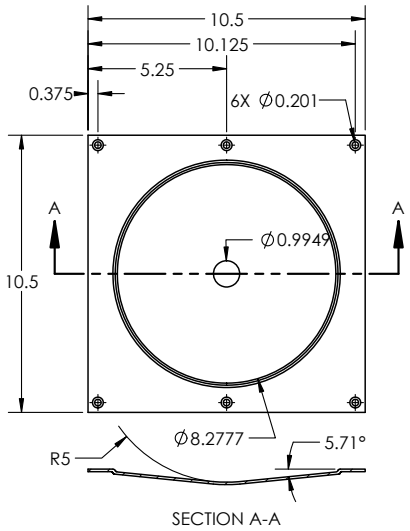

Figure 2.3: Drawing of the conical rolling surface used in the RP isolator unit. (units: in.)

assembly (see Figure 2.4) constrains the lower rolling surface to move horizontally only via four linear motion carriages bolted to the underside of the aluminum plate. These carriages move along two horizontal rails that are bolted to an aluminum plate that is supported by 1.5-in. T-slotted aluminum framing rails on its perimeter forming a rigid base. These rails also serve to support another set of aluminum rails that carry the four vertical guides, which are attached to the upper assembly (see Figure 2.5). Through these guides, the upper assembly is comprised of an aluminum plate bolted to the upper rolling surface, constraining the latter to move vertically only via four flange-mounted bushings. To provide lateral stiffness, the rails are connected through structural angles and gusset plates to develop full moment connections. Ultimately, the setup is designed to provide smooth displacements both horizontally and vertically. Moreover, the tributary load that is being isolated is not transferred through the guides but through the steel rolling surfaces and ball to the rigid base. A detailed drawing of the rigid frame is presented in Figure 2.6, as it was originally fabricated at Fears Lab.

To prevent eccentricity rotations on the vertical guides generated when the ball rolls through the center of the rolling surface, the bearings connecting the upper assembly and the vertical guides were offset as shown in Figure 2.7. The left-most bearings where bolted underneath the aluminum plate holding the upper assembly, providing a 1/4-in. offset with this plate. The right-most bearings were bolted on top of said plate and a 1/4-in. aluminum spacer was placed in between the bearings and the plate. Together, a 3/4-in. eccentricity was generated.

Seven ($11 \times 11 \times 1$ in.) steel plates were used to act as proof mass. Four 1/4-20 threaded rods were put through these plates to keep them together, and the rods were bolted to the upper assembly. A crane was used to lift the proof mass and set it in place. The crane straps were never detached when performing tests to prevent potential failure of the experimental setup although these were loosened so that no load was held by them

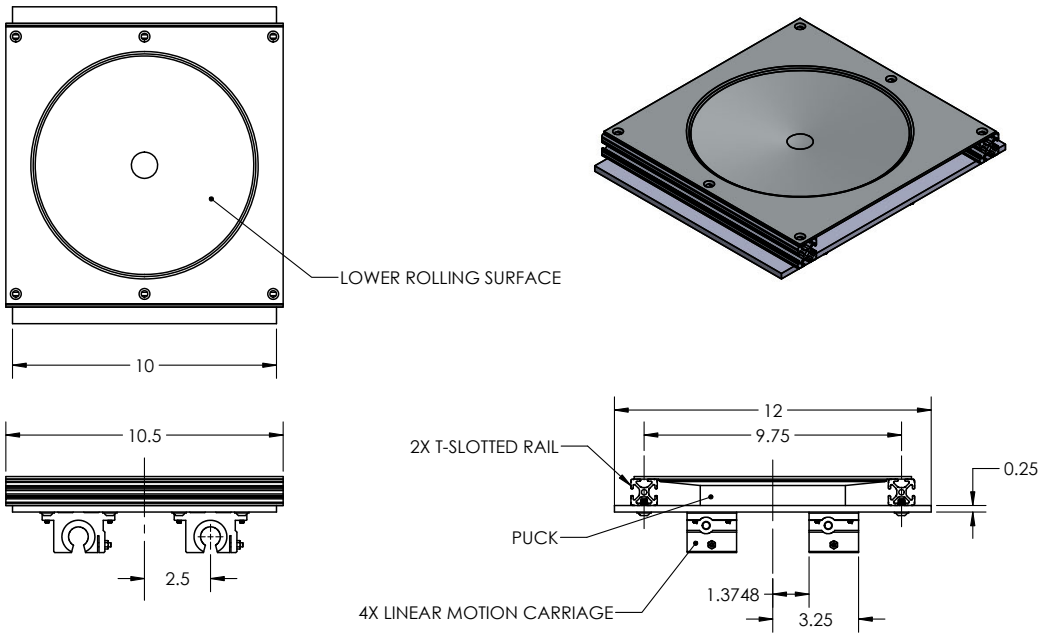

Figure 2.4: Drawing of the lower assembly of the experimental setup. (units: in.)

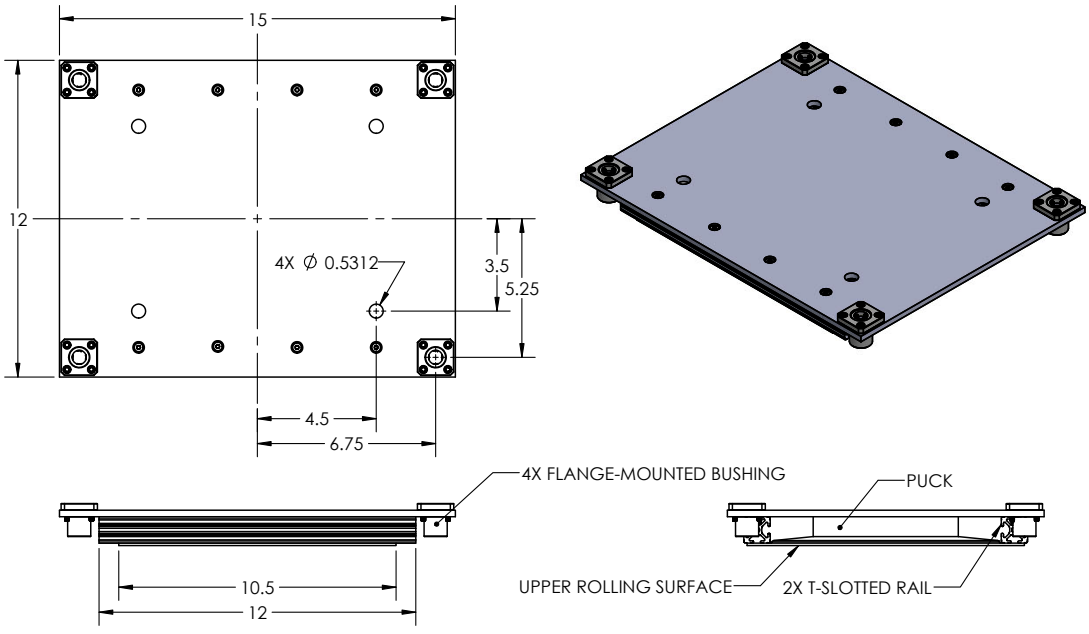

Figure 2.5: Drawing of the upper assembly of the experimental setup. (units: in.)

while testing. Rocking effects were noticed at the top steel plates after a couple of trial tests. To further diminish these effects on the proof masses, the steel plates were placed between two aluminum plates and tied together through threaded rods. The plates acted as wearing surfaces that were supported laterally by four ball transfers attached to the main rigid frame as shown in Figure 2.8.

The setup underwent some modification at the NHERI Lehigh EF to connect the specimen with the testing equipment as shown in Figure 2.9. To connect the experimental setup to the servo hydraulic actuator, a driving steel rod was attached underneath the aluminum plate supporting the lower rolling surface. Two small steel plates were welded to the rod at the front and back edges of the aluminum plate to act as shear keys. This rod was welded to a 1”-14 bolt which was attached to an S-shaped load cell. To avoid external forces from vertical and horizontal misalignment between the horizontal guides of the system and the actuator, a self-aligning ball connection was used in between the load cell and the mating clevis. Moreover, a linear bearing was used

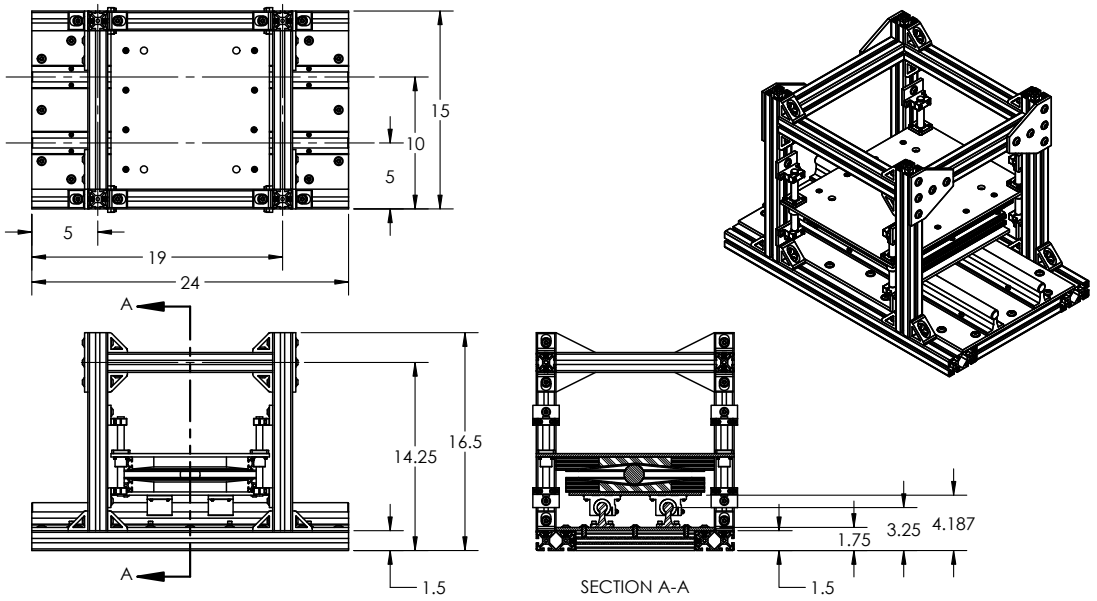

Figure 2.6: Drawing of the rigid frame portion of the experimental setup that was fabricated at Fears Lab. (units: in.)

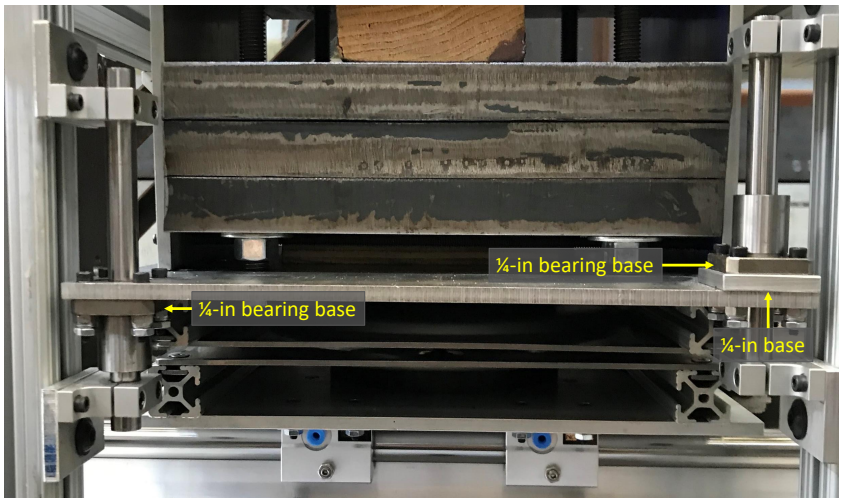

Figure 2.7: Vertical guides connection with upper assembly

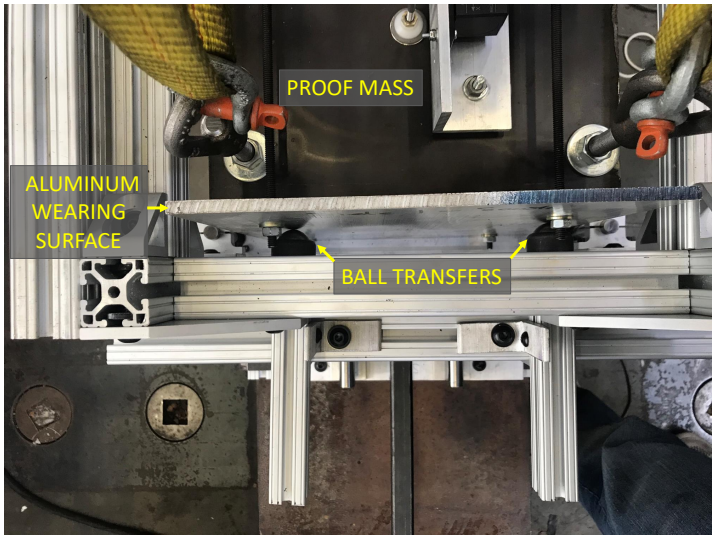

Figure 2.8: Proof mass setup with rotation-preventing aluminum plates

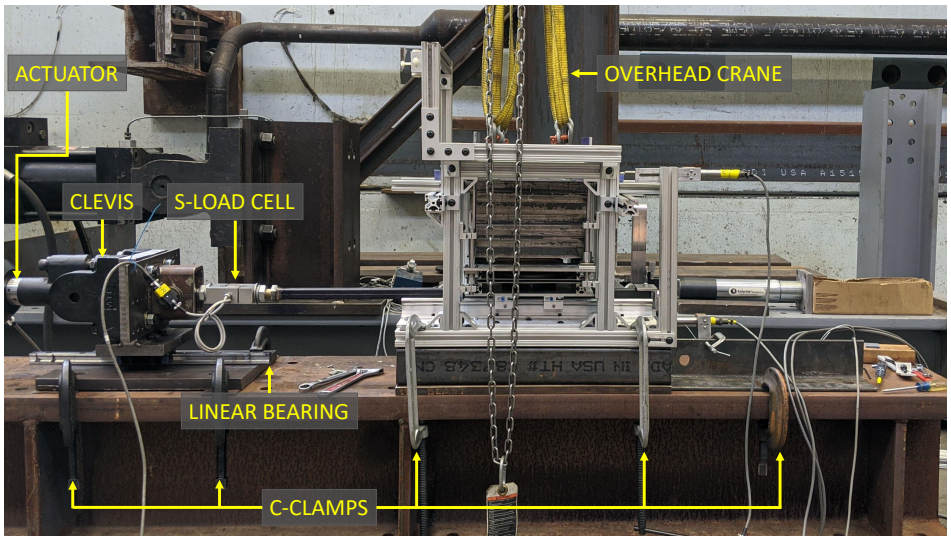

Figure 2.9: Final setup of RTHS testbed at the NHERI Lehigh EF

underneath the clevis-ball connection to prevent the load of the whole connection going into the setup. As well, both the frame experimental setup and the actuator-load cell connection were shimmed up so that the driving rod was completely horizontal and at the same level as the aforementioned connection configuration. Once this was achieved, five C-clamps were used on each side to attach the experimental setup to the base beam. Besides this additional hardware, more aluminum rails were added to support the data acquisition instrumentation.

2.4 Instrumentation

Figure 2.10 shows the sensor layout used to measure accelerations, forces, and displacements. To measure four desired accelerations, a unixial accelerometer (1a) was attached at the back end of the driving rod and a triaxial accelerometer (1b, 1c ,1d) was attached on top of the proof mass. To measure four desired displacements, four linear variable differential transformers (LVDTs) were attached on the setup—including one integrated within the actuator (2a). Of the other three LVDTs, one was attached on top of the proof mass to measure the upper assembly's vertical displacement (2c). Another was attached to the base of the frame to record slipping of the system (2b), and the last one was at-

tached to the top of the frame to measure whether there were lateral deflections or not (2d). An S-shaped LC101-10K load cell (3) was used to measure and record loads. The final sensor arrangement as used is shown in Figure 2.11.

2.5 RP Bearing Test Specimen

The experimental setup allows for replacing rolling surfaces. To perform both the characterization and RTHS tests, the rolling surfaces' rolling resistance was enhanced through the addition of elastomeric coating (QuakeCoat, WorkSafe Technologies, Valencia, CA). Moreover, both conical and flat surfaces were used to investigate the rolling resistance induced by the coating, which is added layer by layer to bare steel rolling surfaces. Different levels of coatings were used to understand the effect of such in the damping of the isolator unit. The specimens that were tested are described in Table 2.1 and a picture illustrating the different thicknesses is shown in Figure 2.12.

Besides the rolling resistance, the consequences of reducing the proof mass were also considered. The full tributary load was taken to be 240 lb and was applied by stacking up seven 11 by 11 by 1 in. steel plates. Another set of specimens was tested

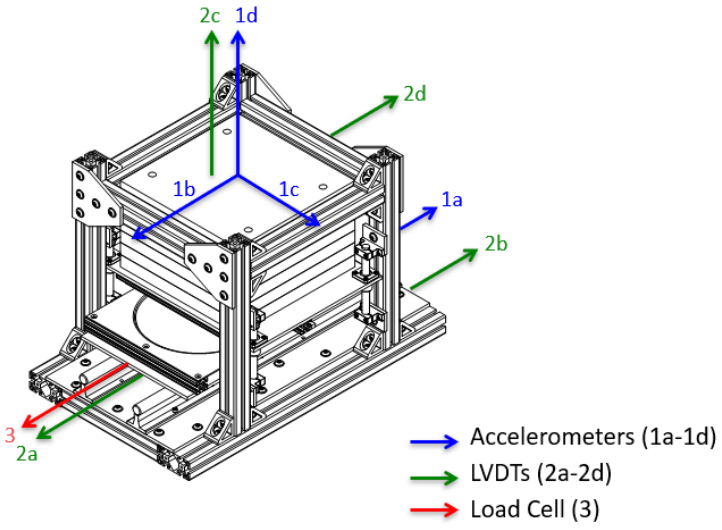

Figure 2.10: Sensor placement and characteristics on experimental setup

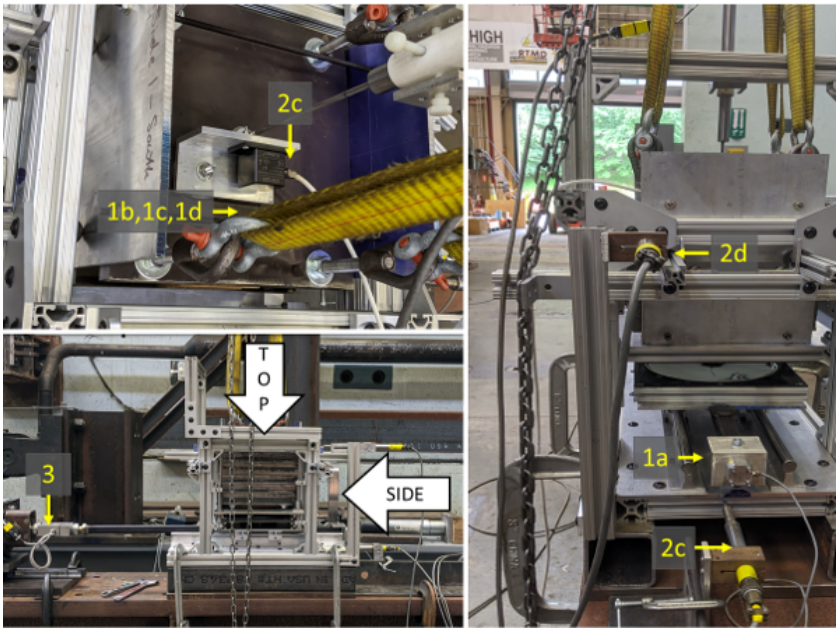

Figure 2.11: Final sensor arrangement on experimental setup at the NHERI Lehigh EF

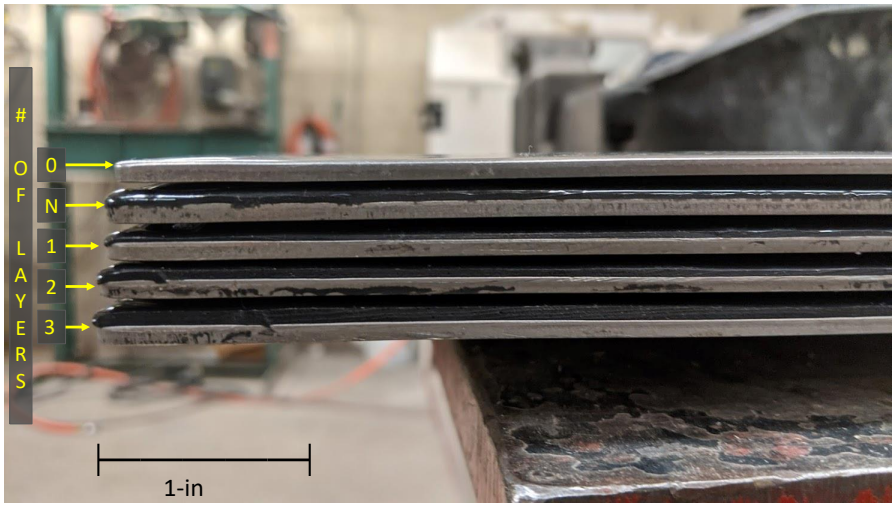

Figure 2.12: Rolling surfaces with different elastomeric rubber thickness

with only four steel plates on top, giving a reduced proof mass of approximately 143 lb. The specimens tested by each of these configurations is given in Table 2.1. All in all, the setup was arranged to fifteen unique configurations.

2.6 Summary

A setup was designed and fabricated to replicate a RP isolator unit under uniaxial lateral loading. The experimental setup was subjected to characterization and RTHS tests at the NHERI Lehigh EF. The specimen was arranged to fifteen unique configurations depending on the proof mass used and the shape and level of damping of the rolling surfaces. The properties of the various configurations are characterized in Chapter 3 and RTHS test to evaluate FIS-equipment and building-FIS interactions in Chapters 4 and 5, respectively.

Table 2.1: Test specimen characteristics

No.	Specimen	Rolling Surface		Payload weight (lbs)	Thickness‡ (in.)
		Profile	QuakeCoat treatment		
1	C0-240	Conical	None*	240	0 (n/a)
2	CN-240	Conical	Nominal†	240	0.067
3	C1-240	Conical	1 layer	240	0.045 (std)
4	C2-240	Conical	2 layers	240	0.065
5	C3-240	Conical	3 layers	240	0.096
6	C0-143	Conical	None	143	0
7	C1-143	Conical	1 layer	143	0.045
8	C2-143	Conical	2 layers	143	0.065
9	C3-143	Conical	3 layers	143	0.096
10	CN-143	Conical	Nominal	143	0.067
11	F0-143	Flat	None	143	0
12	F1-143	Flat	1 layer	143	0.045
13	F2-143	Flat	2 layers	143	0.065
14	F3-143	Flat	3 layers	143	0.096
15	F4-143	Flat	4 layers	143	0.112

*Bare steel, †Nominal thickness used by WorkSafe Technologies,

‡Mean (standard deviation) of $n = 4$ measurements.

Chapter 3
Characterization of a Rolling Pendulum Isolation Bearing with Enhanced Rolling Resistance

3.1 Overview

Three type of characterization tests were conducted. Two predefined motions—one quasi-static and one harmonic with varying displacements—were applied to the system for describing its properties (i.e., rolling resistance, load-deflection and load-velocity relationships, and effects of varying damping and tributary mass) and calibrating a physics-based analytical model. A third predefined synthetic motion was used to validate said model.

3.2 Test Protocol

Each specimen underwent harmonics of different frequency to calibrate a model of the RP isolator unit. First, a quasi-static test was performed. The input motion for this is shown in Figure 3.1. It was modeled as a sinusoidal wave with a maximum displacement of 6 in. at a frequency of 0.05 Hz. The wave is comprised of one cycle of ramping up followed by four complete cycles at the maximum displacement and one last cycle of ramping down.

Additionally, a sinusoidal wave was designed as per IEEE Standard 693 (2016). Figure 3.2 shows the displacement-time history at a frequency of 0.5 Hz. The motion

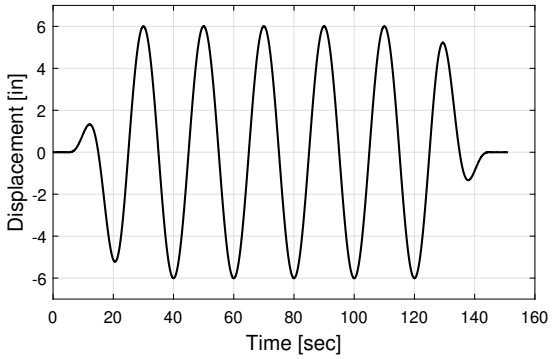

Figure 3.1: Quasi-static characterization wave

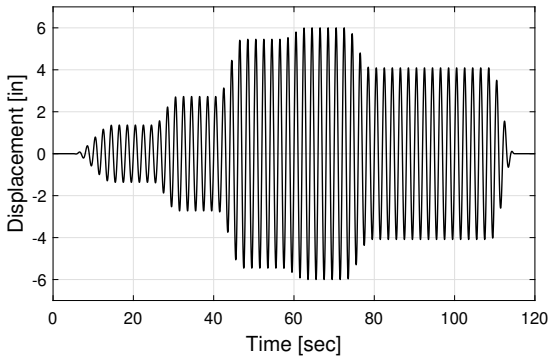

Figure 3.2: Characterization wave at 0.5 Hz

is staged at five different peak displacements: 25, 50, 100, 110, and 75% of a defined maximum displacement (5.45 in.). At last, the wave shows an overall maximum displacement (6 in.). To smooth changes in velocity at the amplitude transitions and meet the actuator's velocity and acceleration capacities, a pad of five seconds was implemented at the beginning. Similarly, there are three full transition cycles in-between each target peak displacement. The same target displacements were used with a wave frequency of 1 Hz.

To test the RP isolator unit and validate its model when calibrated, a synthetic motion (VERTEQ-II) defined in Telcordia (2012) was implemented. Figure 3.3 shows the VERTEQ-II time-history scaled to have a maximum displacement of 6 in., which was the input displacement for the last part of the system's characterization.

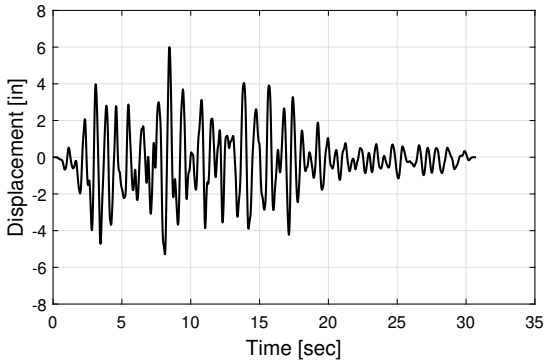

Figure 3.3: VERTEQ-II wave at 6-in. maximum displacement

3.3 Experimental Results

3.3.1 Data Processing

The data gathered was processed and analyzed in various ways. First, the load-deflection and load-velocity relationships of the isolator unit were studied. The former, as per the unaltered (raw) data obtained when testing the conical rolling surface with the nominal coating with 240 lb (CN-240) is shown under the harmonic wave at 0.5 Hz in Figure 3.4.

The load and displacement data was first detrended through a Fourier-transform based digital signal processing (FTDSP) (Gavin, 2013). The FTDSP was also used to differentiate the raw displacements once in order to obtain a FTDSP-detrended velocities. For all three detrended data sets, a high bandpass frequency of 512 Hz—half the 1024-Hz sample rate—was used. The FTDSP-detrended load-deflection and load-velocity relationships for the CN-240 specimen subject to the 0.5-Hz wave are shown in Figure 3.5(a).

Then, a moving average filter with a window length factor of 20 data points was implemented to further process the data sets of interest. In this step of the data processing, the inertial effects induced by the mass of and under the lower assembly were also corrected for. The mass of the lower assembly and the driving rod were measured to be

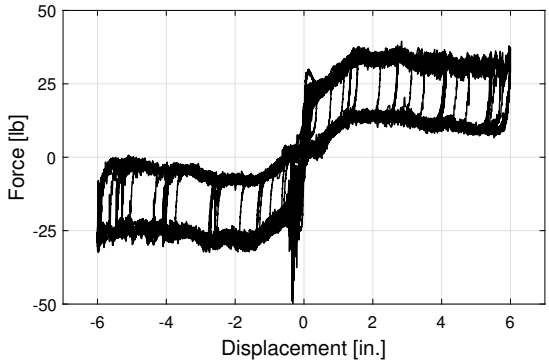

Figure 3.4: Load-deflection relationship of specimen CN-240 subject to 0.5-Hz characterization wave: raw data

18.2 lb/g. This total mass was multiplied by a factor of $-(2\pi f)^2$ where f is the harmonic wave's frequency and then multiplied by its displacement at a given time. This resulting inertial force was subtracted from the moving average filtered load to obtain the inertial-corrected load data. The moving average filtered and corrected load-deflection and load-velocity relationships for the CN-240 specimen subject to the 0.5-Hz wave are shown in Figure 3.5(b).

Lastly, the filtered and corrected data was down-sampled by a factor of 1/8 to finalize the signal processing. The resulting load-deflection and load-velocity plots for the CN-240 specimen subject to the 0.5-Hz wave are shown in Figure 3.5 (c).

3.3.2 Analysis and Results

To analyze the various displacements for a given frequency of the IEEE Standard 693 (2016) wave, one cycle of motion at each staged-displacement was selected. Figure 3.6 shows the cycles used in the designed 0.5-Hz wave with different colors, which were used throughout the analysis of the results. Similar cycles were selected when analyzing the results of the 1-Hz wave. The processed load-deflection and load-velocity diagrams for each of these cycle motions for specimen CN-240 subject to the 0.5-Hz wave are shown in Figure 3.7. All tested specimens were analyzed following the same procedure and their resulting load-deflection and load-velocity relationships are shown

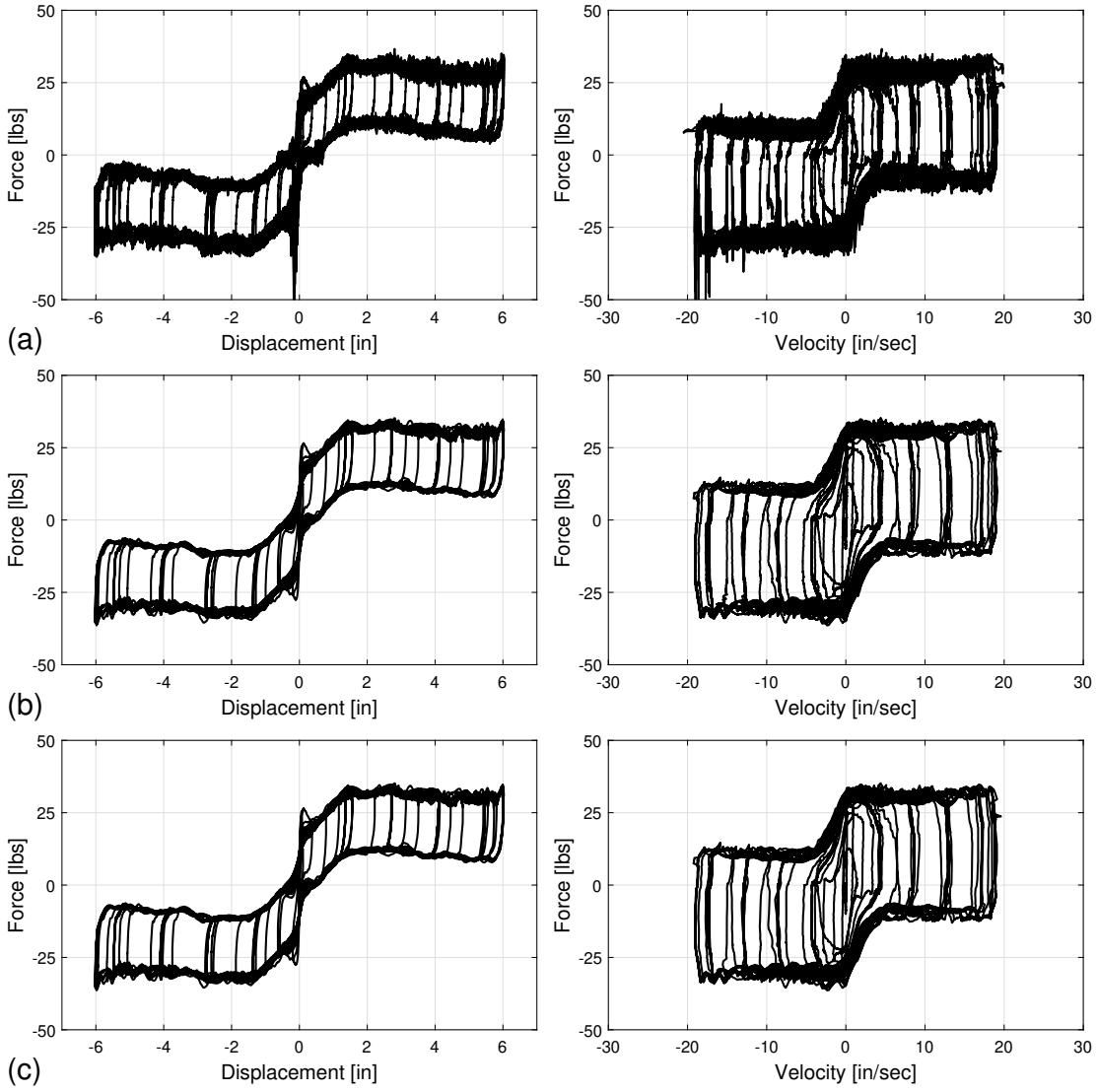

Figure 3.5: Load-deflection (left) and load-velocity (right) relationships of specimen CN-240 subject to 0.5-Hz characterization wave: (a) detrending, (b) moving average filtering and inertial correction, and (c) down-sampling.

in Appendix A.

When comparing the results for the rolling surfaces CN-240 and CN-143 obtained from testing them under the IEEE Standard 693 (2016) at 0.5 and 1 Hz, the effect of the tributary load can be evaluated from the load-deflection and load-velocity relationships. The resulting load-displacement and load-velocity relations for the CN-240 specimen in tested under a 1 Hz wave is shown in Figure 3.8. The load-displacements show a similar

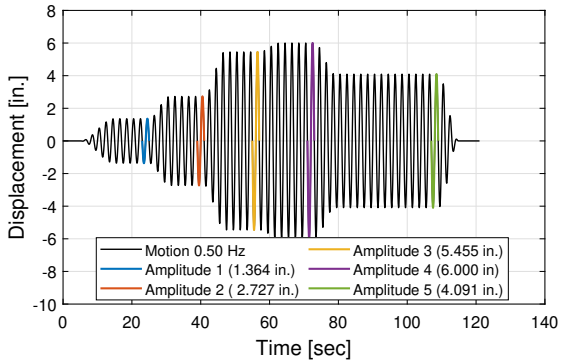

Figure 3.6: Amplitudes of interest in the 0.5-Hz wave

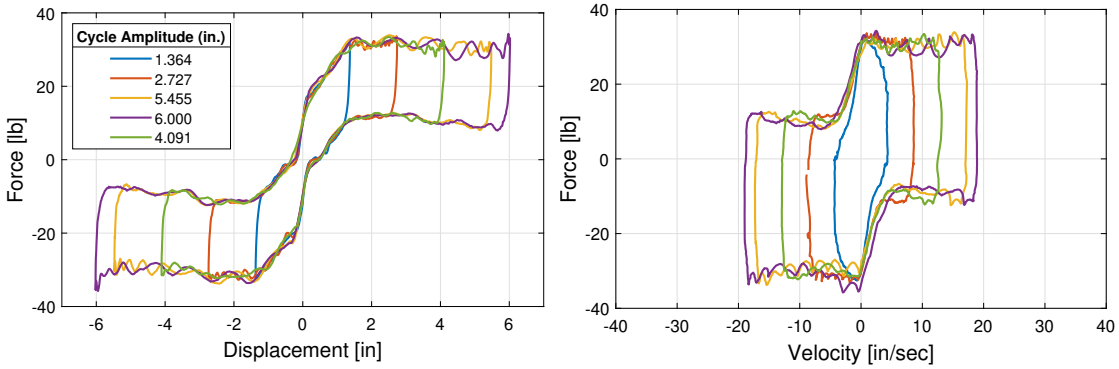

Figure 3.7: Load-deflection and load-velocity relationships with varying amplitudes of specimen CN-240 under 0.5-Hz wave

pattern in both Figures 3.7 and 3.8. These diagrams can be divided into three segments: a central with a parallelogram-like shape and two rectangle-like outer ones. The central one goes from approximately −1.5 in. to 1.5 in. and has a slope of approximately 40.7 lb/in., which represents the stiffness at the circular portion of the rolling surface. It transitions into two relatively horizontal segments at the aforementioned points for the rest of the displacement. These segments represent the the outer portions of the rolling surface profile, which have a constant slope. The behavior of all three segments shown in the load-deflection relationships is similar for all tested specimens (see Appendix A)—there is a corresponding constant force in the segments of constant slope.

For each amplitude, the associated maximum absolute force is similar at both tested frequencies. However, while at 0.5 Hz the lines line-up relatively well, when tested at 1

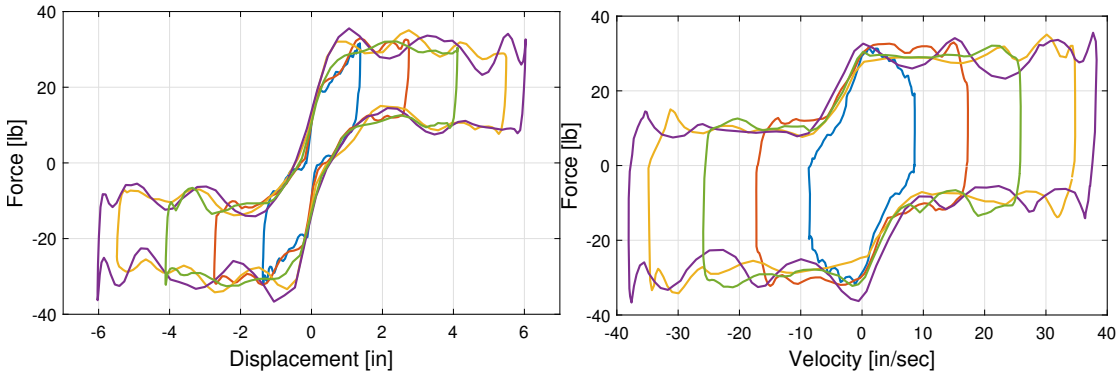

Figure 3.8: Load-deflection and load-velocity diagrams with varying amplitudes of specimen CN-240 under 1 Hz wave

Hz the specimen portrays a more inconsistent behavior. As the the amplitudes increase in the 1-Hz test, the central segment smoothens and the transitions to the ends become spikier. This can be attributed to higher inertial effects given by higher velocities and accelerations. The load-velocities relations are somewhat similar between the 0.5 and 1 Hz tests too. Since higher frequencies correspond to higher velocities, the load-velocity diagrams show that, at each set amplitude, the maximum velocity of the 0.5 Hz are half of those of the 1 Hz tests. The same holds true for the slope of the central segment. Regardless, the maximum forces are approximately equal for both tested frequencies.

Figure 3.9 shows the load-deflection and load-velocity relationships for the same rolling surface and frequency as Figure 3.7 but with a smaller tributary mass (i.e., 143 lbs.). It can be noticed that larger forces were developed for the tests specimen with larger tributary mass. The forces displayed in these figures include the gravitational restoring force of the system, which is proportional to the weight of the supported mass. Thus, the increase in force in when larger masses are tested. As well, at a given cycle amplitude, the difference between the minimum and maximum forces associated with such amplitude is different. Similarly, the load-velocity relations found for both 143 and 240 lbs. tests only vary with regards to the total force developed at a certain velocity.

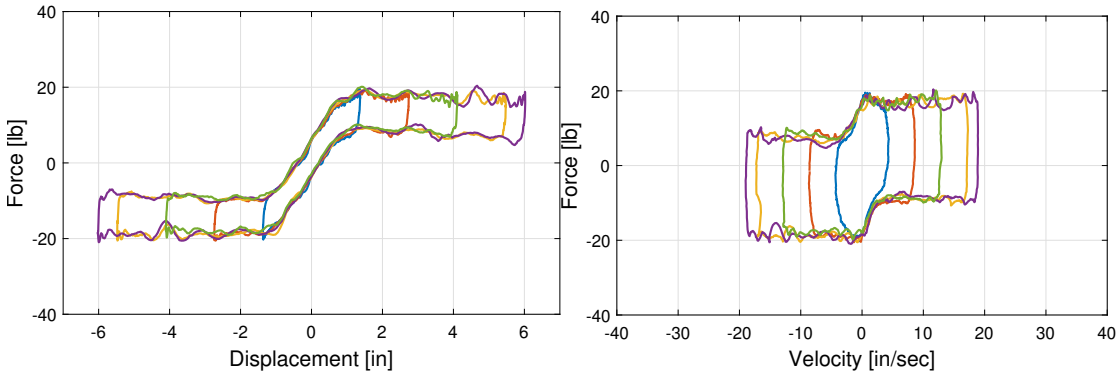

Figure 3.9: Load-deflection and load-velocity diagrams with varying amplitudes of specimen CN-143 under 0.5-Hz wave

3.3.3 Rolling Resistance Estimates

From the load-deflection relationship, it was possible to approximate the rolling resistance of each rolling surface at a given tested amplitude and frequency. To do so, a trapezoidal numerical integration scheme was implemented in order to calculate the area within a specific loop representing a cycle of motion. From this, 5 different rolling resistances were found per rolling surface tested—one per peak displacement. When dividing such rolling resistance by the tributary mass under which each test subjected, a normalized rolling resistance factor, μ, can be calculated. This factor resembles the Coulomb friction factor of sliding bearing systems. Figure 3.10 shows the rolling resistances factors of the conical surfaces as tested at different frequencies and under different tributary loads. The rolling resistance factors increase as the number of layers increase. Let it be noted that in all cases, the nominal coating, which rubber thickness is approximately the same as that of the 2 layers sample, is associated with the highest μ values. These rolling surfaces were produced around 5 years before the rest. Thus, the higher rolling resistance in this specimens could be attributed to an material aging affect, a change in chemical composition of the rubber used by the manufacturer, or both.

Looking at the variation of μ for a given plate, it can be noted that similar rolling

resistances are shown for all cases shown in Figure 3.10 when analyzing the bare steel surfaces. Furthermore, enhancing the damping of a rolling surface with one layer of elastomeric rubber increases this factor by approximately 600% and 900% for the 143 and 240 lbs. tributary masses, respectively. However, the effect of the number of layers thereon is almost negligible, especially between 2 and 3 layers and for all of the smaller mass tests. It can be concluded then, than the enhanced damping is effective as long as there is any elastomeric rubber in the rolling surfaces, but additional layering provides little additional benefit.

To more accurately characterize the rolling resistance factors, the IEEE Standard 693 (2016) harmonics wave was used to test flat plates with varying elastomeric rubber thicknesses (Bare Steel, 1, 2, 3, and 4 coating layers). This was, however, only performed for the 143 lbs. loads due to time constraints. The same procedure followed when calculating μ values for the conical rolling surfaces was implemented for these flat plates. Figure 3.11 shows the normalized rolling resistance factors of the varying levels of elastomeric coating for flat rolling surfaces supporting 143 lbs. under the 0.5 and 1 Hz harmonic waves. These results support the previously discussed findings. The enhanced damping samples shows a lot more rolling resistance than the bare steel rolling surfaces but after 1 layer of coating is added, the variation of rolling resistance is very small.

3.4 Model Calibration

A preliminary Bouc-Wen model was developed in MATLAB/Simulnk using the theoretical profile of the conical rolling surfaces. The model is dependant on the profile, slope, and curvature of the rolling surface. Figure 3.12 shows a surface profile comparison between the theoretical and experimental shapes, as well as an 14th-degree polynomial fitted to the experimental data. The theoretical shape is continues on profile and slope but discontinuous in curvature. As well, it is assumed to have only curvature in its cen-

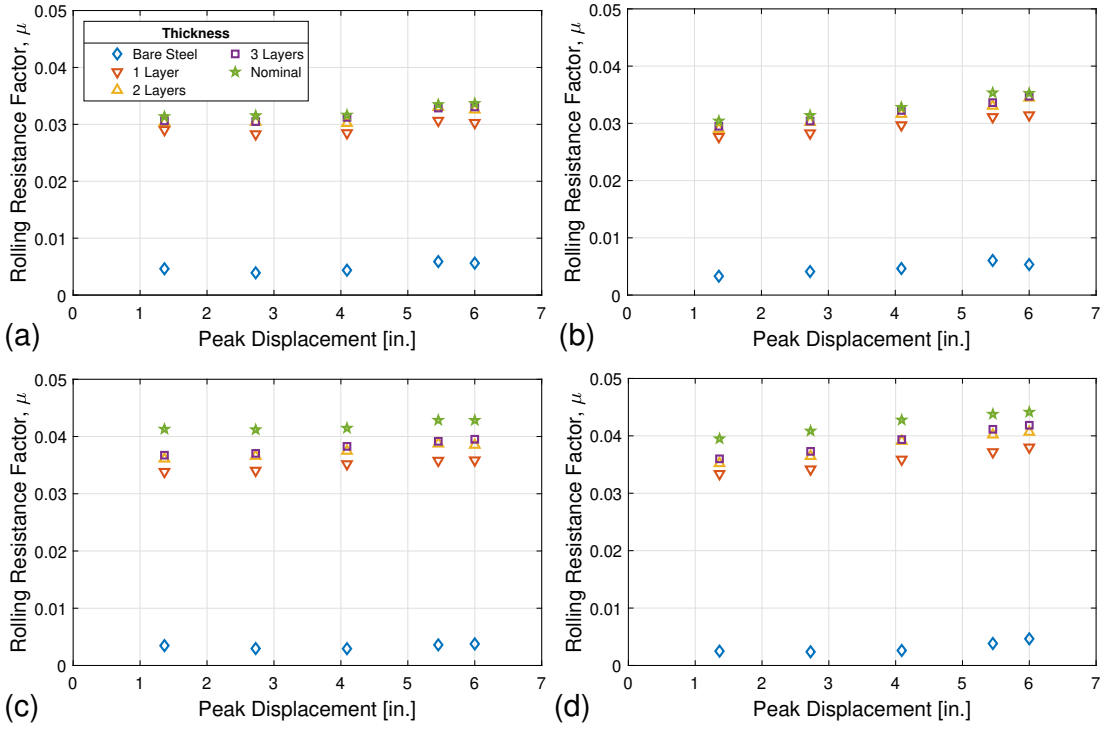

Figure 3.10: Rolling resistance factor at different peak displacements for conical rolling surfaces with different surface thicknesses: (a) 0.50 and (b) 1 Hz under 143 lbs, and (c) 0.50 and (d) 1 Hz under 240 lbs.

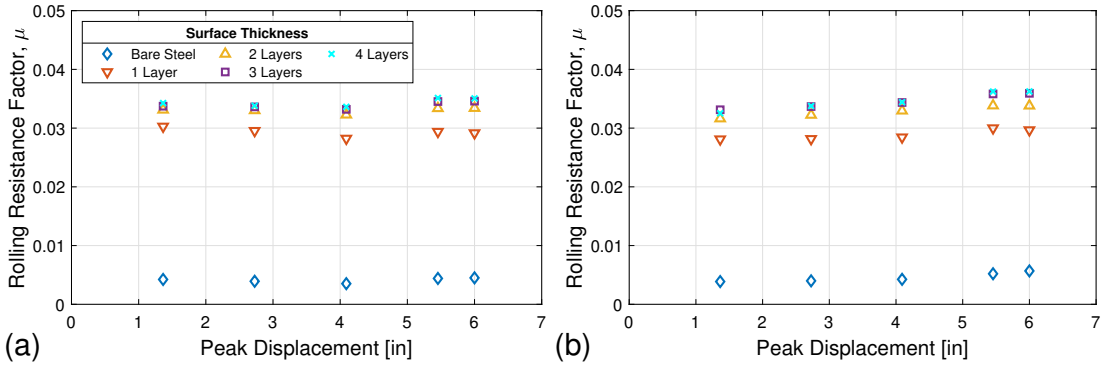

Figure 3.11: Rolling resistance factor at different peak displacements for flat rolling surfaces with different surface treatment thicknesses: (a) 0.50 and (b) 1 Hz under 143 lbs.

ter portion (i.e., the outer ends have a constant slope). However, from Figure 3.12 it is possible to notice that the shape of a Bare Steel rolling surface drawn from test data is different in that sense. While the center portion is very similar among the theoretical and experimental shapes, the outer portions of the plate have a slight concave down

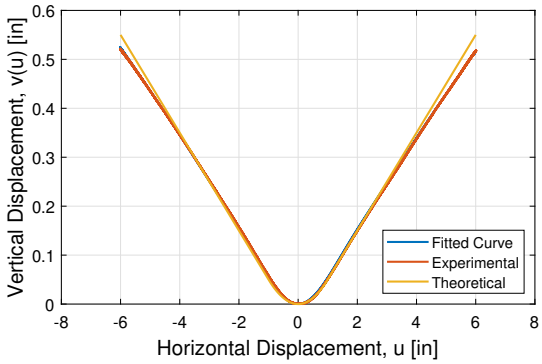

Figure 3.12: Theoretical,experimental and fitted profiles of conical Bare Steel rolling surfaces

curvature that becomes more prominent as for larger diameters. Thus, a more accurate profile of the rolling surface than the theoretically developed must be used in order to calibrate the model.

Figure 3.13 shows the fitted profile from Figure 3.12—which was attempted to substitute the theoretical profile in the preliminary Bouc-Wen model—as well as its slope and curvature. While for the fitted profile the slope and curvature are now continuous, the concavity in the outer portions of the surfaces produces non-conventional curvatures (see Figure 3.13 between for $|x| > 2$ in.). The 14th-degree polynomial was the poly function that closest resembled the shape of the rolling surfaces developed by experimental data. Thus, a different approach is to be taken to calibrate the model. Nevertheless, the load-deflection and load-velocity diagrams intended to serve as the model's validation are presented in Figures A.7 and A.8 (Appendix A).

3.5 Summary

The behavior of the experimental setup described in Chapter 2 was characterized under uni-axial loading by subjecting it to three different input motions. Through analyzing a load-deflection and load-velocity diagrams, the effect of the test specimen's rolling surface thickness and tributary mass. For the former, a rolling resistance factor was characterized for each of the rolling surfaces at different amplitudes, frequencies, and

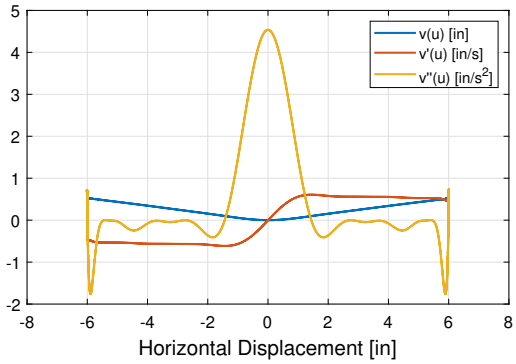

Figure 3.13: Profile, slope and curvature of fitted Bare Steel rolling surfaces

under different tributary mass. It was found that the elastomeric rubber for the enhanced damping rolling surfaces present develop a higher rolling resistance than the bare steel specimens, but relatively similar among other damped specimens. As well, a higher rolling resistance was for higher amplitudes. For the later, the samples with lower tributary mass were found to develop lower rolling resistance as well as lower gravitational restoring forces. The profile of a Bare Steel rolling surface was drawn from experimental data to calibrate a model of the experimental setup. However, the slopes and curvatures made the approach taken to model said shape into a function nonviable. The initial stiffness was found through these tests and was used for the proper implementation of RTHS tests, as described in Chapters 4 and 5.

Chapter 4
Real-Time Hybrid Simulation of a Rolling Pendulum Isolation System with Isolator–Equipment Interactions

4.1 Overview

The interactions between the floor isolation system (FIS) and the isolated equipment were evaluated. A general equation of motion for the system was developed to implement and perform real-time hybrid simulation (RTHS) tests. Said equation was adapted to successfully fit the characteristics of the experimental setup. The experimental setup was incorporated into two different finite element method (FEM) models—one representing the bearing with rigid equipment and another one with flexible equipment. The equation of motion was modified to accurately model a rolling pendulum (RP) isolator unit, and effectively integrate it into each model. Three input excitations were used to asses the FIS-equipment interactions in a total of 116 hybrid tests. The effects of isolating flexible equipment and rigid equipment in an RP unit isolator are studied.

4.2 Problem Formulation

RTHS tests were performed to evaluate the isolator-equipment interactions of the system described in Chapter 2. To successfully implement the MKR-alpha algorithm (Kolay and Ricles, 2019) into RTHS tests, a mathematical model of an RTHS experimental setup was developed. Figure 4.1 shows a schematic of an idealized RP bearing and

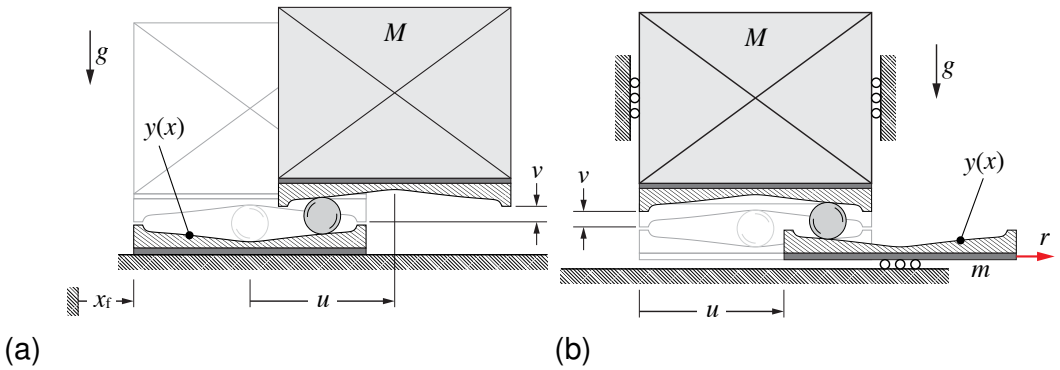

Figure 4.1: Idealized schematic of a) a single RP bearing and b) the experimental setup for dynamic analysis.

the designed experimental setup used. In both schematics, a structural floor motion x_f induces a horizontal (relative) displacement u in the system. The vertical displacement v of the proof mass M is kinematically constrained by the rolling of the ball across two concave surfaces having identical profiles $y(x)$. However, in the experimental setup for dynamic analysis the lower platform of of the bearing is not attached to the structural floor. Thus, its mass m is present whereas in a real RP bearing it is not.

For the experimental setup (Figure 4.1(b)), the kinetic energy $\mathcal{T}$ is given by:

$$\mathcal{T}(\dot{u}, \dot{v}) = \frac{1}{2} m\dot{u}^2 + \frac{1}{2} M\dot{v}^2 \tag{4.1}$$

and the potential energy $\mathcal{V}$ is given by

$$\mathcal{V}(v) = Mgv \tag{4.2}$$

where g is the acceleration due to gravity.

Assuming rolling without slipping, the ball will displace half of the horizontal displacement u of the lower platform. Hence, the kinematic constraint is written as follows:

$$v = 2y(u/2) \tag{4.3}$$

This expression can be differentiated to find the vertical velocity $\dot{v}$ of the proof mass:

$$\dot{v} = y'(u/2)\dot{u} \tag{4.4}$$

This expression can be differentiated to find the vertical acceleration $\ddot{v}$ of the proof mass:

$$\ddot{v} = y''(u/2)\dot{u}^2/2 + y'(u/2)\ddot{u} \tag{4.5}$$

From these constraints, the kinetic and potential energies can be re-expressed in terms of only u (and $\dot{u}$) as follows:

$$\mathcal{T}(u, \dot{u}) = \frac{1}{2}m\dot{u}^2 + \frac{1}{2}M[y'(u/2)\dot{u}]^2 \tag{4.6}$$

and

$$\mathcal{V}(u) = 2Mgy(u/2) \tag{4.7}$$

The equation of motion, in terms of u alone, are found using Lagrange's equation:

$$\frac{d}{dt}\frac{\partial \mathcal{L}}{\partial \dot{u}} - \frac{\partial \mathcal{L}}{\partial u} = Q_u \tag{4.8}$$

where the Lagrangian $\mathcal{L} = \mathcal{T} - \mathcal{V}$ and Q_u is the generalized force associated with u. The resulting equation of motion is given by

$$m\ddot{u} + M\ddot{u}[y'(u/2)]^2 + M\dot{u}^2y'(u/2)y''(u/2)/2 + Mgy'(u/2) + f_d = r^e(t) \tag{4.9}$$

where r^e is the force applied experimentally to the lower platform in the direction of u, and f_d is the dissipative force due to rolling resistance.

The RTHS experimental setup (Figure 4.1b)) is meant to emulate an RP bearing for use in an isolation system. For this, an important distinction was made between a real RP-bearing and the experimental setup. In a RP isolator unit, the system is attached to the structural floor level while for the RTHS experimental setup it is not. In other words, the mass of the lower platform, m, is not real in an RP isolator unit. Consequently, extra

inertial force arise that needs to be corrected for. Following a similar procedure that in Section 4.2, after applying Lagrange's equation (4.8), the equation of motion for an isolation system utilizing RP bearings is given by (Harvey, 2015)

$$M\ddot{u} + M\ddot{u}[y'(u/2)]^2 + M\dot{u}^2 y'(u/2)y''(u/2)/2 + Mgy'(u/2) + f_d = -M\ddot{x}_{\mathrm{f}}(t) \tag{4.10}$$

Equation (4.10) is almost identical to that of the RTHS setup [Equation (4.9)], with exception of the first (inertial) term—$M\ddot{u}$ for the isolation system, and $m\ddot{u}$ for the RTHS setup—and the right hand sides of the equations. These differences are important in the testing of an RP bearing using the RTHS setup (Fig. 2.1) as discussed in the following section. Since the mass is real in the experimental setup, this correction can be done numerically through RTHS in the tests' numerical sub-system.

4.3 Implementation of Real-Time Hybrid Testing

In the context of RTHS tests, the force $r^e(t)$ appearing in Equation (4.9) is the *experimental restoring force* that would be measured by the load cell when the prescribed displacement $u(t)$ and velocity $\dot{u}(t)$ (and indirectly acceleration $\ddot{u}(t)$) are imposed on the RP bearing. This experimental restoring force would then be fed back into the numerical model to simulate an isolation system's dynamics (see Section 1.2.2). Substituting the experimental restoring force defined by Equation (4.9) into Equation (4.10), the equation of motion to be integrated in a real-time hybrid test is given by

$$M\ddot{u}(t) + r(t) = F(t) \tag{4.11}$$

where

$$F(t) \equiv \begin{cases} 0, & \text{Free vibration} \\ -M\ddot{x}_{\mathrm{f}}(t), & \text{Floor motion} \end{cases} \tag{4.12}$$

is the *external excitation* (force), and

$$r(t) = r^e(t) - m\ddot{u}(t) \tag{4.13}$$

$$\equiv M\ddot{u}[y'(u/2)]^2 + M\dot{u}^2 y'(u/2)y''(u/2)/2 + Mgy'(u/2) + f_d \tag{4.14}$$

is the *compensated* restoring force, i.e., the experimentally measured restoring force $r^e(t)$ having removed the inertial effect due to the the lower stage (m), which is not present in an isolation system. Substituting the compensated restoring force (4.13) into Equation (4.11) gives

$$(M - m)\ddot{u}(t) + r^e(t) = F(t) \tag{4.15}$$

This equation represents the differential equation that was integrated *numerically* as part of the RTHS testing. For some of the SDOF experiments, this compensation was neglected (i.e., $m = 0$), and for some others the compensation was performed on the right-hadn side of the equation, having Equation (4.15) presented as:

$$M\ddot{u}(t) + r^e(t) = F(t) \tag{4.16}$$

for the former, and:

$$M\ddot{u}(t) + r^e(t) = F(t) - m\ddot{x}_{\mathrm{f}}(t) \tag{4.17}$$

for the latter.

To evaluate the FIS-equipment interactions, the RP bearing and equipment were modeled as both a rigid single-degree-of-freedom (SDOF) and a flexible three-degree-of-freedom (3DOF) system. The following subsections describe in-depth such modelling.

4.3.1 Modelling of a Rolling Pendulum Isolator Unit to Protect Rigid Equipment

For protecting rigid equipment, the RP isolator unit was modelled as a SDOF system using HybridFEM, a 2D finite-element environment developed by researchers at Lehigh University. This was achieved by defining two nodes effectively overlapping. Node 1 represents the base of the RP bearing and node 2 depicts the base of the equipment being isolated. The former moves along with the ground motion (i.e., is fixed in the x, y, and θ directions) while the latter is free to tanslate horizontally. In the same way, node 1 is defined to have the whole tributary mass M. In this node, too, the mass correction described in by Equation (4.15) takes place—m is subtracted from M on the left-hand side of the equation. Note that m is a measured physical value and, since the configuration of the lower platform is the same for all the experiments performed, m does not change. This holds true for both model configurations (i.e., SDOF and 3DOF). The nodes aforementioned were connected through an experimental element, which represents the experimental RP isolator unit. This was given a initial stiffness and damping obtained from the characterization test described in Chapter 3.

The integration of the MKR-α algorithm in real time was performed at a sample rate of 1024 Hz with 6-step interpolation. As well, to control the numerical dissipation, the parameter ρ in the algortihm was set to 0.75 for all the experiments with the SDOF model. The algorithm's integration and the signal generation of the tests were performed using the Simulink model shown in Figure 4.2. This model also handled the communication between the experimental and numerical substructures for the SDOF experiments.

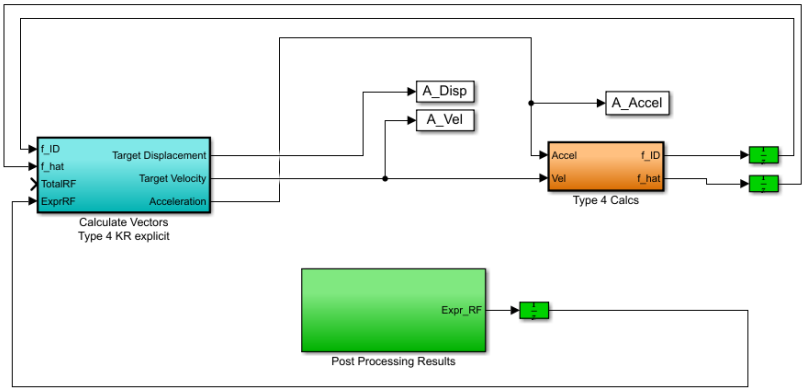

Figure 4.2: Simulink model containing the MKR-α algorithm used for SDOF tests

4.3.2 Modelling of a Rolling Pendulum Isolator Unit with Flexible Equipment

For protecting flexible equipment, the RP isolator unit was modelled as a 3DOF system using HybridFEM. The equipment is flexible as it is thought to have an internal frequency itself, independent from the frequency of the RIS. Thus, the frequency of the equipment being isolated at its base is defined as f, and it is parameterized as $f = 1, 2, 5,$ and 10 Hz. Note that 10 Hz is a lot grater than the natural frequency of the RP bearing, and can be understood as effectively rigid. The base of the RP isolator unit was defined in the same way that for the SDOF system through a fixed-fixed-fixed node (1). The equipment, however, was modeled as a 2-meter tall cantilever beam with lumped mass at node 3 . Thus, the node representing the base of the equipment (2), still effectively overlaps with node 1 and is allowed to translate horizontally. However, it only holds half the tributary mass M. The other half is placed in an extra node (3), which location is defined to be at a height (h) of 2 meters above nodes 1 and 2. Node 3 is restricted to displace vertically, thus it is free to move in the x and θ directions.

Nodes 1 and 2 are connected through an experimental element, similarly to the SDOF system. Nodes 2 and 3 are connected assuming the cantilever beam is an Euler-Bernoulli beam. For this, the cantilever's flexural and axial rigidity were calculated as a

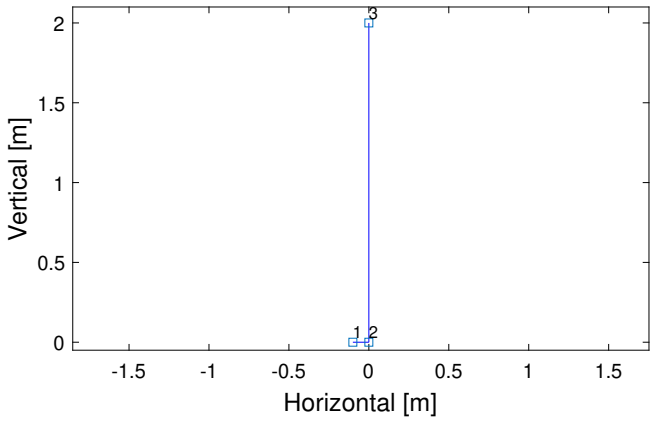

Figure 4.3: Model of RP isolator unit for protecting flexible equipment with its nodes' location

function of the M, h, and f. As well, since the mass is lumped at the ends of the beam, the mass per unit length is set to zero for this system. Figure 4.3 shows the system as modeled by HybridFEM.

The lower platform's mass correction in this system is performed after the model is created. Once HybridFEM created a mass matrix given nodes 2 and 3 each hold $M/2$, m is subtracted from the first term of said matrix. The damping configuration of the system is assigned to be stiffness-proportional assuming 2% damping in the first mode. For the majority of the experiments performed with this model, ρ is set to 0.5, although 0.75 is used for some of the initial test. The sample rate and number of interpolations are the same as those for the SDOF system. The algorithm's integration and the signal generation of the tests were performed using the Simulink model shown in Figure 4.4. This model also handled the communication between the experimental and numerical substructures for the 3DOF experiments.

4.4 Test Protocol

The experimental setup was subject to three different tests: a free vibrations tests, and two equipment sensitivity test protocols. These three tests are defined by the floor acceleration $\ddot{u}_f(t)$, which acts as the disturbance to the numerical model (see Equation

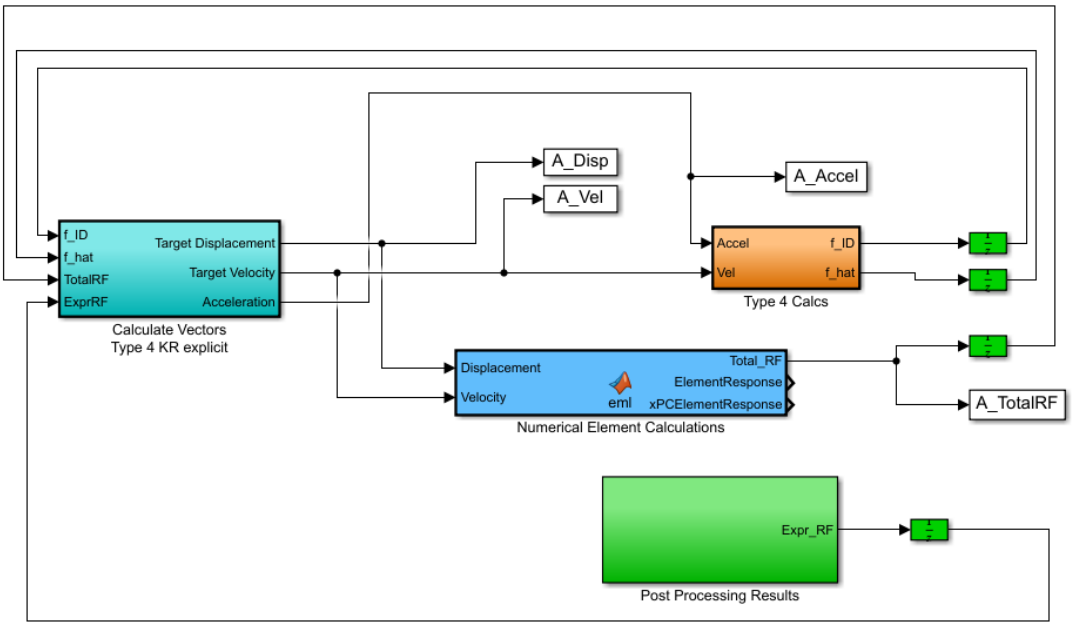

Figure 4.4: Simulink model containing the MKR-α algorithm used for 3DOF tests

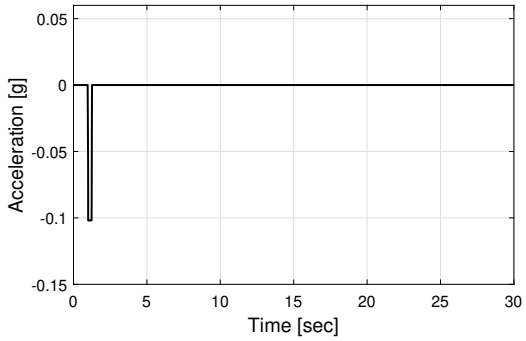

Figure 4.5: Acceleration-time history of the 0.25 seconds square-impulse wave

(4.12))). For the free vibrations tests, a unit acceleration impulse was applied as rectangular loading for 0.25 seconds. The total duration of this response is 30 seconds, as shown in Figure 4.5. The experimental setup was subject to free vibrations tests for both rigid and flexible equipment (i.e., using both SDOF and 3DOF models).

The experimental setup was also subject to a narrow-band, random, sweep records generated by a MATLAB routine (Wilcoski et al., 1997) as specified in ATC (2007). To pick an input signal that was the most meaningful to the testing of the RP isolator units,

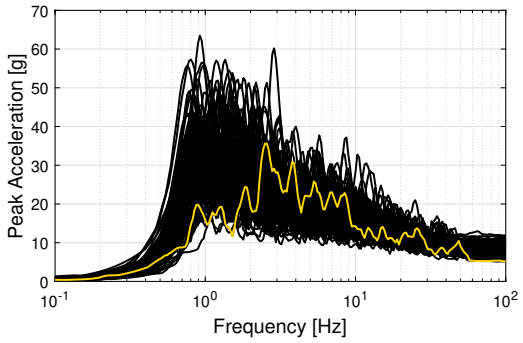

Figure 4.6: Spectra response of one hundred randomly generated narrow-band signals (chosen response shown in yellow)

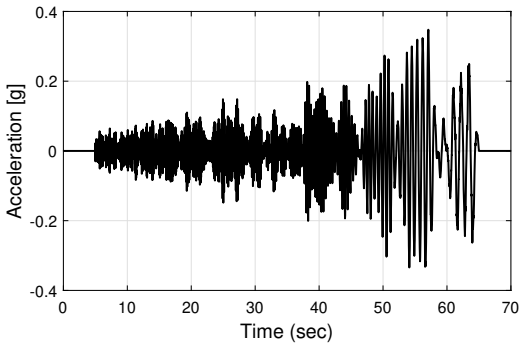

Figure 4.7: Acceleration-time history of the FEMA 461 standard randomly generated narrow-band signal

one hundred of these were generated. Then, a spectra response analysis was performed for all the generated signals. A signal was finally picked after a comparing said spectra by a linear least squares approximation and a target spectral acceleration suggested in ATC (2007). Figure 4.6 shows the spectra response analysis of all the randomly generated narrow-band signals and the one selected after the linear least squares approximation. Figure 4.7 shows the acceleration-time history to which the experimental setup was subject. This input excitation was only used for the rigid equipment system.

Lastly, the experimental setup was subject to the VERTEQ-II wave, a synthetic floor motion given by Telcordia (2012). The acceleration-time history of VERTEQ-II is shown in Figure 4.8. The experimental setup was subject to this excitation for both the rigid and flexible equipment configurations.

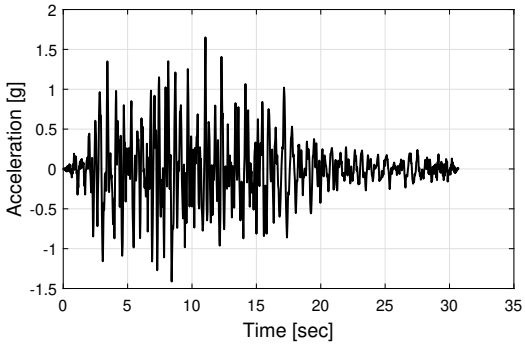

Figure 4.8: Acceleration-time history of the VERTEQ-II wave

4.4.1 Test Matrix

Figure 4.9 shows the test matrix developed for evaluating the FIS-equipment interactions. A total of 116 tests were performed, from which 21 studied the FIS behavior with flexible equipment (i.e., used the 3DOF model) and the rest did so for rigid (i.e., used the SDOF model). Ten different rolling surfaces with 5 levels of damping were used, as well as two tributary loads (240 and 143 lbs).

4.5 Experimental Results

Through RTHS, it was possible to obtain information about the kinetic behavior of the system due to the applied uniaxial loading. In specific, the displacements, velocities, and accelerations relative to the input excitements were recorded for the respective DOFs of each model. Then, through these experimental results, it is possible to asses the isolation performance of the RP bearing.

4.5.1 Free Vibrations

The model considering rigid equipment protection was implemented for two different rolling surfaces—Bare Steel (zero) and the QuakeCoat (nominal)—subject to free vibrations tests. In all of these tests the setup held a tributary load of 240 lbs. Figures 4.10 and 4.11 show the displacement and acceleration time-histories of the experimental setup when subject to different intensities of the impulse wave (see Figure 4.5) using

ROLLING SURFACE	TEST #	WEIGHT (lb)	INPUT MOTION	EQUIPMENT	INTENSITY	DATE
1. Bare Steel	1	240	Free Vibration	Rigid Equip.	1x Impulse	27/08/2020
	2	240	Free Vibration	Rigid Equip	2x Impulse	27/08/2020
	3	240	VERTEQ-II (GR-63)	Rigid Equip.	0.25 scale factor	27/08/2020
	4	240	VERTEQ-II (GR-63)	Rigid Equip.	0.33 scale factor	27/08/2020
	5	240	VERTEQ-II (GR-63)	Rigid Equip.	0.4 scale factor	27/08/2020
	6	240	VERTEQ-II (GR-63)	Rigid Equip.	0.5 scale factor	27/08/2020
	7	240	VERTEQ-II (GR-63)	Rigid Equip.	0.5 scale factor	27/08/2020
	8	240	VERTEQ-II (GR-63)	Rigid Equip.	0.5 scale factor	27/08/2020
	9	240	VERTEQ-II (GR-63)	Rigid Equip	0.6 scale factor	27/08/2020
	10	240	FEMA 461	Rigid Equip.	0.167 scale factor	28/08/2020
	11	240	FEMA 461	Rigid Equip.	0.25 scale factor	28/08/2020
	12	240	FEMA 461	Rigid Equip.	0.333 scale factor	28/08/2020
	13	240	FEMA 461	Rigid Equip.	0.4 scale factor	28/08/2020
	14	240	FEMA 461	Rigid Equip	0.5 scale factor	28/08/2020
	15	240	FEMA 461	Rigid Equip	0.625 scale factor	28/08/2020
	16	240	FEMA 461	Rigid Equip.	0.75 scale factor	08/28/2020
	17	240	Free Vibration	Flexible Equip. (10 Hz)	1x Impulse	28/08/2020
	18	240	Free Vibration	Flexible Equip. (5 Hz)	1x Impulse	28/08/2020
	19	240	Free Vibration	Flexible Equip. (2 Hz)	1x Impulse	28/08/2020
	20	240	Free Vibration	Flexible Equip. (1 Hz)	1x Impulse	28/08/2020
	21	240	Free Vibration	Flexible Equip. (10 Hz)	2x Impulse	28/08/2020
	22	240	Free Vibration	Flexible Equip. (5 Hz)	2x Impulse	28/08/2020
	23	240	Free Vibration	Flexible Equip. (2 Hz)	2x Impulse	28/08/2020
	24	240	Free Vibration	Flexible Equip. (1 Hz)	2x Impulse	08/28/2020
	25	240	VERTEQ-II (GR-63)	Flexible Equip. (10 Hz)	0.5 scale factor	28/08/2020
	26	240	VERTEQ-II (GR-63)	Flexible Equip. (10 Hz)	0.4 scale factor	28/08/2020
	27	240	VERTEQ-II (GR-63)	Flexible Equip. (5 Hz)	0.4 scale factor	28/08/2020
	28	240	VERTEQ-II (GR-63)	Flexible Equip. (2 Hz)	0.4 scale factor	28/08/2020
	29	240	VERTEQ-II (GR-63)	Flexible Equip. (1 Hz)	0.4 scale factor	08/28/2020
2. QuakeCoat (nominal)	1	240	Free Vibration	Rigid Equip.	1x Impulse	31/08/2020
	2	240	Free Vibration	Rigid Equip	1x Impulse	31/08/2020
	3	240	Free Vibration	Rigid Equip	1x Impulse	31/08/2020
	4	240	Free Vibration	Rigid Equip	10x Impulse	31/08/2020
	5	240	Free Vibration	Rigid Equip	5x Impulse	31/08/2020
	6	240	Free Vibration	Rigid Equip	2x Impulse	31/08/2020
	7	240	Free Vibration	Rigid Equip	3x Impulse	31/08/2020
	8	240	VERTEQ-II (GR-63)	Rigid Equip.	0.25 scale factor	31/08/2020
	9	240	VERTEQ-II (GR-63)	Rigid Equip.	0.5 scale factor	31/08/2020
	10	240	VERTEQ-II (GR-63)	Rigid Equip.	0.75 scale factor	31/08/2020
	11	240	VERTEQ-II (GR-63)	Rigid Equip.	1 scale factor	31/08/2020
	12	240	VERTEQ-II (GR-63)	Rigid Equip.	1 scale factor	04/09/2020
	13	240	FEMA 461	Rigid Equip.	0.33 scale factor	31/08/2020
	14	240	FEMA 461	Rigid Equip.	0.5 scale factor	31/08/2020
	15	240	FEMA 461	Rigid Equip.	0.625 scale factor	31/08/2020
	16	240	FEMA 461	Rigid Equip.	0.8 scale factor	31/08/2020
	17	240	FEMA 461	Rigid Equip	1 scale factor	31/08/2020
	18	240	VERTEQ-II (GR-63)	Flexible Equip. (10 Hz)	0.75 scale factor	31/08/2020
	19	240	VERTEQ-II (GR-63)	Flexible Equip. (5 Hz)	0.75 scale factor	31/08/2020
	20	240	VERTEQ-II (GR-63)	Flexible Equip. (5 Hz)	1 scale factor	31/08/2020
	21	240	VERTEQ-II (GR-63)	Flexible Equip. (5 Hz)	1 scale factor	31/08/2020
	22	240	VERTEQ-II (GR-63)	Flexible Equip. (2 Hz)	0.75 scale factor	31/08/2020
	23	240	VERTEQ-II (GR-63)	Flexible Equip. (2 Hz)	1 scale factor	31/08/2020
	24	240	VERTEQ-II (GR-63)	Flexible Equip. (1 Hz)	0.75 scale factor	31/08/2020
	25	240	VERTEQ-II (GR-63)	Flexible Equip. (1 Hz)	1 scale factor	31/08/2020
3. QuakeCoat – 1 Layer	1	240	VERTEQ-II (GR-63)	Rigid Equip.	0.25 scale factor	31/08/2020
	2	240	VERTEQ-II (GR-63)	Rigid Equip.	0.5 scale factor	31/08/2020
	3	240	VERTEQ-II (GR-63)	Rigid Equip.	0.75 scale factor	31/08/2020
	4	240	VERTEQ-II (GR-63)	Rigid Equip.	1 scale factor	31/08/2020
	5	240	FEMA 461	Rigid Equip.	0.4 scale factor	31/08/2020
	6	240	FEMA 461	Rigid Equip.	0.5 scale factor	31/08/2020
	7	240	FEMA 461	Rigid Equip.	0.625 scale factor	31/08/2020
	8	240	FEMA 461	Rigid Equip.	0.8 scale factor	31/08/2020
	9	240	FEMA 461	Rigid Equip	1 scale factor	31/08/2020

Figure 4.9: Real-time hybrid simulation test matrix for evaluating FIS-equipment interactions

5. QuakeCoat – 3 Layers	1	240	VERTEQ-II (GR-63)	Rigid Equip.	0.25 scale factor	31/08/2020
	2	240	VERTEQ-II (GR-63)	Rigid Equip.	0.5 scale factor	31/08/2020
	3	240	VERTEQ-II (GR-63)	Rigid Equip.	0.75 scale factor	31/08/2020
	4	240	VERTEQ-II (GR-63)	Rigid Equip.	1 scale factor	31/08/2020
	5	240	FEMA 461	Rigid Equip.	0.4 scale factor	31/08/2020
	6	240	FEMA 461	Rigid Equip.	0.5 scale factor	31/08/2020
	7	240	FEMA 461	Rigid Equip.	0.625 scale factor	31/08/2020
	8	240	FEMA 461	Rigid Equip.	0.8 scale factor	31/08/2020
	9	240	FEMA 461	Rigid Equip	1 scale factor	31/08/2020
	10	240	FEMA 461	Rigid Equip	1.25 scale factor	31/08/2020
4. QuakeCoat – 2 Layers	1	240	VERTEQ-II (GR-63)	Rigid Equip.	0.25 scale factor	31/08/2020
	2	240	VERTEQ-II (GR-63)	Rigid Equip.	0.5 scale factor	31/08/2020
	3	240	VERTEQ-II (GR-63)	Rigid Equip.	0.75 scale factor	31/08/2020
	4	240	VERTEQ-II (GR-63)	Rigid Equip.	1 scale factor	31/08/2020
	5	240	FEMA 461	Rigid Equip.	0.4 scale factor	31/08/2020
	6	240	FEMA 461	Rigid Equip.	0.5 scale factor	31/08/2020
	7	240	FEMA 461	Rigid Equip.	0.625 scale factor	31/08/2020
	8	240	FEMA 461	Rigid Equip.	0.8 scale factor	31/08/2020
	9	240	FEMA 461	Rigid Equip	1 scale factor	31/08/2020
8. QuakeCoat – 2 Layer	1	143	VERTEQ-II (GR-63)	Rigid Equip.	0.25 scale factor	02/09/2020
	2	143	VERTEQ-II (GR-63)	Rigid Equip.	0.5 scale factor	02/09/2020
	3	143	VERTEQ-II (GR-63)	Rigid Equip.	0.75 scale factor	02/09/2020
	4	143	VERTEQ-II (GR-63)	Rigid Equip.	1 scale factor	02/09/2020
	5	143	VERTEQ-II (GR-63)	Rigid Equip.	0.25 scale factor	02/09/2020
	6	143	VERTEQ-II (GR-63)	Rigid Equip.	0.5 scale factor	02/09/2020
	7	143	VERTEQ-II (GR-63)	Rigid Equip.	0.75 scale factor	02/09/2020
	8	143	VERTEQ-II (GR-63)	Rigid Equip.	1 scale factor	02/09/2020
	9	143	FEMA 461	Rigid Equip.	0.4 scale factor	02/09/2020
	10	143	FEMA 461	Rigid Equip.	0.5 scale factor	02/09/2020
	11	143	FEMA 461	Rigid Equip	0.625 scale factor	02/09/2020
	12	143	FEMA 461	Rigid Equip	0.8 scale factor	02/09/2020
	13	143	FEMA 461	Rigid Equip.	1 scale factor	02/09/2020
6. Bare Steel	1	143	VERTEQ-II (GR-63)	Rigid Equip.	0.25 scale factor	03/09/2020
	2	143	VERTEQ-II (GR-63)	Rigid Equip.	0.5 scale factor	03/09/2020
	3	143	VERTEQ-II (GR-63)	Rigid Equip.	0.375 scale factor	03/09/2020
	4	143	VERTEQ-II (GR-63)	Rigid Equip.	0.625 scale factor	03/09/2020
	5	143	VERTEQ-II (GR-63)	Rigid Equip.	0.875 scale factor	03/09/2020
	6	143	VERTEQ-II (GR-63)	Rigid Equip.	1 scale factor	03/09/2020
7. QuakeCoat – 1 Layer	1	143	VERTEQ-II (GR-63)	Rigid Equip.	0.25 scale factor	03/09/2020
	2	143	VERTEQ-II (GR-63)	Rigid Equip.	0.5 scale factor	03/09/2020
	3	143	VERTEQ-II (GR-63)	Rigid Equip.	0.75 scale factor	03/09/2020
	4	143	VERTEQ-II (GR-63)	Rigid Equip.	1 scale factor	03/09/2020
9. QuakeCoat – 3 Layers	1	143	VERTEQ-II (GR-63)	Rigid Equip.	0.25 scale factor	03/09/2020
	2	143	VERTEQ-II (GR-63)	Rigid Equip.	0.5 scale factor	03/09/2020
	3	143	VERTEQ-II (GR-63)	Rigid Equip.	0.75 scale factor	03/09/2020
	4	143	VERTEQ-II (GR-63)	Rigid Equip.	1 scale factor	03/09/2020
10. QuakeCoat (nominal)	1	143	VERTEQ-II (GR-63)	Rigid Equip. (Kc = 0)	0.25 scale factor	03/09/2020
	2	143	VERTEQ-II (GR-63)	Rigid Equip. (Kc = 0)	0.5 scale factor	03/09/2020
	3	143	VERTEQ-II (GR-63)	Rigid Equip. (Kc = 0)	0.75 scale factor	03/09/2020
	4	143	VERTEQ-II (GR-63)	Rigid Equip. (Kc = 0)	1 scale factor	03/09/2020
	5	143	VERTEQ-II (GR-63)	Rigid Equip. (Kc = 1)	1 scale factor	03/09/2020
	6	143	VERTEQ-II (GR-63)	Rigid Equip. (Kc = 1)	1.25 scale factor	03/09/2020
	7	143	VERTEQ-II (GR-63)	Rigid Equip. (Kc = 10)	1 scale factor	03/09/2020

Figure 4.9 (cont.): Real-time hybrid simulation test matrix for evaluating FIS-equipment interactions

zero and nominal rolling surface thicknesses respectively. The former of these was subject to the motion at two different intensities (1× and 2×) while the latter was also tested to 3× the impulse wave. The system's responses shown in Figure 4.10 are as expected for a free vibrations test for a system with little-to-no rolling resistance—the impulse causes a displacement that decays asymptotically with time . While the input excitement is twice as large in Figure 4.10(b), its maximum displacement is approximately 3 times larger than that of Figure 4.10(a). The acceleration values, however, are almost the same, which is due to the RP bearings conical (constant slope) design. The difference in the acceleration for both cases relies on the time it takes for the response to dissipate and reach zero. In both cases, the first acceleration cycles resemble a square-wave—like the input motion—and slowly become more sinusoidal until reaching zero. The influence of the enhanced rolling resistance can be noted when comparing this response to that shown in Figure 4.11. For this case, the base impulse (1×) is enough to barely move the system 0.08 in. Moreover, the increased rolling resistance causes the system to come to rest after approximately two cycles of exponentially decreasing displacements. For the 2× impulse wave case, the displacement of the bare steel rolling surface comes to rest after approximately 28 seconds while for the QuakeCoat rolling surface the same happens in less than 3 seconds. The acceleration time-histories of the tests performed using the QuakeCoat surface are similar for both × and 2× (see right-hand-side of Figure 4.10. At first, they the response is a first acceleration from the 0.25 seconds impulse followed by oscillations with local maximum and minimum accelerations at the maximum and minimum displacements where maximum displacements were reached.

The Bare Steel surface was also tested using the model for protecting flexible equipment with a tributary load of 240 lbs at two different intensities: 1× and 2×. As well, as described in Section 4.3.2, the frequency at the base of the equipment being isolated was parameterized to better understand the FIS-equipment interactions. The kinematic be-

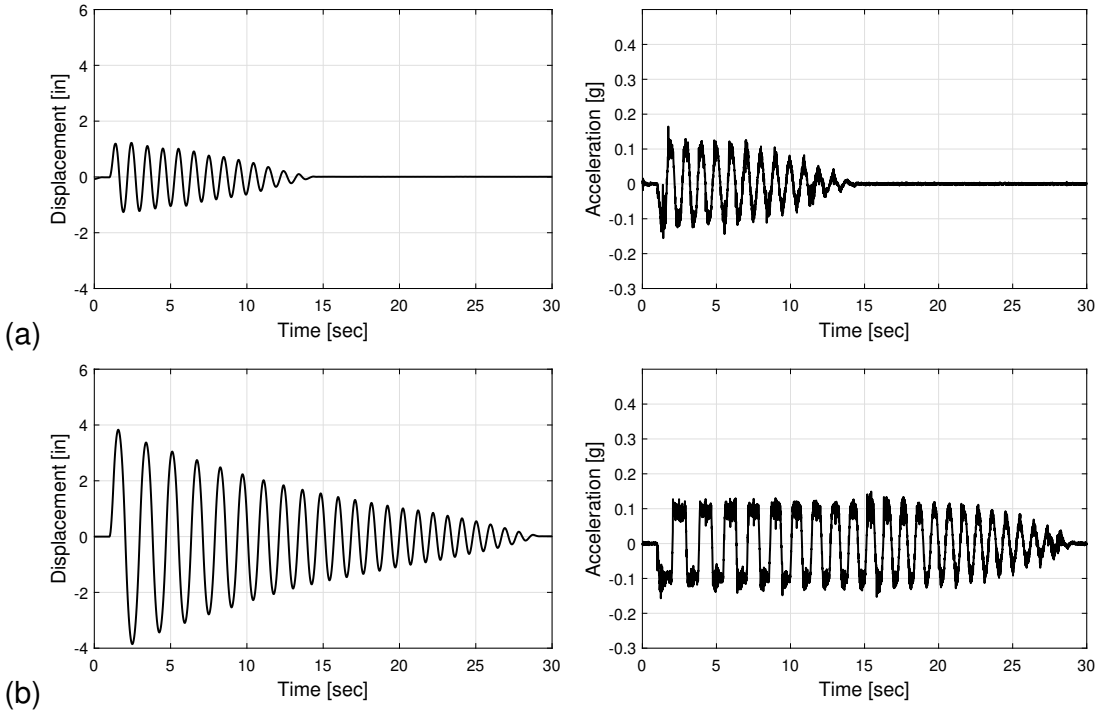

Figure 4.10: Displacement (left) and total acceleration (right) time-histories at the base of rigid equipment for experimental setup with Bare Steel rolling surface subject to impulse wave amplified (a) 1× and (b) 2×

havior of its 3DOF was recorded, two of which are translational (horizontally) and one rotational. The translational DOFs represent the top of the RP isolator unit/base of the equipment and the top of the equipment. From this, the displacement and acceleration time-histories are shown in Figures 4.12 and 4.13 for 1× and 2× scaling of the square-impulse wave respectively with varying equipment frequency (a-d). From these figures, it can be concluded that having more flexible equipment (i.e., equipment with lower frequency) does affects the response of the RP isolator unit. The displacement response, for instance, is affected by two overlapping modes. Figures 4.12(a) and 4.13(a) show that the top of the isolator/base of the equipment does not move sinusoidally. Rather, the low frequency of the equipment appears to partake in the isolator's performance by decreasing the peak displacements and increasing the period of the system.

When compared to the results of the higher-frequencies equipment, the 1-Hz case

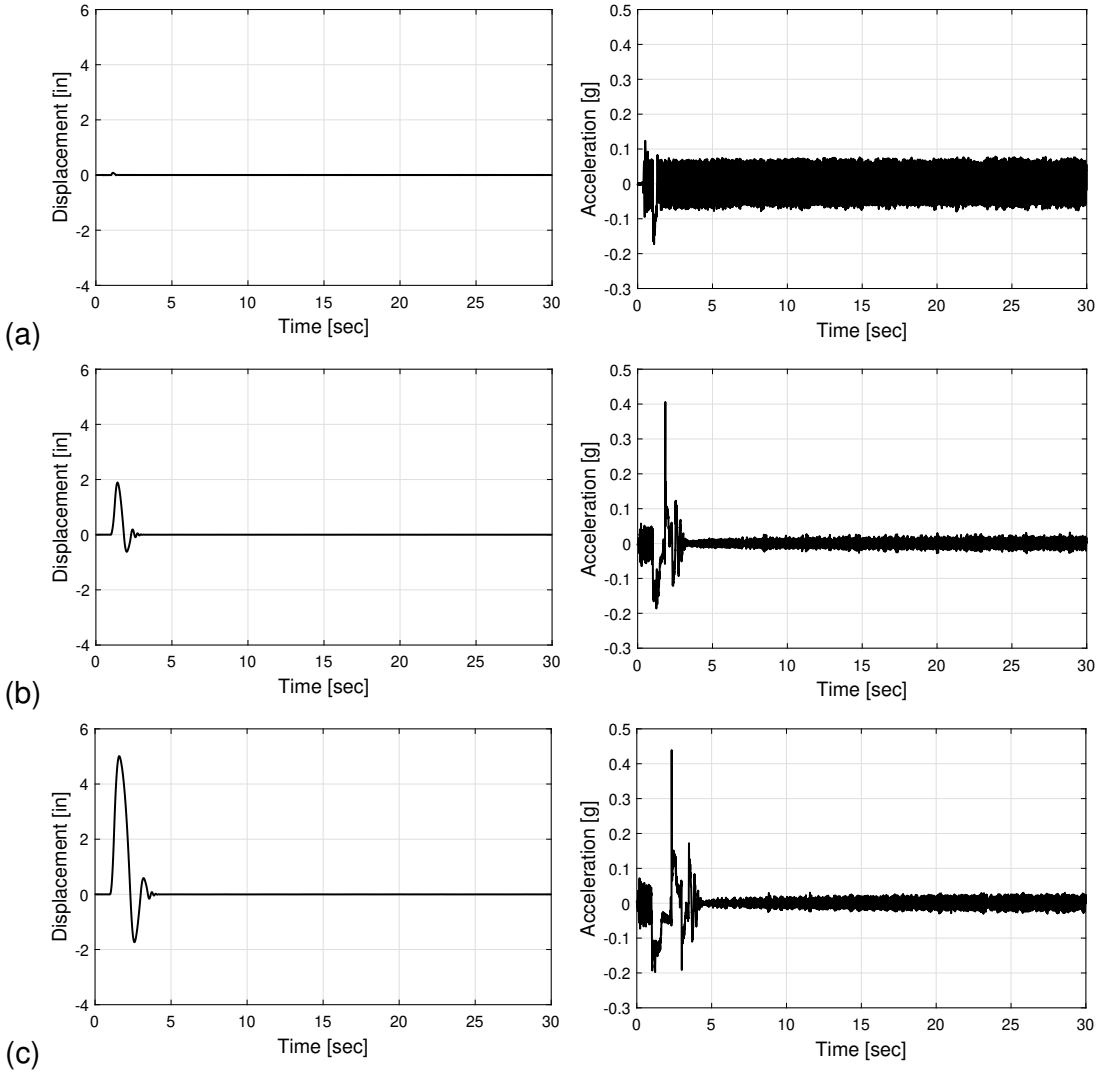

Figure 4.11: Displacement (left) and total acceleration (right) time-histories at the base of rigid equipment for experimental setup with QuakeCoat rolling surface subject to impulse wave amplified (a) 1×, (b) 2×, and (c) 3×

shows a higher equipment drift for both 1× and 2× waves. Furthermore, the system's response elongates for the cases with higher frequency. For instance, in Figure 4.13, the RP bearing takes about 25 seconds to come to rest for the 1 and 2 Hz cases, while for the 5 and 10 Hz ones it takes over 30 seconds—even longer than what was expected from the experiments with the rigid equipment model. Regarding the accelerations, these figures show that for the less flexible equipment the maximum accelerations at both ends of the equipment remains somewhat constant for a longer period while for

the more flexible cases this decays similar to the displacement decay. On the other hand, the accelerations at the top of the equipment for the cases with 1-Hz frequency take the form of a sinusoidal wave faster than those with higher frequency—which are more square-like for the first portion of the motion.

Since when the frequency of the equipment is 10 Hz this can be thought off as effectively rigid, theoretically Figure 4.10(a) should be the same as Figure 4.12(d). Similarly, the behavior represented in Figure 4.10(b) should be the same as that in Figure 4.13(d). For the tests under the square impulse wave (1×), the behavior is very similar although the damping for the 3DOF model is higher. This case comes to rest at about 14.3 seconds while the test with the SDOF model lasts takes about one extra second to come to rest. Furthermore, the maximum displacement of the former is about 7% larger than that of the latter. For the scale wave (2×) the maximum displacement is about 16% higher for the flexible equipment model than for the rigid one.

4.5.2 FEMA 461

The model considering rigid equipment was used to test the experimental setup under the narrow-band randomly generated wave described by Building Seismic Safety Council (2007) (see Figure 4.7). The experimental setup was subject to experiments withstanding the 240-lbs tributary mass in all 5 different rolling surfaces (see testing specimens 1–5 in Table 2.1). As per the the testing protocol, the motion was scaled to at least three different intensities varying at least 25% from one another. Moreover, two intensities for which the system went over the set displacement and/or velocity limits given by the actuator. For the tests in which the Bare Steel rolling surface was used, these intensities were: 0.167, 0.25, 0.33, 0.4, 0.5, 0.625, and 0.75. For the enhanced-damping specimens, the intensities used were 0.4, 0.5, 0.625, 0.8, 1, and 1.25 (if applicable). For the nominal Quakecoat tests, 0.4 was substituted by 0.33 for the first tests. Figure 4.14 shows the displacement and acceleration time-histories for a test using a

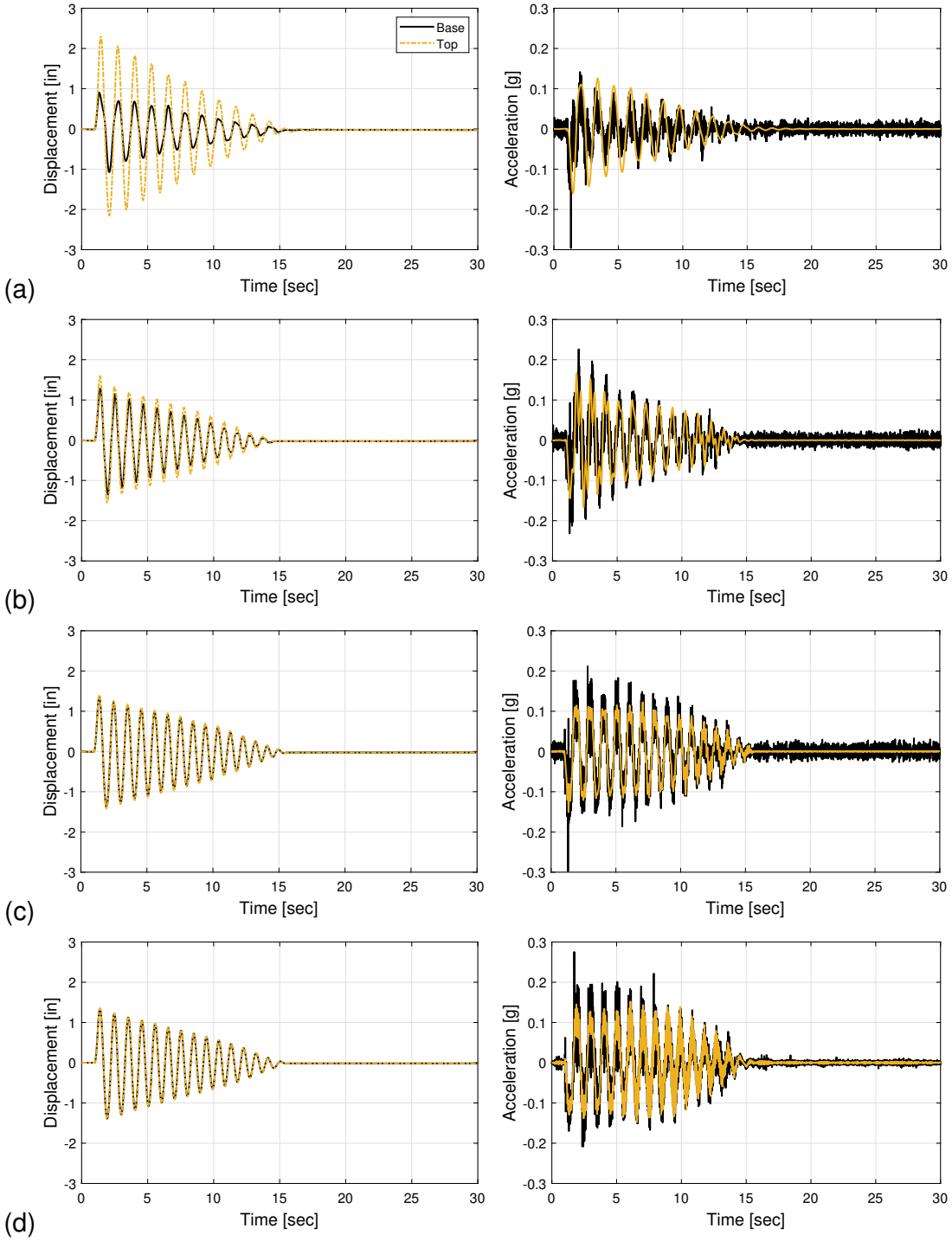

Figure 4.12: Displacement (left) and total acceleration (right) time-histories at the base and top of flexible equipment for experimental setup with a Bare Steel rolling surface subject to the impulse wave amplified 1× with varying equipment frequency: (a) 1, (b) 2, (c) 5, and (d) 10 Hz

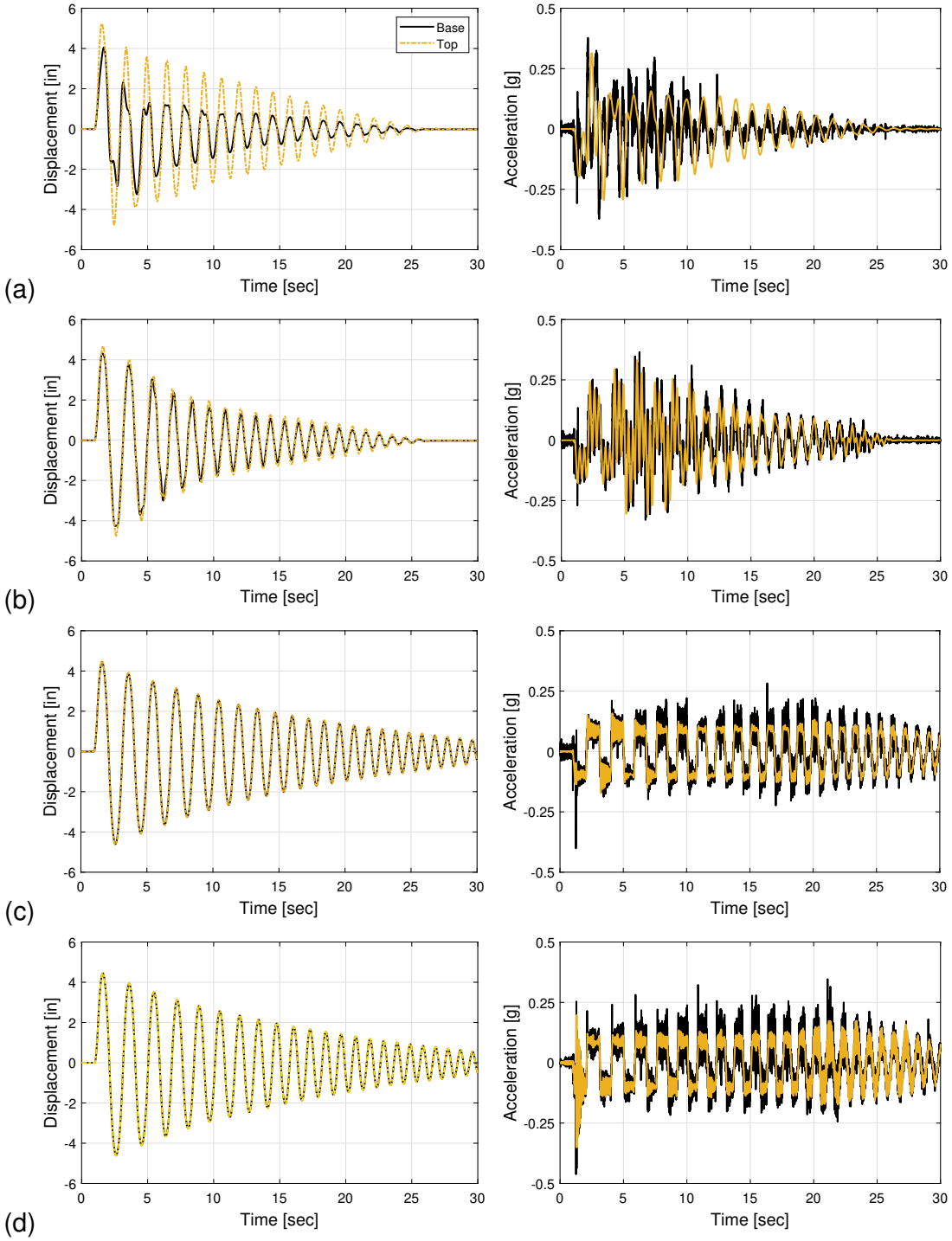

Figure 4.13: Displacement (left) and total acceleration (right) time-histories at the base and top of flexible equipment for experimental setup with a Bare Steel rolling surface subject to the impulse wave amplified $2\times$ with varying equipment frequency: (a) 1, (b) 2, (c) 5, and (d) 10 Hz

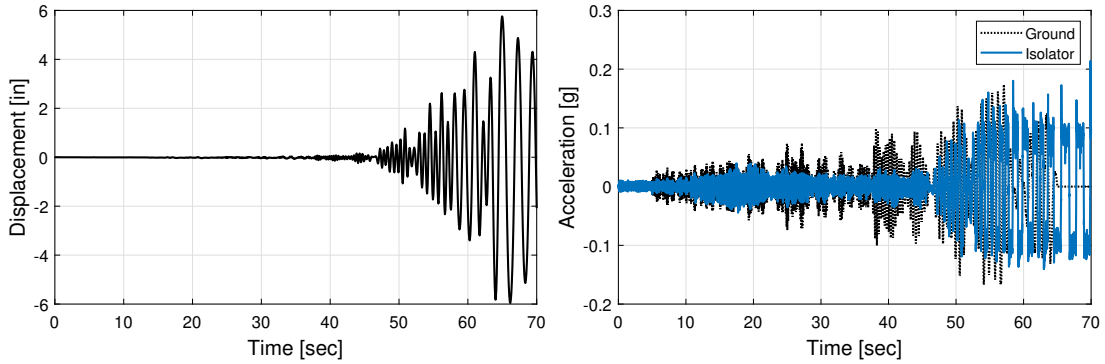

Figure 4.14: Displacement (left) and total acceleration (right) time-histories for the experimental setup with the Bare Steel rolling surface subject to FEMA461 wave scaled down to 0.5

Bare Steel rolling surface subject to 0.5× the input excitement. The acceleration time-history shows that for the lower accelerations (i.e., higher frequencies), the response at the top of the RP isolator unit is significantly lower than the input excitation. Nevertheless, for larger accelerations (i.e., lower frequencies) the equipment's response is almost the same as the input excitation. Even after the input acceleration goes to zero, the top of the RP isolator keeps moving at large displacements and accelerations (i.e., freely vibrates).

For all the test specimens subject to this wave, the total maximum absolute acceleration was obtained at a given intensity. Figure 4.15 shows said maximum accelerations for all the test specimens, as well as the maximum peak ground acceleration (PGA) for a given intensity. Let it be noted that for every rolling surface the experiments with the two highest scale factors were not completed. For these, the actuator hit a displacement limit (6 in.) and the test was stopped. The values obtained shown are from the data obtained before the tests were stopped. From the testing standard, the maximum response at each intensity should meet but not exceed more than 30% the input motion's maximum response spectra (ATC, 2007)—PGA in this case. However, as shown in Figure 4.15, the peak total acceleration is larger for all test specimens than the PGA for intensities equal or lower than 0.625. Thus, the C3-240 (3 layers) rolling surface is

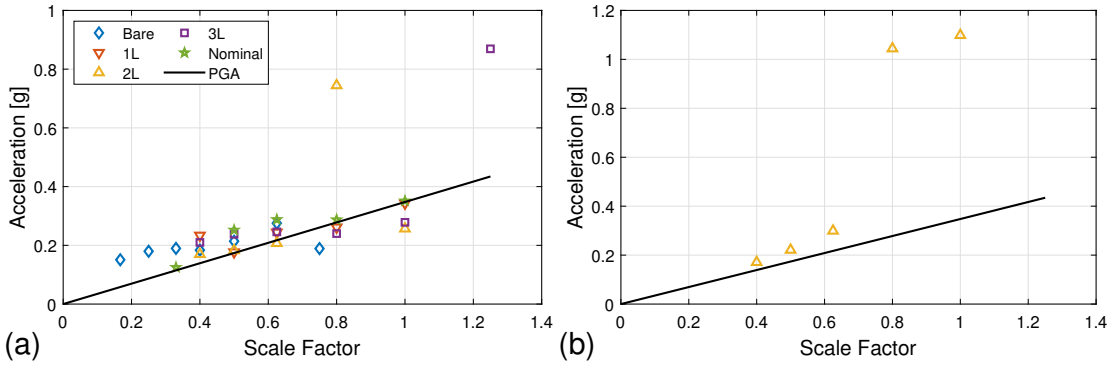

Figure 4.15: Varying FEMA-461 wave intensities versus its PGA and the isolator's peak total accelerations for different rolling surface under (a) 240- and (b) 143-lbs tributary load

the only one for which the maximum acceleration is lower than the PGA for a complete test. Even then, however, its acceleration is significantly larger than 30% PGA scaled down to 0.8.

Figure 4.15(b) shows the peak total acceleration at given intensities for the nominal-thickness rolling surface with a 143-lbs tributary load. From this, it can be noted that reducing the tributary load decreases the peak total accelerations. However, these are still very close to their respective PGAs. At last, the RP isolator unit did not meet the performance specifications given in the FEMA 461 testing standard.

4.5.3 VERTEQ-II

The VERTEQ-II wave was used to test the experimental setup for both rigid and flexible equipment models. For the former, all 5 different rolling surfaces were tested while for the latter the nominal QuakeCoat and the Bare Steel surfaces were used. Figure 4.16 shows the displacement and acceleration time-histories for a nominal QuakeCoat subject to 0.75× the VERTEQ-II input excitation. The acceleration time-history shows the response of the equipment being isolated too. For said equipment, the acceleration at its base is about half the maximum PGA of the scaled input motion which demonstrates the equipment is effective isolated. The peak total acceleration for all rolling surfaces are shown at different intensities in Figure 4.17. For each rolling surface, the second

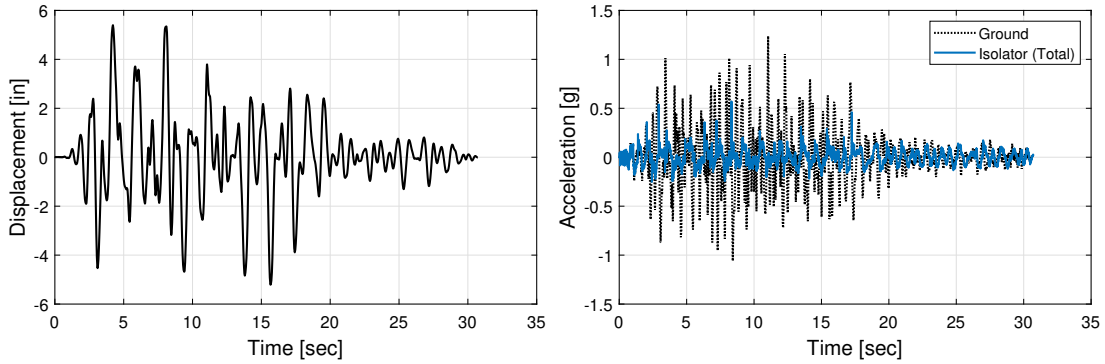

Figure 4.16: Displacement (left) and total acceleration (right) time-histories for the experimental setup with the nominal QuakeCoat rolling surface subject to VERTEQ-II wave scaled down to 0.75

to largest scale factor was the limiting experiment—the last experiment that was successfully performed. The experiments at the largest scale factors, then, were incomplete because of displacement or velocity limits set in the actuator. Regardless, a peak total acceleration value was obtained between the experiment's beginning and termination. It can be noted in this figure that the total accelerations are higher for the specimens with enhanced damping. However, for the tests with a lower tributary mass (Figure 4.17(right)) the Bare Steel reaches accelerations much closer to those of the damped rolling surfaces. In general, higher accelerations are present as well when the specimens are tested with the smaller tributary load. The systems, at last, appear to better-isolate equipment for higher intensities. With regards to the performance of the different testing specimens with respect the input excitation's intensity, the damped cases are able to withstand higher intensity disturbances. From Figure 4.17(left), the bare steel stops at 0.6 whereas the damped cases go up to 1. This is the trade off—reduced isolation performance but with reduced displacement responses.

The experimental setup was also implemented in the 3DOF model for the VERTEQ-II wave. The displacement and acceleration time-histories for the BareSteel and QuakeCoat rolling surfaces when tested using the model for protecting flexible equipment at 1, 2, 5, 10 Hz are shown in Figures 4.18 and 4.19, respectively. The former was subject

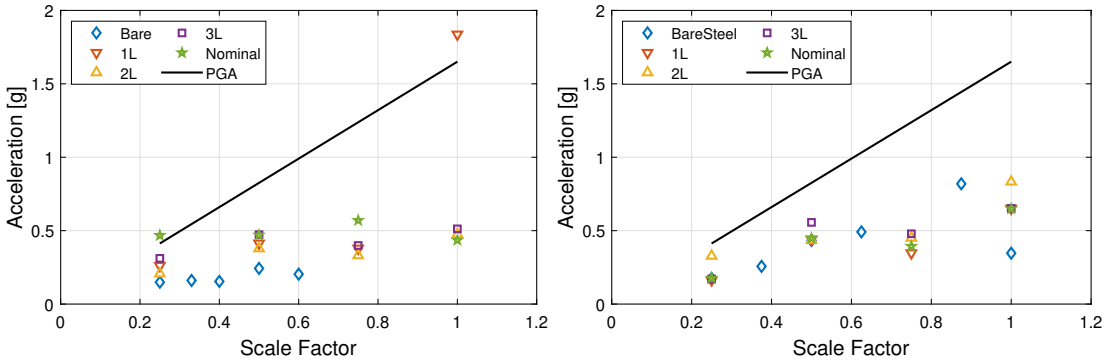

Figure 4.17: Varying VERTEQ-II wave intensities versus its PGA and the isolator's absolute peak accelerations for different rolling surfaces under 240 (left) and 143 lbs (right) of tributary load

to 0.4× while the latter was so to 0.75× the intensity of the VERTEQ-II acceleration record (see Figure 4.8). For the tests involving the more flexible equipment, it can be noted that the equipment's frequency interaction with the RP isolator unit yields smaller displacements and larger accelerations for the latter. On the other hand, in these tests larger displacements at the top of the equipment are developed. The total accelerations of the cases with lower frequency get out of phase with respect to the input acceleration more frequently than the higher frequency tests. The effect of the enhanced damping in the rolling surfaces can be observed in all of these tests too when comparing these figures—the latter reaches a maximum absolute displacement about 25% larger at an intensity almost 50% larger.

By calculating the difference of the maxima displacement at both ends of the equipment and normalizing it by its height, the drift ratio was found for every experiment. Figure 4.20 shows the peak equipment drift ratio at a given equipment frequency for both rolling surfaces. The drifta are lower for the Bare Steel surface because its response is to a lower intensity excitation. While the gap between the the percentage drift becomes larger as the equipment frequency increases, the drift for cases other than $f = 1$ Hz is negligible.

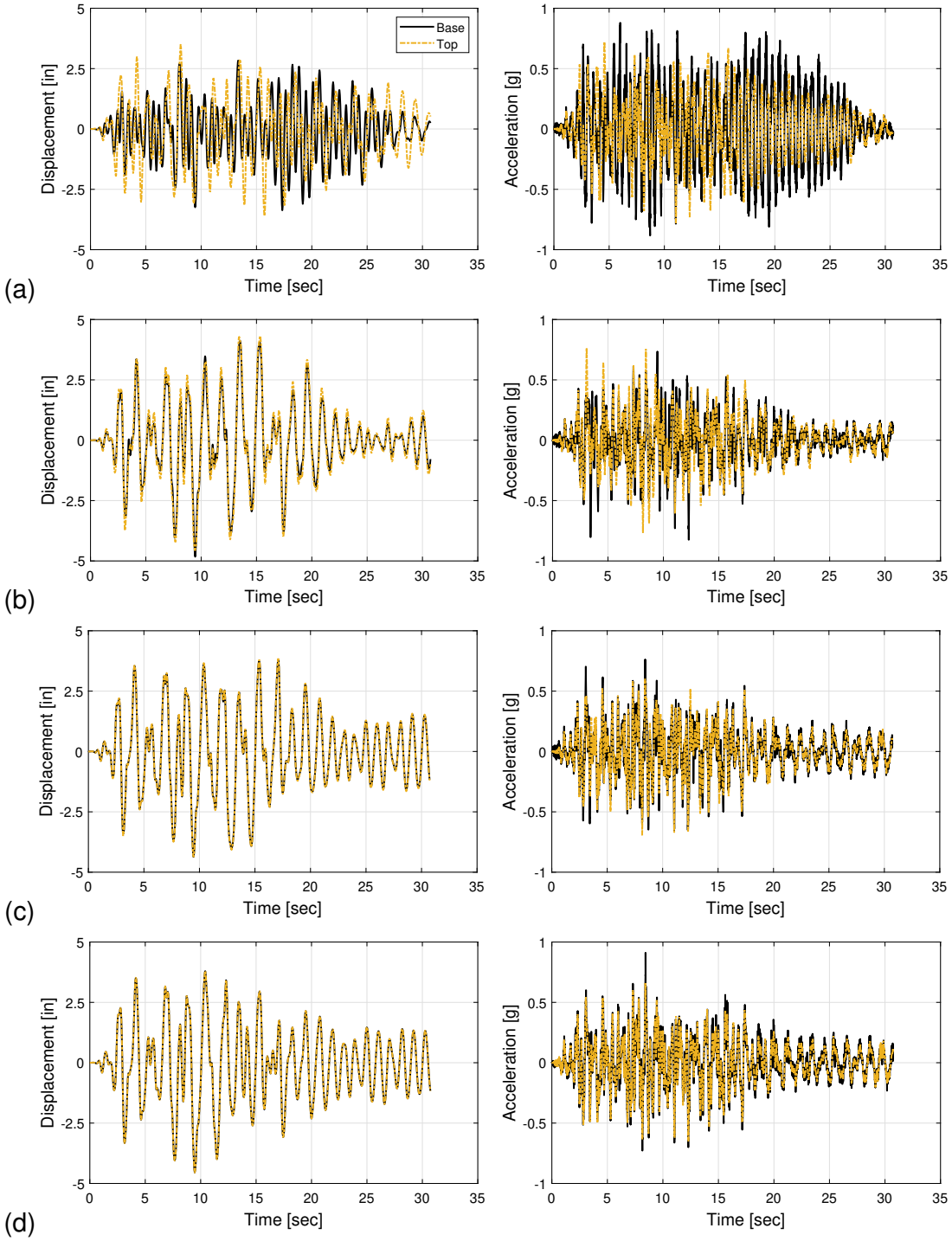

Figure 4.18: Displacement (left) and total acceleration (right) time-histories at the base and top of flexible equipment for experimental setup with a Bare Steel rolling surface subject to the VERTEQ-II wave scaled to 0.4 with varying equipment frequency: (a) 1, (b) 2, (c) 5, and (d) 10 Hz

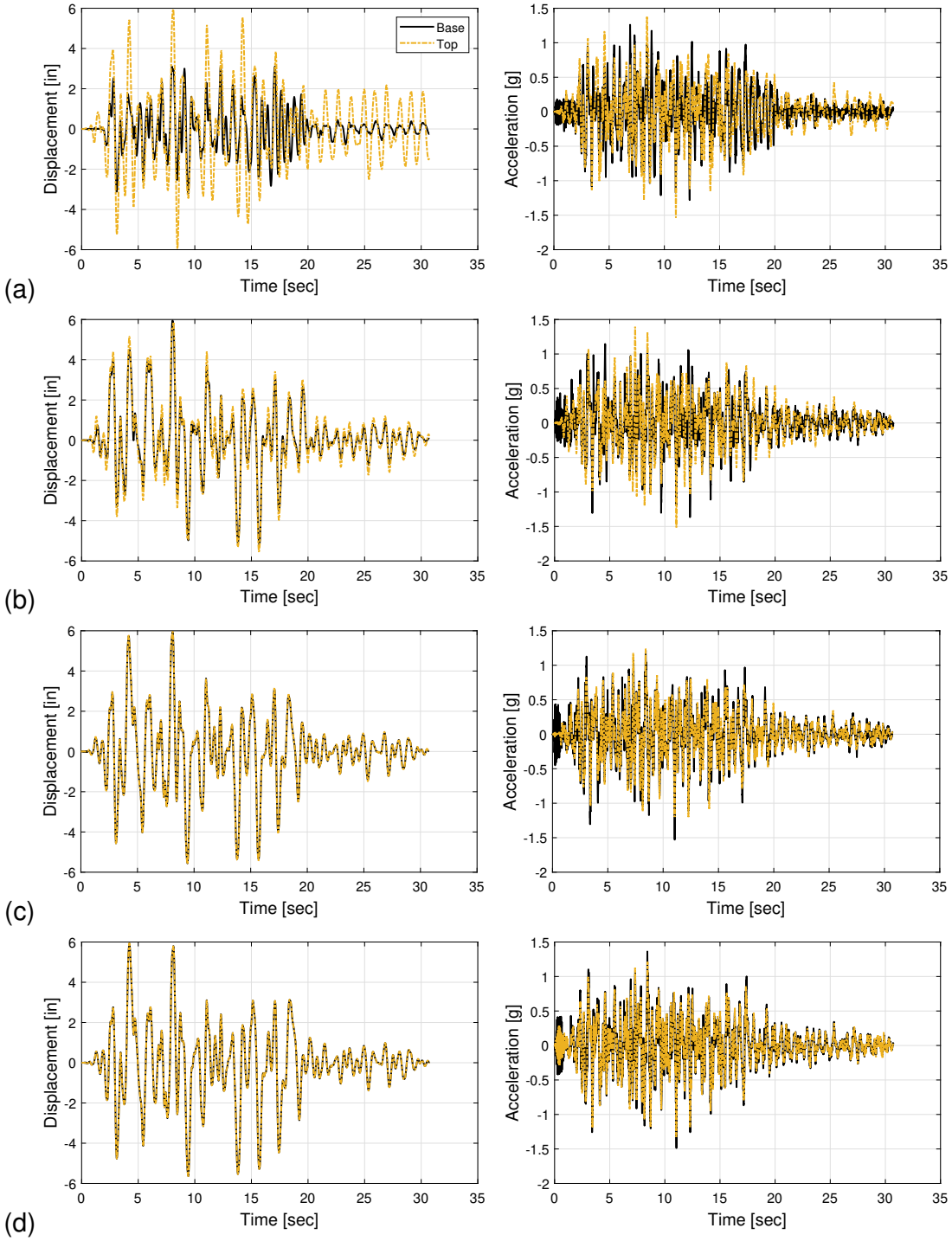

Figure 4.19: Displacement (left) and total acceleration (right) time-histories at the base and top of flexible equipment for experimental setup with a QuakeCoat rolling surface subject to the VERTEQ-II wave scaled to 0.75 with varying equipment frequency: (a) 1, (b) 2, (c) 5, and (d) 10 Hz

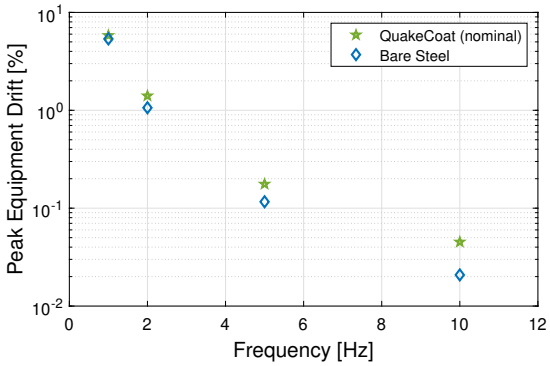

Figure 4.20: Percent drift across the equipment at a given frequency for experimental setup subject to $0.4\times$ (BareSteel) and $0.75\times$ (nominal QuakeCoat) VERTEQ-II wave

4.6 Summary

In this chapter, FIS-equipment interactions were studied and discussed. Two FEM models were developed to study FIS-equipment interactions—one for rigid and one for flexible equipment. The experimental setup was linked to said models and then tested through RTHS. To properly perform RTHS, the kinematic behavior of the experimental setup was modeled into an equation of motion of the system. The model of an RP isolator unit for protecting rigid equipment was subject to 3 different input excitations. The model of an RP isolator unit for protecting flexible equipment—$f = 1, 2, 5$, and 10 Hz—was subject to 2 different input excitations. The tests involving the model for protecting rigid equipment demonstrated the effect of rolling surfaces with enhanced damping. As well, these showed the applicability of RTHS tests for the study of FISs. For isolated equipment with a frequency of its own, it was found that the bearing's performance was affected for low-frequency equipment (i.e., 1 and 2 Hz at the base of the equipment). In the following chapter, interactions between a building and a FIS are studied and discussed.

Chapter 5
Building–FIS Real-Time Hybrid Tests

5.1 Overview

A rolling pendulum (RP)-based floor isolation system (FIS) was modeled within a numerically modeled 3-story moment-resisting frame (MRF) and placed in all three levels. The model of the FIS is comprised of 350 bearings like the one that the experimental setup is designed to represent, and has a mass of 5% the structural floor's mass. The structure was subject to four past-earthquake records to different intensities to evaluate the FIS's overall performance and interactions with the building through real-time hybrid simulation (RTHS) tests. An impact model configuration of this system was developed too in order to provide additional stiffness numerically.

5.2 Problem Formulation

To evaluate the building-FIS interactions, the FIS is considered to isolate rigid equipment. For this, the RP isolator unit and the equipment are modeled as a single-degree-of-freedom (SDOF) system in a finite element environment, HybridFEM (Kolay et al., 2018). The structural system considered for this study is the 2D (N-S) benchmark 3-story MRF designed for the SAC project for the Los Angeles, California region (Ohtori et al., 2004).

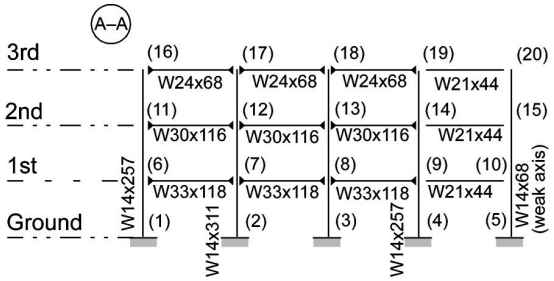

Figure 5.1: Three-story steel moment resisting frame N-S. Source: Ohtori et al. (2004)

5.2.1 Model of 3-Story MRF

Figure 5.1 shows the 3-story MRF upon which a finite-element model was developed in HybridFEM. The structure is made of steel beams and columns, and it has a total height of 39 ft (11.88 m) and four 30-ft (9.15-m) bays. The seismic mass of the first and second level is 65.5 kip s^2/ft (9.57×10^5 kg) while the roof's is 71.0 kip s^2/ft (1.04×10^6 kg), all of which are distributed along two MRFs in the N-S direction.

In total, the MRF is modeled with 30 nodes as shown in Figure 5.2. Node 31 represents the base of the isolated equipment. The center column (nodes 9, 10, 12, and 12) carry the seismic mass corresponding to one MRF. The mass of the rest of the nodes is modeled as negligible. The nodes connecting the MRF to the ground are fixed. Nodes 21–26 are defined to act as pin connections and are restrained to have the same degrees of freedom as nodes 14–20 in the x and y direction. The steel is modeled as a bilinear elastoplastic material with an initial modulus of elasticity of 29,000 ksi (200 GPa), a yield strength of 50 ksi (345 MPa), and a post-yielding stiffness ratio of 0.1. The beams and columns for the MRF are defined as *forceBeamColumn* elements, and their properties are defined as per the W-sections shown in Figure 5.1. These elements are set to be integrated under a Lobatto scheme with 5 element iterations with a tolerance factor of 10^{-16}. The elements are set to carry over unbalanced section capabilities. The stiffness proportional damping contribution of these elements is set to use the stiffness at the current step of integration. Since the mass is lumped in the nodes of the central

columns, the elements do not carry any load per unit length.

Moreover, a lean-on column (nodes 27–30) is defined off-set to the right of the right-most bay to model the MRF's P–Δ effects. The elements of this are defined as *elasticBeamColumn* elements along with *dummy* elements. The former have stiffness proportional damping—given by $\beta_K = 0.0005$ and $\alpha_M = 0$—as well as a modulus of elasticity of 29,000 ksi (200 GPa), and negligible element area and moment of inertia. The elements comprising the lean-on column have assigned weights (vertical loads) to generate P–Δ effects. Note that nodes 28, 29, and 30 are conditioned to have the same equal DOFs as nodes 10, 11, and 12 respectively (i.e., the lateral displacement of the former is slaved to the latter). Besides the damping assigned to the *forceBeamColumn* and *elasticBeamColumn* elements, 2% modal damping was applied to the first 4 modes of the structure.

Regarding the modelling of the RP isolator unit with rigid equipment, the SDOF model described in Section 4.3.1 was adapted to be used in this series of tests. It was placed in the third bay—left to right—at all three different floor-levels (i.e., 1st, 2nd, and roof), and was connected through an experimental element carrying 350× the real tributary mass held by the experimental setup (M), which this element represents. Essentially, by doing this, a 50-kip RP-based FIS (approximately 5% the structural floor's weight) is modeled to respond horizontally to the uniaxial lateral loading. At last, the 3-story MRF (including the lean-on column) along with the RP isolator unit possess 59 unique degrees-of-freedom.

The challenge presented in Section 4.3, in which the mass of the lower platform, m, needs to be compensated to account for external inertial effects was neglected for these tests. Originally, testing to corroborate the accuracy of this assumption was thought of but, due time constraints, it was not possible. The integration of this model was performed by using the MKR-α algorithm (Kolay et al., 2015; Kolay and Ricles, 2016,

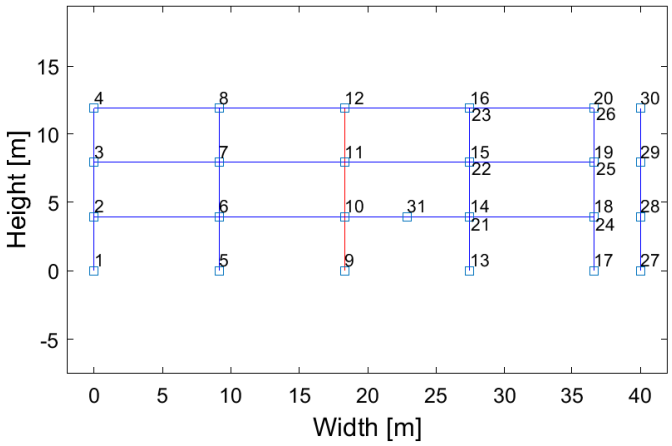

Figure 5.2: Model of 3-story MRF with RP-based FIS for protecting rigid equipment integrated in the 1st level (node 31)

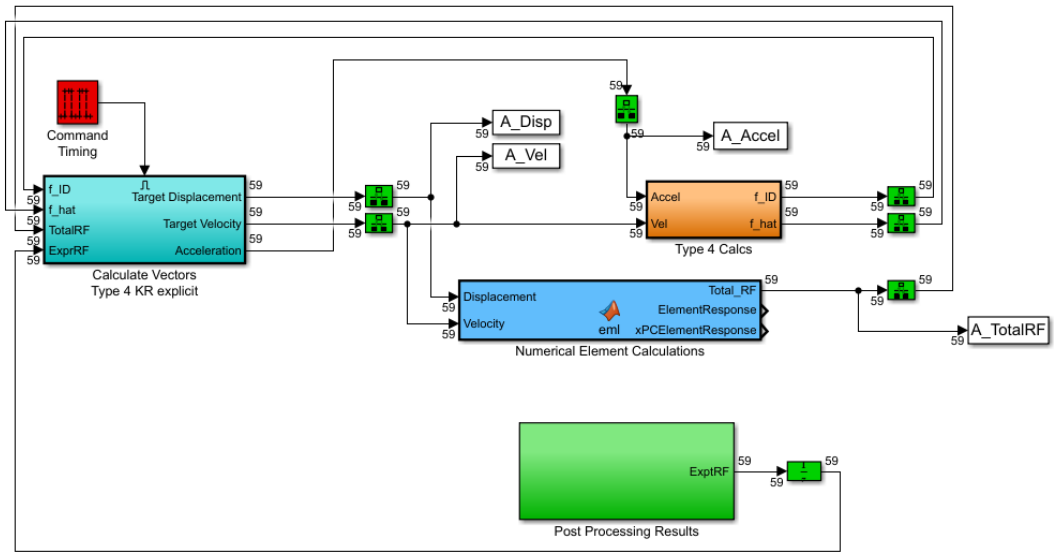

Figure 5.3: Simulink model containing the MKR-α algorithm used for 3-story MRF tests

2014) at 1024 Hz with 6-step interpolations. The control parameter for numerical dissipation, ρ, was set to 0.5 for all the tests involving the model herein described. Figure 5.3 shows the Simulink model in which the algorithm's integration in real-time and the signal generation of the tests was performed.

5.2.2 Impact Model Configuration

A 5-in. gap was placed in the Simulink model to (numerically) provide additional stiffness, k_c, to the RP isolator unit (Tehrani and Harvey, 2019; Bin et al., nd). This gap acts as a bumper, for which when the absolute value of the displacement commanded to the actuator, d, is greater than 5 in., a force resulting from $k_c \times |d - 5|$ is added to or subtracted from the load recorded in the S-beam load cell. Thus, reducing the value calculated for the next displacement. The nominal value assigned to k_c is 13.75 lb/in., which was obtained from the initial stiffness of a QaukeCoat rolling surface during the characterization tests (see Chapter 3). The value of k_c was scaled to 0×, 1×, 10×, and 20× throughout the testing sequence.

5.3 Test Protocol

All of the tests for evaluating building-FIS interactions were performed using specimen C2-143—QuakeCoat with 2 layers of thickness supporting a 143-lb tributary mass. Following the evaluation criteria designed for the structure of interest (Ohtori et al., 2004), the experimental setup was subject to four past-earthquake records:

- El Centro, Imperial Valley Irrigation District substation, 1940;
- Hachinohe, Hachinohe City station (Tokachi-oki earthquake), 1968;
- Northridge, Sylmar County Hospital station, 1994; and
- Kobe, Kobe Japanese Meteorological Agency station (Hyogoken Nanbu earthquake), 1995.

Each ground motion was scaled to three different intensities (0.5×, 1×, and 1.5×)

5.4 Test Matrix

Figure 5.4 shows the sequence of tests performed for evaluating building-FIS interactions. Every earthquake record was originally planned to be tested to the intensities

BUILDING	TEST #	TEST WEIGHT (lb)	ROLLING SURFACE	EQUIPMENT	ISOLATOR BEARING LOCATION	NUMBER ISOLATION BEARINGS	BUMPER SCALE	INPUT MOTION	SCALE FACTOR	DATE
3-Story Steel MRF (Ohtori et al., 2004)	1	143	8.QuakeCoat (2L)	Rigid Equip.	1st Story	350 (5% of floor)	0	El Centro	0.5	02/09/2020*
	2	143	8.QuakeCoat (2L)	Rigid Equip.	1st Story	350 (5% of floor)	0	El Centro	1	02/09/2020*
	3	143	8.QuakeCoat (2L)	Rigid Equip.	1st Story	350 (5% of floor)	0	El Centro	0.5	09/02/2020
	4	143	8.QuakeCoat (2L)	Rigid Equip.	1st Story	350 (5% of floor)	0	El Centro	1	02/09/2020*
	5	143	8.QuakeCoat (2L)	Rigid Equip.	1st Story	350 (5% of floor)	0	Hachinohe	0.5	09/02/2020
	6	143	8.QuakeCoat (2L)	Rigid Equip.	1st Story	350 (5% of floor)	0	Hachinohe	1	09/02/2020
	7	143	8.QuakeCoat (2L)	Rigid Equip.	1st Story	350 (5% of floor)	0	Hachinohe	1.5	09/02/2020*
	8	143	8.QuakeCoat (2L)	Rigid Equip.	1st Story	350 (5% of floor)	0	Northridge	0.5	09/02/2020*
	9	143	8.QuakeCoat (2L)	Rigid Equip.	1st Story	350 (5% of floor)	0	Kobe	0.5	09/02/2020
	10	143	8.QuakeCoat (2L)	Rigid Equip.	1st Story	350 (5% of floor)	1	El Centro	0.5	09/02/2020
	11	143	8.QuakeCoat (2L)	Rigid Equip.	1st Story	350 (5% of floor)	1	El Centro	1	09/02/2020
	12	143	8.QuakeCoat (2L)	Rigid Equip.	1st Story	350 (5% of floor)	1	El Centro	1.5	09/02/2020*
	13	143	8.QuakeCoat (2L)	Rigid Equip.	1st Story	350 (5% of floor)	10	El Centro	1	09/02/2020
	14	143	8.QuakeCoat (2L)	Rigid Equip.	1st Story	350 (5% of floor)	10	El Centro	1.5	09/02/2020
	15	143	8.QuakeCoat (2L)	Rigid Equip.	2nd Story	350 (5% of floor)	0	El Centro	0.5	09/02/2020
	16	143	8.QuakeCoat (2L)	Rigid Equip.	2nd Story	350 (5% of floor)	0	El Centro	1	09/02/2020*
	17	143	8.QuakeCoat (2L)	Rigid Equip.	2nd Story	350 (5% of floor)	1	El Centro	0.5	09/02/2020
	18	143	8.QuakeCoat (2L)	Rigid Equip.	2nd Story	350 (5% of floor)	1	El Centro	1	09/02/2020*
	20	143	8.QuakeCoat (2L)	Rigid Equip.	2nd Story	350 (5% of floor)	10	El Centro	0.5	09/02/2020
	21	143	8.QuakeCoat (2L)	Rigid Equip.	2nd Story	350 (5% of floor)	10	El Centro	1	09/02/2020*
	23	143	8.QuakeCoat (2L)	Rigid Equip.	3rd Story	350 (5% of floor)	0	El Centro	0.5	09/02/2020*
	24	143	8.QuakeCoat (2L)	Rigid Equip.	3rd Story	350 (5% of floor)	1	El Centro	0.5	09/02/2020*
	25	143	8.QuakeCoat (2L)	Rigid Equip.	3rd Story	350 (5% of floor)	10	El Centro	0.5	09/02/2020*
	26	143	8.QuakeCoat (2L)	Rigid Equip.	3rd Story	350 (5% of floor)	20	El Centro	0.5	09/02/2020*

* Test was stopped due displacement or velocity limits was hit

Figure 5.4: Real-time hybrid simulation tests matrix for evaluating building-FIS interactions

described in Section 5.3. Nevertheless, once the experimental setup met a displacement, velocity, or acceleration limit placed in the actuator, tests were skipped for that specimen under higher intensities of the same excitation. At last, a total of 26 test were performed with the RP isolator unit places at different stories of the MRF described in previous sections.

5.5 Experimental Results

A total of 11 experiments ran throughout the totality of the earthquake record. The FIS's displacement went over a failsafe displacement limit—6 in.—placed in the code when no gap force was added for all 4 excitation records in the when placed in the roof. For the same case but with the FIS in the second floor, only the tests subject to 0.5× El Centro was not stopped. From these preliminary results and due to time constraints, it was decided to test the influence and reach of the gap element only for El Centro at the same three previously defined intensities.

From the RTHS tests, the displacement, velocity, and acceleration data of each DOF was recorded. From these, the performance of the RP isolator unit can be analyzed when compared to the excitations impact on the structural floor to which the unit was attached.

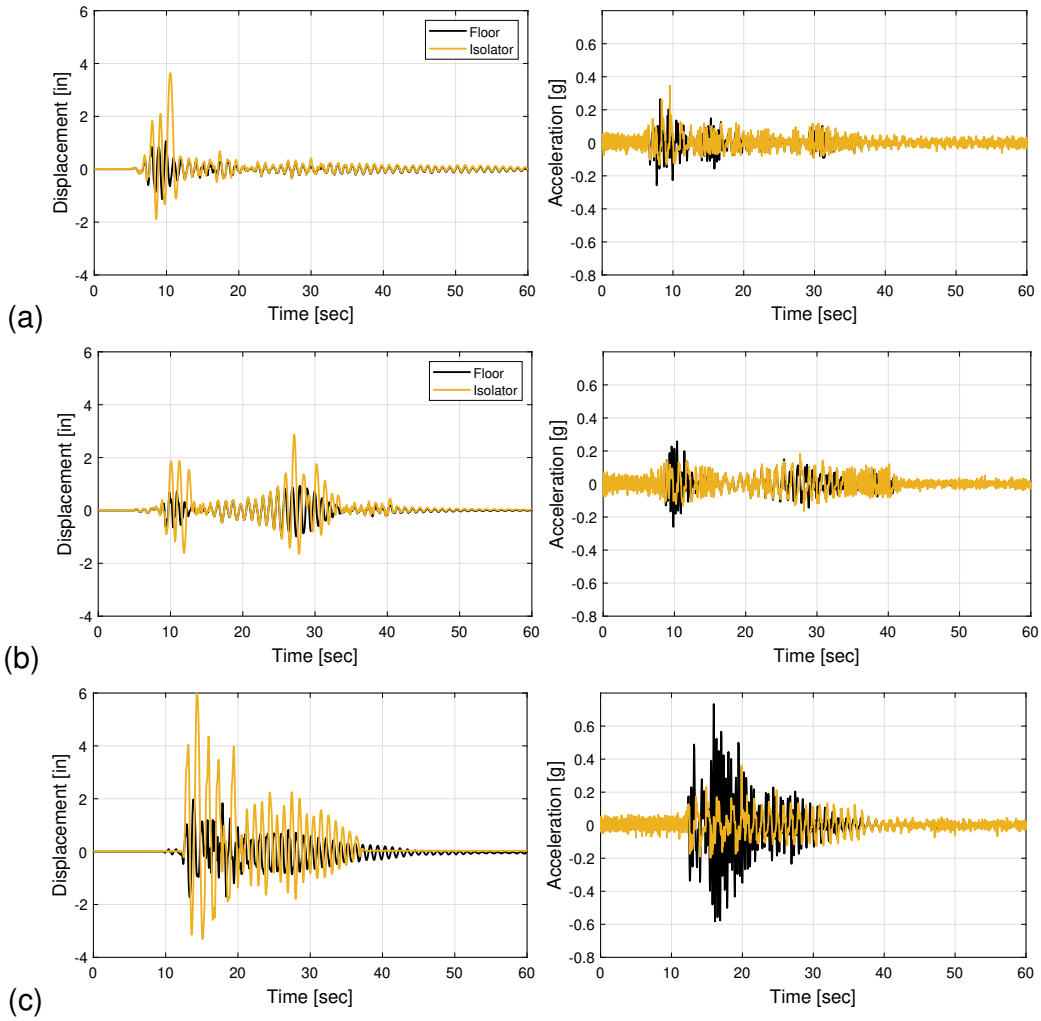

Figure 5.5: Displacement (left) and acceleration (right) time-histories of RP-based 50-kip FIS in the 1st level of a 3-story MRF and subject to $0.5\times$: (a) El Centro, (b) Hachinohe, and (c) Kobe earthquake records

Figure 5.5 shows that the the RP isolator unit's displacement relative to the ground motion is larger than the floor's. Nevertheless, the former reaches similar magnitudes to the latter relative rapidly. The RP isolator unit's acceleration is, in general, higher than that of the structural floor. However, the structural floor presents the highest total acceleration. Even more, as seen in Figure 5.5, when the floor reaches its maximum total accelerations the RP isolator unit's are significantly lower—about one half for El Centro, one-sixth for Hachinohe, and one-seventh for Kobe.

The influence of adding the gap element to the RP-base FIS when placed in the

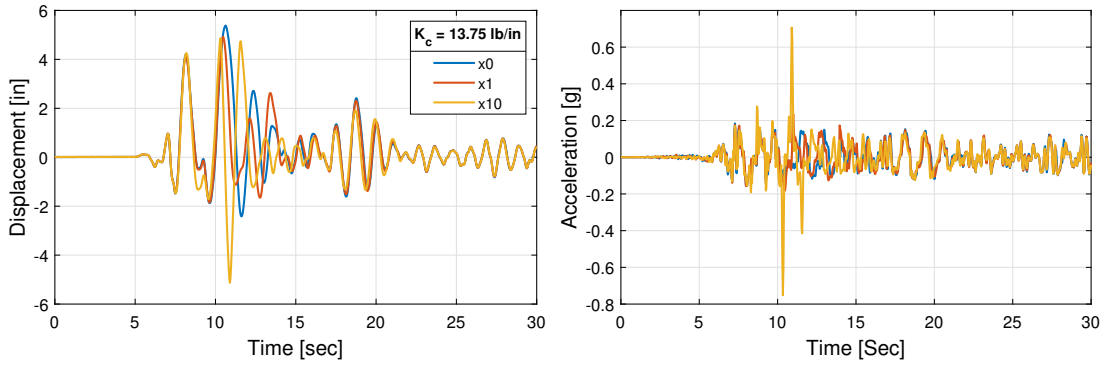

Figure 5.6: Displacement (left) and acceleration (right) time-histories of RP-based 50-kip FIS in the 1st level of a 3-story MRF and subject to $0.5\times$ El Centro

second story is shown in Figure 5.6. The FIS was subject to $0.5\times$ El Centro. The first 30 seconds of displacement and acceleration recorded by the experimental setup are shown in said figure. It can be noted that adding the gap element initially reduces the displacements calculated by the MKR-α algorithm, especially for the case in which the gap force is $k_c \times 10$. This, however, induces larger accelerations in the experimental setup since the change in the total force (i.e., gap plus load cell) is larger. As well, the reduction in the earlier displacements ends up increasing the later ones—the $k_c \times 10$ system still produces the largest displacement. For this case, the cycle in which the largest displacements are observed—peak-to-peak—has a period of approximately 1.20 seconds. For the system with $k_c \times 1$, this period is approximately 1.65 seconds ($\sim$17% larger), and for the system with no gap force it is around 1.76 (47% larger). This shortened period causes large spikes in the acceleration at those peak displacements for the $k_c \times 10$ system. At last, the displacement and acceleration records of both non-zero k_c systems eventually merge back with those of the zero-gap system.

Finally, the effect of the RP-based FIS can be analyzed by comparing the structure's maximum interstory drift ratio $\delta^{\max}$ with the RP-based FIS located in the 1st and 2nd levels versus the benchmark values of a the 3-story MRF on its own. This parameter is defined as the interstory drift of the above ground level divided by the height of each

of the associated stories (Ohtori et al., 2004). In the same way, it is also possible to compare whether the additional numerical stiffness in the FIS given by the gap force element influences the structure at all. Table 5.1 shows the $\delta^{\max}$ for the 3-story MRF with and without a FIS. To obtain the values for the latter, the model was simply subject to the input excitation of interest without any restoring force. While the mass of the RP-based FIS is modeled to be approximately 5% of that of the structural floor, $\delta^{\max}$ are not very different from one another for ever case herein presented. The largest difference is shown for 0.5× El Centro excitation with the isolator on the second level, for which the building-FIS maximum interstory drift is about 0.02% larger than that of the structure by itself. Regardless, the drift ratios remain very small. It also noticeable that the engagement and scaling of the gap element does not have a signifance in the influence of the RP-based FIS on the structure. If the gap force came from a physical element (i.e., an external source of stiffness placed in the RP bearing) this result could be different. At last, the 3-story MRF's behavior is not heavily affected by the 50-kip RP-based FIS.

5.6 Summary

In this chapter, building-FIS interactions were studied and discussed. A 3-story MRF was modeled in a FEM environment. The experimental setup was linked to this model

Table 5.1: Maximum interstory drift ratio of building without and with FIS in first and second levels

EQ Record	EQ Intensity	Location	k_c×	Building-FIS $\delta^{\max}$ (%)	Building Only $\delta^{\max}$ (%)
El Centro	1	First	1	1.67	1.67
	0.5	Second	10	1.02	1.04
	0.5	Second	1	1.02	1.04
	0.5	Second	0	1.02	1.04
	0.5	First	0	1.03	1.04
Hachinohe	0.5	First	0	0.91	0.91
Kobe	0.5	First	0	2.26	2.27

as a SDOF RP-based FIS composed of 350 bearing. As impact model was also numerically developed to provide additional stiffness to the RP-based FIS. The model and experimental set up were place in all three levels of the structure and subject to 4 different past-earthquake at different intensities records through RTHS. In total, 11 experiments were completed for the totality of the earthquake record. In general, the performance of the FISs was not adequate for high intensity excitations and when placed in the second level and roof of the 3-story MRF. The effects of the FIS—which accounted for 5% of the structural floor mass—were found to be negligible on the building studied (i.e., 3-story moment resisting frame).

Chapter 6
Summary, Conclusions, and Future Work

6.1 Summary and Conclusions

An experimental setup was designed to represent a rolling pendulum (RP) isolator unit under uni-axial lateral loading. In total, 240 characterization and real-time hybrid simulation (RTHS) tests were performed at the Natural Hazard Engineering Research Infrastructure Experimental Facility at Lehigh University. A test protocol was developed to perform characterization tests through a series of harmonic waves with various frequencies and amplitudes according to IEEE-693. Both conical and flat surfaces were used to investigate the rolling resistance induced by elastomeric coating, which is added layer by layer to bare steel rolling surfaces. Different levels of coatings were used to understand the effect of such in the damping of the isolator unit. A total of 15 unique configurations of the test setup were used in order to measure and evaluate the effects of the rolling surface's rolling resistance and shape, and the tributary mass on the bearing. For the RTHS tests, the experimental setup was subjected to synthetic and recorded ground motions in accordance with GR-63 and FEMA 461. To evaluate the FIS-equipment interaction, sensitive equipment was numerically modeled as a cantilever beam with both rigid and flexible characteristics. FIS-equipment interactions were only evaluated under synthetic floor motions. To evaluate the building-FIS interactions, a HybridFEM numerical model of a 3-story steel moment resisting frame was developed and used. For this, earthquake records at different intensities were applied as input motions. At

last, RTHS and the MKR-α algorithm showed to be an appropriate technique to tests building-FIS and FIS-equipment interactions.

From the characterization tests, the rolling resistance of rolling surfaces with varying levels of damping-enhancing material (i.e., elastomeric rubber). It was concluded that this material significantly increases the rolling resistance of an RP bearing. However, increasing the thickness of rubber does not remarkably impact the rolling resistance of the rolling surfaces. Moreover, the rolling resistance was found to increase as the displacement of the bearing increased. Regarding other parameters studied, it was found that the system yields a higher gravitational restoring when supporting larger tributary loads. From the RTHS tests, it was found that when isolating low-frequency flexible equipment, the RP isolator unit performance is affected. In specific, it can be argued that for this case, the bearing's displacement decreases while its acceleration decreases when compared to cases in which the isolated equipment is more rigid. Lastly, this study found that an RP-based FIS—of about 5% the mass of a structural floor—did not affect the building response to ground excitations.

6.2 Future Work

This research proposes an innovative approach to evaluate FISs—through implementing RTHS. It was center centered around measuring the behavior and performance of an RP-bearing under uni-axial loading. As a continuation of this research, the following are several areas which have the potential for further investigation:

- Multi-axial testing of multiple-bearing configurations. These may include but not be limited to bi-axial loading and incorporating vertical motions.

- Further study of FIS-equipment interactions through different approaches of modeling the isolated equipment.

- Further study of building-FIS interactions through study of a wider variety of pa-

rameters, as well as by incorporating a model of the RP isolator unit that captures FIS-equipment interactions too.

Bibliography

Almazán, J. L. and Llera, J. C. D. l. (2003). "Physical model for dynamic analysis of structures with fps isolators." *Earthquake Engineering & Structural Dynamics*, 32(8), 1157–1184. doi:10.1002/eqe.266.

ASCE (2010). *Minimum Design Loads for Buildings and Other Structures*. American Society of Civil Engineers (ASCE), Reston, VA, ASCE/SEI 7-10 edition.

ASCE (2017). *Minimum Design Loads and Associated Criteria for Buildings and Other Structures*. American Society of Civil Engineers (ASCE), Reston, VA, ASCE/SEI 7-16 edition.

ATC (2007). *Interim Testing Protocols for Determining the Seismic Performance Characteristics of Structural and Nonstructural Components* (June) FEMA 461, prepared by the Applied Technology Council (ATC) for the Federal Emergency Management Agency (FEMA), Washington, D.C.

Bin, P., Tehrani, M. H., Nisa, M., Harvey, Jr, P. S., and Taflanidis, A. A. (n.d.). "Analysis and optimization of a nonlinear dual-mode floor isolation system subjected to earthquake excitations." *Earthquake Engineering & Structural Dynamics* in press, doi: 10.1002/eqe.3449.

Bouc, R. (1971). "Modele mathematique d'hysteresis." *Acustica*, 24, 16–25 (in French).

Building Seismic Safety Council (2007). *Interim Testing Protocols for Determining the Seismic Performance Characteristics of Structural and Nonstructural Components*. FEMA, Washington, D.C.

Cao, L., Marullo, T., Al-Subaihawi, S., Kolay, C., Amer, A., Ricles, J., Sause, R., and Kusko, C. S. (2020). "Nheri lehigh experimental facility with large-scale multi-directional hybrid simulation testing capabilities." *Frontiers in Built Environment*, 6, 107. doi:10.3389/fbuil.2020.00107.

Chen, C. and Ricles, J. M. (2008). "Development of direct integration algorithms for structural dynamics using discrete control theory." *Journal of Engineering Mechanics*, 134(8), 676–683. doi:10.1061/(ASCE)0733-9399(2008)134:8(676).

Chen, C., Ricles, J. M., Marullo, T. M., and Mercan, O. (2009). "Real-time hybrid testing using the unconditionally stable explicit cr integration algorithm." *Earthquake Engineering & Structural Dynamics*, 38(1), 23–44. doi:10.1002/eqe.838.

Cilsalar, H. and Constantinou, M. C. (2019). "Behavior of a spherical deformable rolling seismic isolator for lightweight residential construction." *Bulletin of Earthquake Engineering*, 17(7), 4321–4345. doi:10.1007/s10518-019-00626-z.

Deringöl, A. H. and Güneyisi, E. M. (2019). "Effect of friction pendulum bearing properties on behaviour of buildings subjected to seismic loads." *Soil Dynamics and Earthquake Engineering*, 125, 105746. doi:10.1016/j.soildyn.2019.105746.

Fenz, D. M. and Constantinou, M. C. (2006). "Behaviour of the double concave friction pendulum bearing." *Earthquake Engineering & Structural Dynamics*, 35(11), 1403–1424. doi:10.1002/eqe.589.

Gavin, H. P. (2013). "Digital signal processing using the fast fourier transform, <http://people.duke.edu/ hpgavin/SystemID/CourseNotes/ftdsp.pdf>.

Harvey, Jr., P. S. (2015). "Vertical accelerations in rolling isolation systems: Experiments and simulations." *Journal of Engineering Mechanics*, 142(3), 04015091. doi:10.1061/(ASCE)EM.1943-7889.0001017.

Harvey, Jr., P. S. and Gavin, H. P. (2013). "The nonholonomic and chaotic nature of a rolling isolation system." *Journal of Sound and Vibration*, 332, 3535–3551. doi:10.1016/j.jsv.2013.01.036.

Harvey, Jr., P. S. and Gavin, H. P. (2014). "Truly isotropic biaxial hysteresis with arbitrary knee sharpness." *Earthquake Engineering and Structural Dynamics*, 43, 2051–2057. doi:10.1002/eqe.2436.

Harvey, Jr., P. S. and Kelly, K. C. (2016). "A review of rolling-type seismic isolation: Historical development and future directions." *Engineering Structures*, 125, 521–531. doi:10.1016/j.engstruct.2016.07.031.

Harvey, Jr., P. S., Zéhil, G.-P., and Gavin, H. P. (2014). "Experimental validation of simplified models for rolling isolation systems." *Earthquake Engineering and Structural Dynamics*, 43, 1067–1088. doi:10.1002/eqe.2387.

Horiuchi, T., Inoue, M., Konno, T., and Namita, Y. (1999). "Real-time hybrid experimental system with actuator delay compensation and its application to a piping system with energy absorber." *Earthquake Engineering & Structural Dynamics*, 28(10), 1121–1141. doi:10.1002/(SICI)1096-9845(199910)28:10⟨1121::AID-EQE858⟩3.0.CO;2-O.

IEEE Standard 693 (2016). *IEEE Recommended Practice for Seismic Design of Substations*. Institute of Electrical and Electronic Engineers, Inc.

Ismail, M., Rodellar, J., and Ikhouane, F. (2010). "An innovative isolation device for aseismic design." *Engineering Structures*, 32, 1168–1183. doi:10.1016/j.engstruct.2009.12.043.

Jia, G., Gidaris, I., Taflanidis, A. A., and Mavroeidis, G. P. (2014). "Reliability-based assessment/design of floor isolation systems." *Engineering Structures*, 78, 41–56. doi:10.1016/j.engstruct.2014.07.031.

Kolay, C., Marullo, T. M., Al-Subaihawi, S., and Ricles, J. (2018). "HybridFEM-MH: A program for nonlinear dynamic analysis and real-time hybrid simulation of civil infrastructure systems subject to multi-hazards." *Report No. ATLSS Report No. 18-06*, ATLSS. HybridFEM-MH Version 2.0 User's Manual.

Kolay, C. and Ricles, J. M. (2014). "Development of a family of unconditionally stable explicit direct integration algorithms with controllable numerical energy dissipation." *Earthquake Engineering and Structural Dynamics*, 43(9), 1361–1380. doi:10.1002/eqe.2401.

Kolay, C. and Ricles, J. M. (2016). "Assessment of explicit and semi-explicit classes of model-based algorithms for direct integration in structural dynamics." *International Journal for Numerical Methods in Engineering*, 107(1), 49–73. doi:10.1002/nme.5153.

Kolay, C. and Ricles, J. M. (2019). "Improved explicit integration algorithms for structural dynamic analysis with unconditional stability and controllable numerical dissipation." *Journal of Earthquake Engineering*, 23(5), 771–792. doi:10.1080/13632469.2017.1326423.

Kolay, C., Ricles, J. M., Marullo, T. M., Mahvashmohammadi, A., and Sause, R. (2015). "Implementation and application of the unconditionally stable explicit parametrically dissipative kr-α method for real-time hybrid simulation." *Earthquake Engineering and Structural Dynamics*, 44(5), 735–755. doi:10.1002/eqe.2484.

Mahin, S. A. and Shing, P. B. (1985). "Pseudodynamic method for seismic testing." *Journal of Structural Engineering*, 111(7), 1482–1503. doi:10.1061/(ASCE)0733-9445(1985)111:7(1482).

Mokha, A., Constantinou, M. C., Reinhorn, A. M., and Zayas, V. A. (1991). "Experimental study of friction‐pendulum isolation system." *Journal of Structural Engineering*, 117(4), 1201–1217. doi:10.1061/(ASCE)0733-9445(1991)117:4(1201).

Nakashima, M. (2020). "Hybrid simulation: An early history." *Earthquake Engineering & Structural Dynamics*, 49(10), 949–962. doi:10.1002/eqe.3274.

Nakashima, M., Kato, H., and Takaoka, E. (1992). "Development of real-time pseudo dynamic testing." *Earthquake Engineering & Structural Dynamics*, 21(1), 79–92. doi:10.1002/eqe.4290210106.

Ohtori, Y., Christenson, R. E., Spencer, Jr., B. F., and Dyke, S. J. (2004). "Benchmark control problems for seismically excited nonlinear buildings." *Journal of Engineering Mechanics*, 130, 366–385. doi:10.1061/(ASCE)0733-9399(2004)130:4(366).

Sarlis, A. A. and Constantinou, M. C. (2016). "A model of triple friction pendulum bearing for general geometric and frictional parameters." *Earthquake Engineering & Structural Dynamics*, 45(11), 1837–1853. doi:10.1002/eqe.2738.

Shao, X. and Griffith, C. (2013). "An overview of hybrid simulation implementations in NEES projects." *Engineering Structures*, 56, 1439–1451. doi:https://doi.org/10.1016/j.engstruct.2013.07.008.

Solovyov, A., Semenov, M., Meleshenko, P., and Barsukov, A. (2017). "Bouc-wen model of hysteretic damping." *Procedia Engineering*, 201, 549 – 555 3rd International Conference "Information Technology and Nanotechnology, doi:https://doi.org/10.1016/j.proeng.2017.09.605.

Takanashi, K., Udagawa, K., Seki, M., Okada, T., and Tanaka, H. (1975). "Non-linear earthquake response analysis of structures by a computer-actuator on-line system." *Report No. 8*, Bulletin of Earthquake Resistant Structure Research Center, Institute of Industrial Science, University of Tokyo, Tokyo, Japan.

Tehrani, M. H. and Harvey, Jr., P. S. (2019). "Enhanced passive control of dual-mode systems under extreme seismic loading: an optimal control approach." *Structural Control and Health Monitoring*, 26(7), e2367. doi:10.1002/stc.2367.

Telcordia (2012). *NEBS Requirements: Physical Protection*. Number GR-63-CORE. Telcordia Technologies, Inc., Piscataway, NJ.

Touaillon, J. (1870). "Improvement of buildings (February 15). US Patent No. 99973.

Vargas, R. and Bruneau, M. (2009). "Experimental response of buildings designed with metallic structural fuses. II." *Journal of Structural Engineering*, 135, 394–403. doi:10.1061/(ASCE)0733-9445(2009)135:4(394).

Wang, S.-J., Yu, C.-H., Lin, W.-C., Hwang, J.-S., and Chang, K.-C. (2017). "A generalized analytical model for sloped rolling-type seismic isolators." *Engineering Structures*, 138, 434 – 446. doi:10.1016/j.engstruct.2016.12.027.

Warn, G. P. and Ryan, K. L. (2012). "A review of seismic isolation for buildings: Historical development and research needs." *Buildings*, 2, 300–325. doi:10.3390/buildings2030300.

Wilcoski, J., Gambill, J. B., and Smith, S. J. (1997). "The CERL equipment fragility and protection procedure (CEFAPP): Experimental definition of equipment vulnerability to transient support motions." *Report No. USACERL Technical Report 97/58*, U.S. Army Construction Engineering Research Laboratories (USACERL), <https://apps.dtic.mil/sti/pdfs/ADA342277.pdf>.

Zhang, R., Phillips, B. M., Taniguchi, S., Ikenaga, M., and Ikago, K. (2017). “Shake table real-time hybrid simulation techniques for the performance evaluation of buildings with inter-story isolation.” *Structural Control and Health Monitoring*, 24(10), e1971. doi:10.1002/stc.1971.

Appendix A
Results of Characterization Tests

In this chapter, an exhaustive portrayal of all the characterization test results are included.

A.1 Conical Rolling Surfaces

A.1.1 240-lb Payload

A.1.1(a) 0.5-Hz Characterization Wave

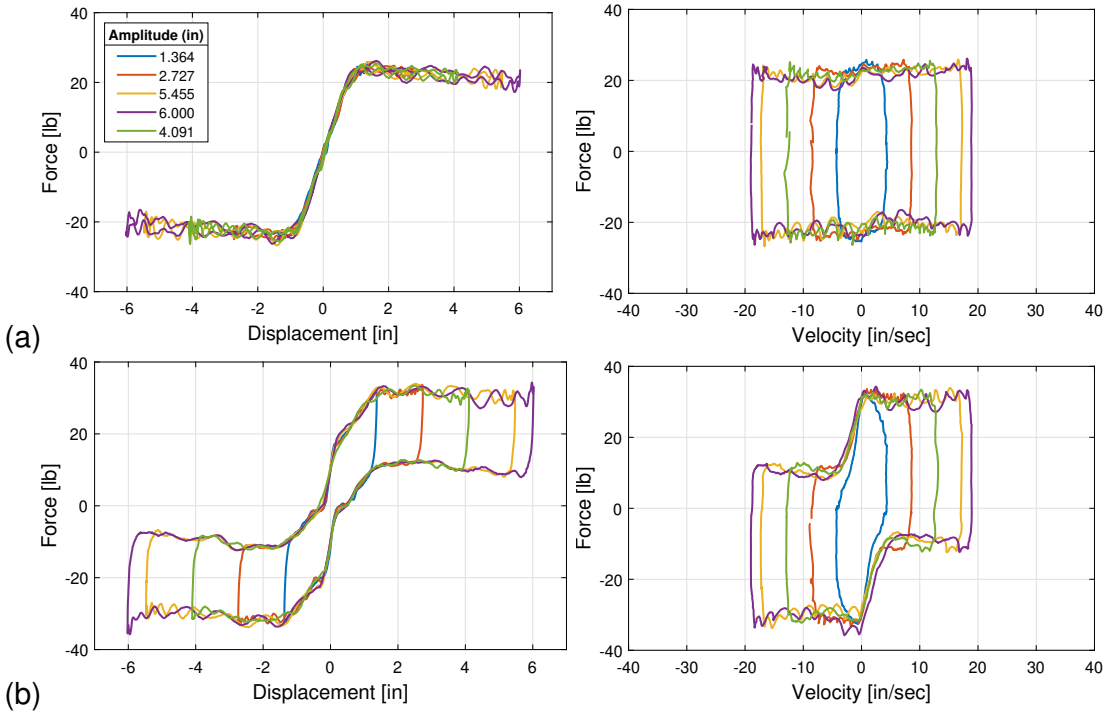

Figure A.1: Load-deflection (left) and load-velocity (right) relationships of specimens (a) C0-240, (b) CN-240, (c) C1-240, (d) C2-240, and (e) C3-240 subject to 0.5-Hz characterization wave.

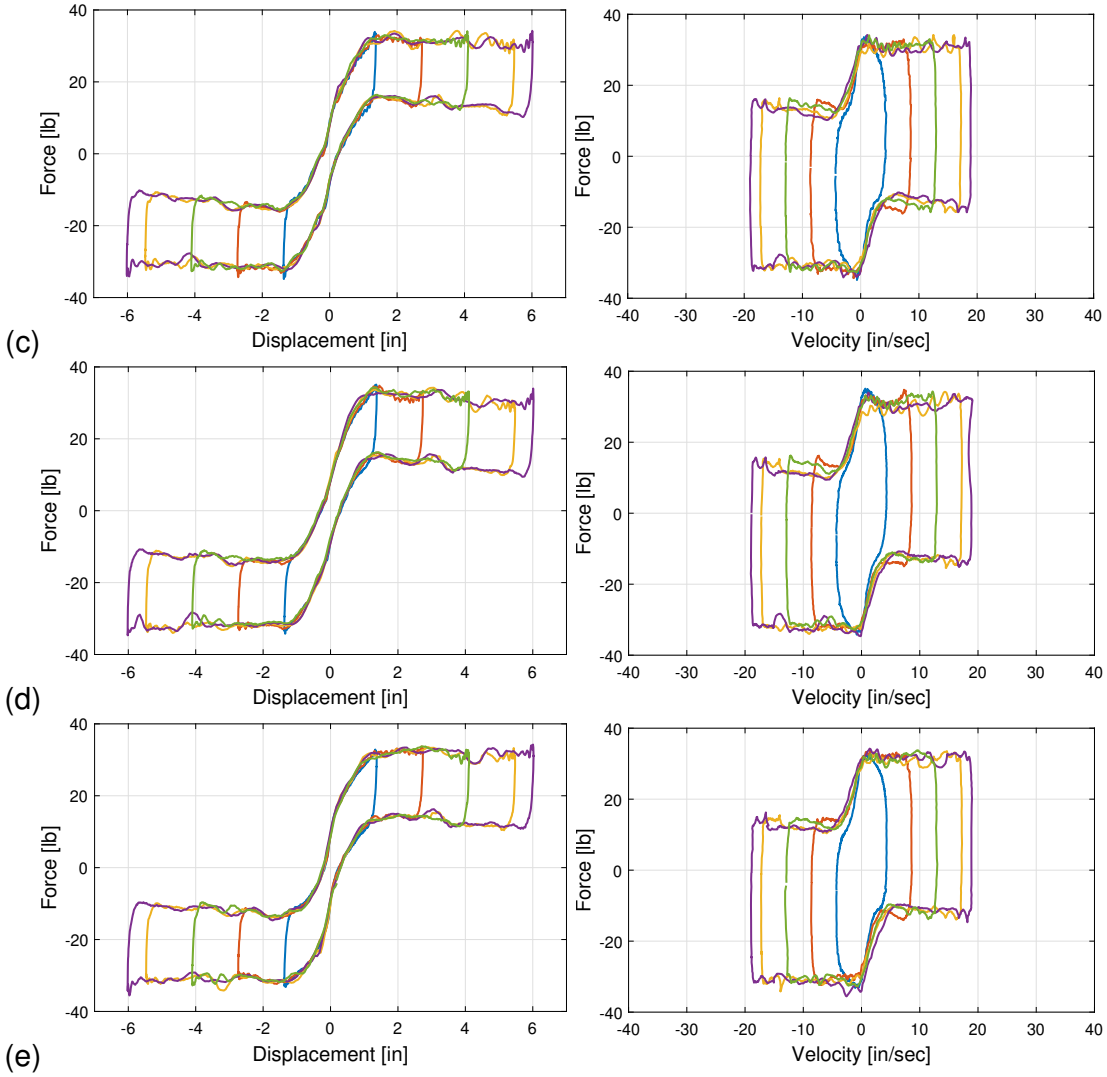

Figure A.1 (cont.): Load-deflection (left) and load-velocity (right) relationships of specimens (a) C0-240, (b) CN-240, (c) C1-240, (d) C2-240, and (e) C3-240 subject to 0.5-Hz characterization wave.

A.1.1(b) 1-Hz Characterization Wave

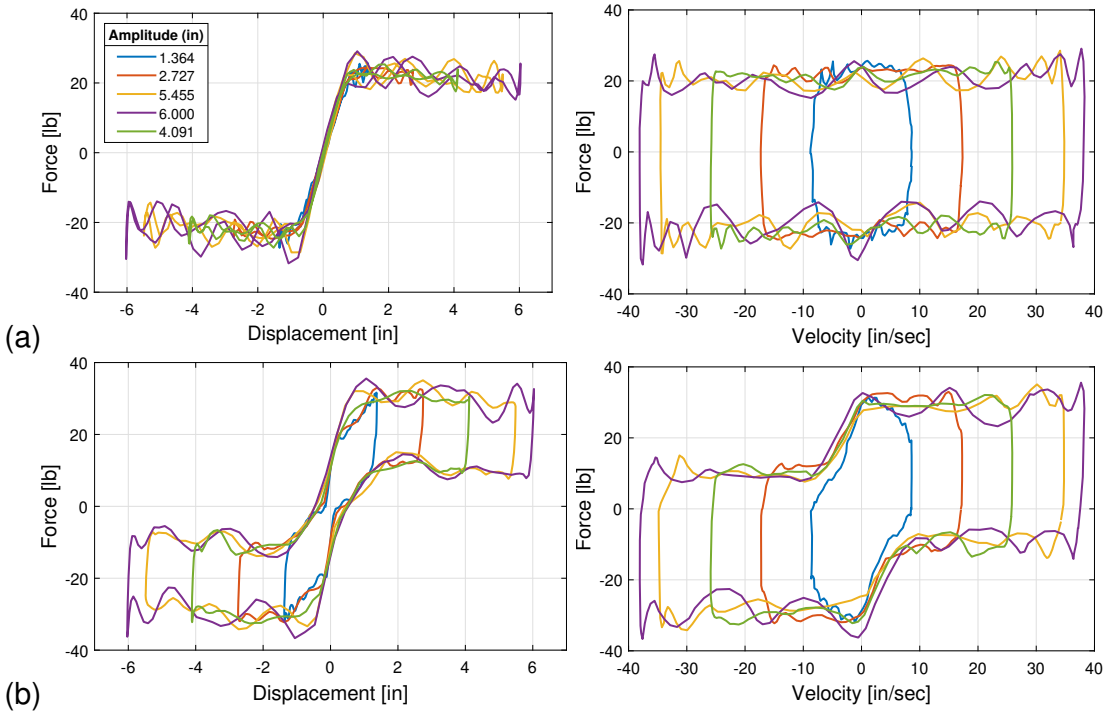

Figure A.2: Load-deflection (left) and load-velocity (right) relationships of specimens (a) C0-240, (b) CN-240, (c) C1-240, (d) C2-240, and (e) C3-240 subject to 1.0-Hz characterization wave.

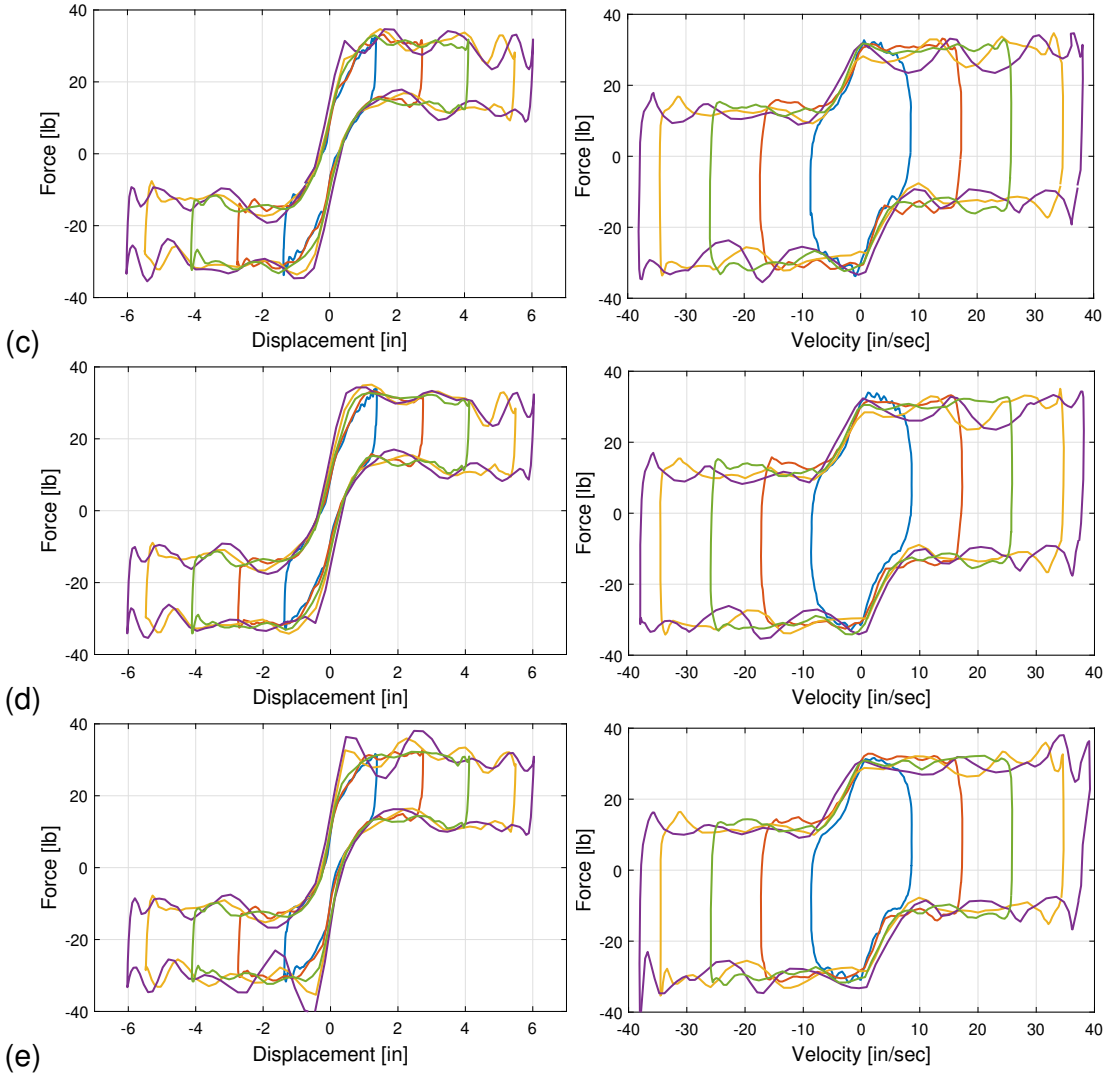

Figure A.2 (cont.): Load-deflection (left) and load-velocity (right) relationships of specimens (a) C0-240, (b) CN-240, (c) C1-240, (d) C2-240, and (e) C3-240 subject to 1.0-Hz characterization wave.

A.1.2 143-lb Payload

A.1.2(a) 0.5-Hz Characterization Wave

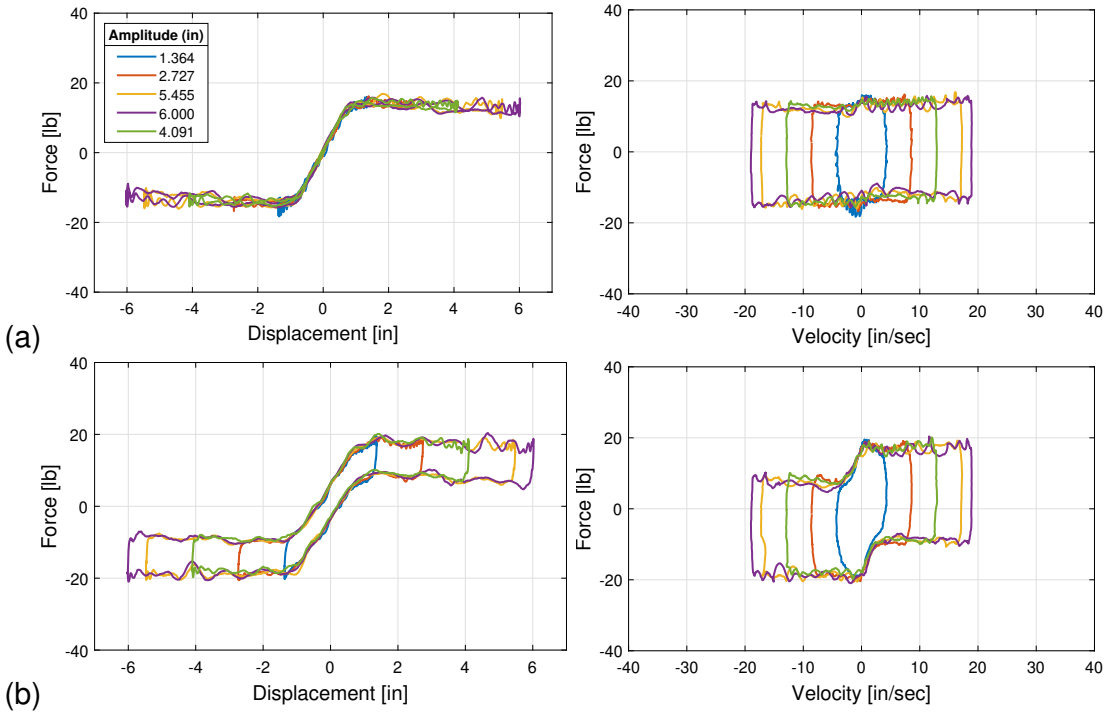

Figure A.3: Load-deflection (left) and load-velocity (right) relationships of specimens (a) C0-143, (b) CN-143, (c) C1-143, (d) C2-143, and (e) C3-143 subject to 0.5-Hz characterization wave.

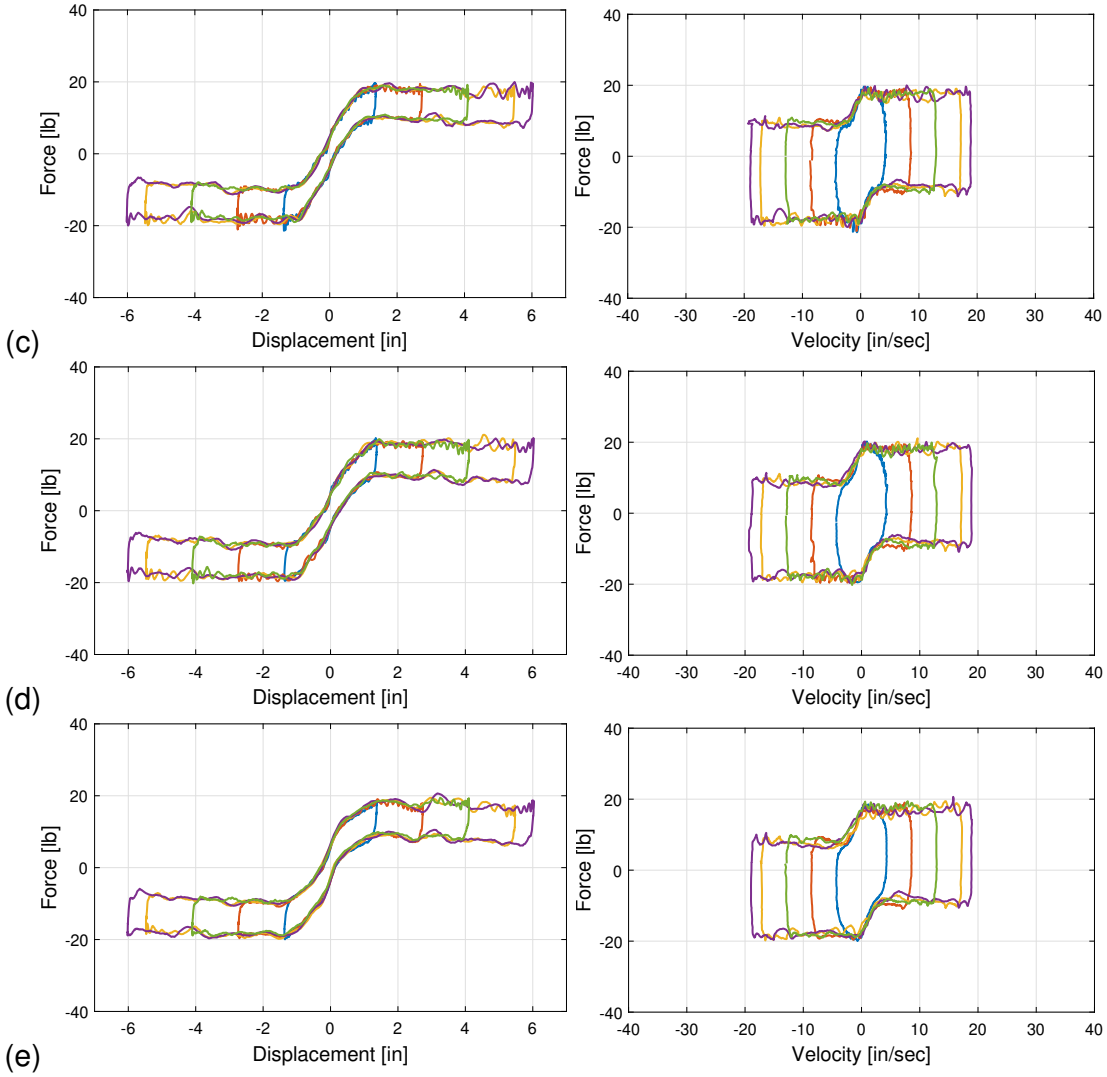

Figure A.3 (cont.): Load-deflection (left) and load-velocity (right) relationships of specimens (a) C0-143, (b) CN-143, (c) C1-143, (d) C2-143, and (e) C3-143 subject to 0.5-Hz characterization wave.

A.1.2(b) 1-Hz Characterization Wave

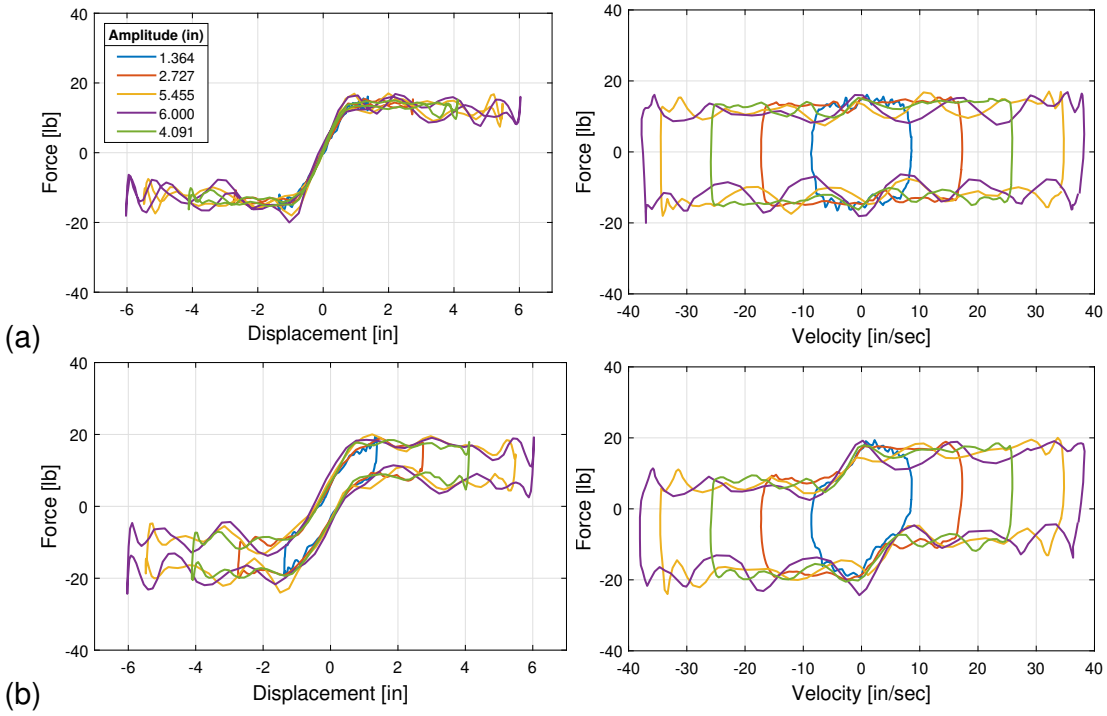

Figure A.4: Load-deflection (left) and load-velocity (right) relationships of specimens (a) C0-143, (b) CN-143, (c) C1-143, (d) C2-143, and (e) C3-143 subject to 1-Hz characterization wave.

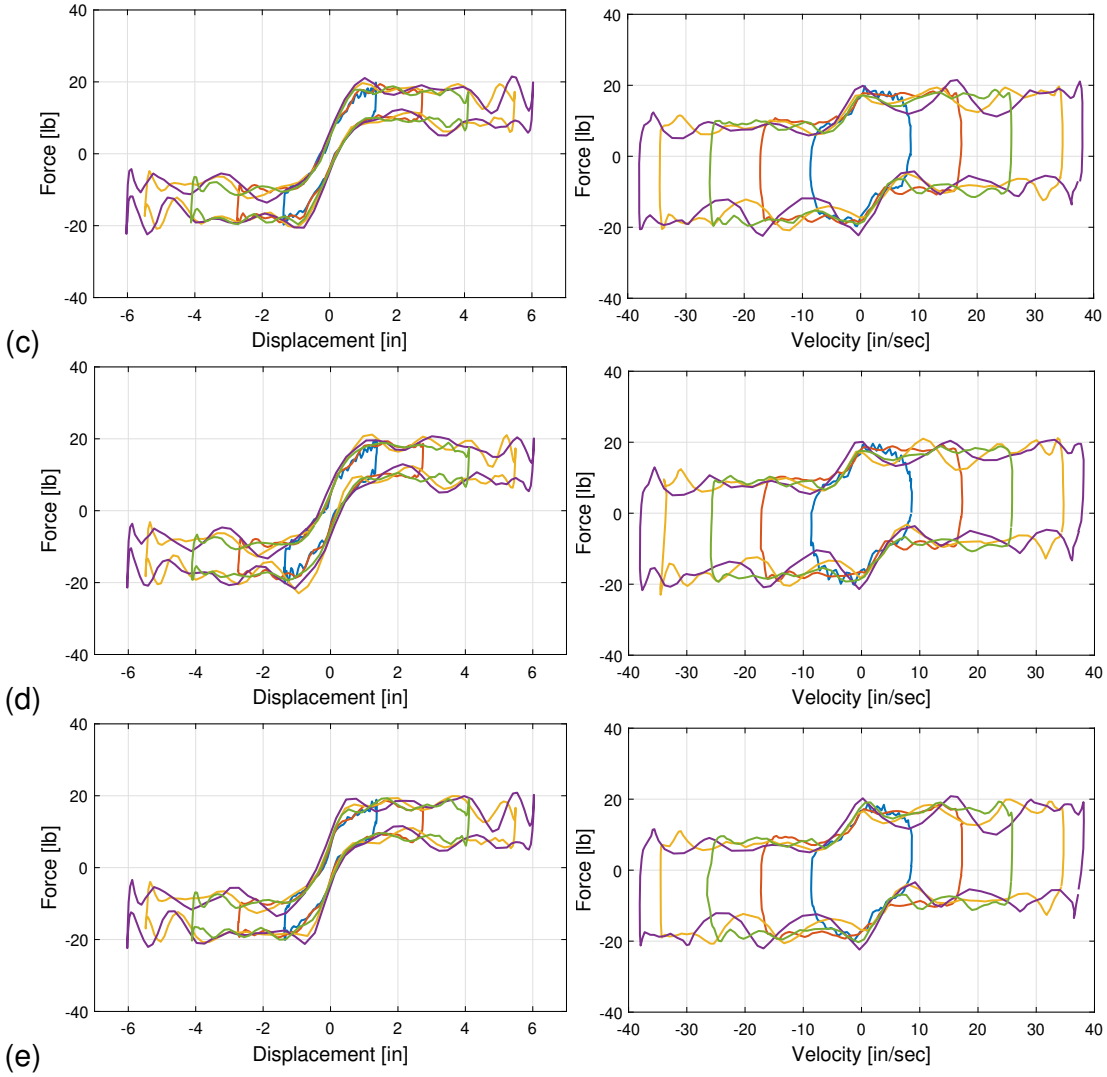

Figure A.4 (cont.): Load-deflection (left) and load-velocity (right) relationships of specimens (a) C0-143, (b) CN-143, (c) C1-143, (d) C2-143, and (e) C3-143 subject to 1-Hz characterization wave.

A.2 Flat Rolling Surfaces

A.2.1 143-lb Payload

A.2.1(a) 0.5-Hz Characterization Wave

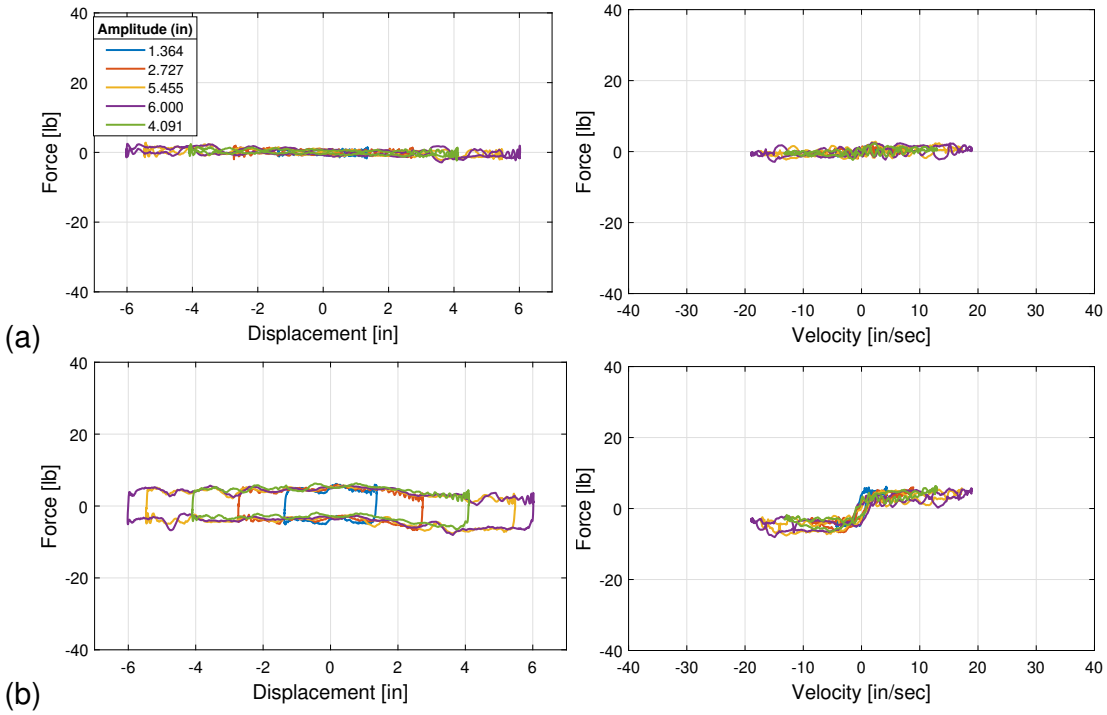

Figure A.5: Load-deflection (left) and load-velocity (right) relationships of specimens (a) F0-143, (b) F1-143, (c) F2-143, (d) F3-143, and (e) F4-143 subject to 0.5-Hz characterization wave.

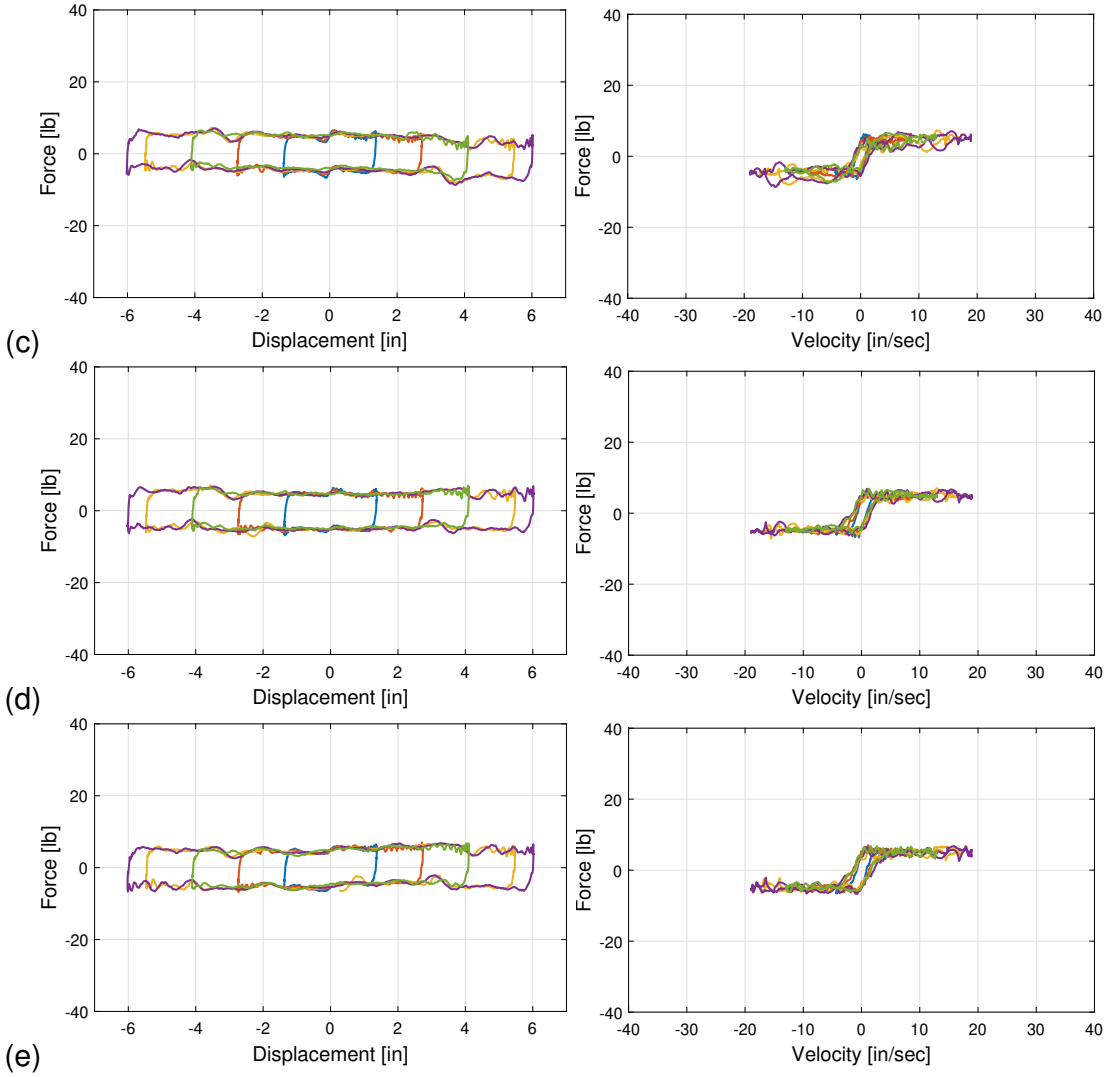

Figure A.5 (cont.): Load-deflection (left) and load-velocity (right) relationships of specimens (a) F0-143, (b) F1-143, (c) F2-143, (d) F3-143, and (e) F4-143 subject to 0.5-Hz characterization wave.

A.2.1(b) 1-Hz Characterization Wave

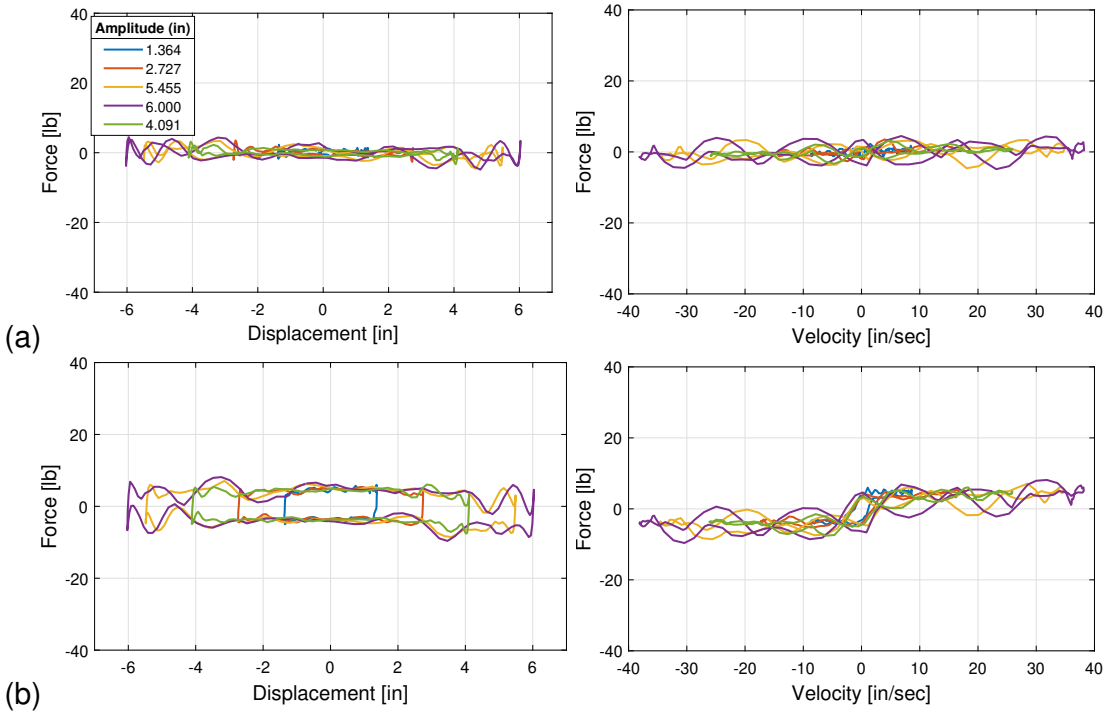

Figure A.6: Load-deflection (left) and load-velocity (right) relationships of specimens (a) F0-143, (b) F1-143, (c) F2-143, (d) F3-143, and (e) F4-143 subject to 1-Hz characterization wave.

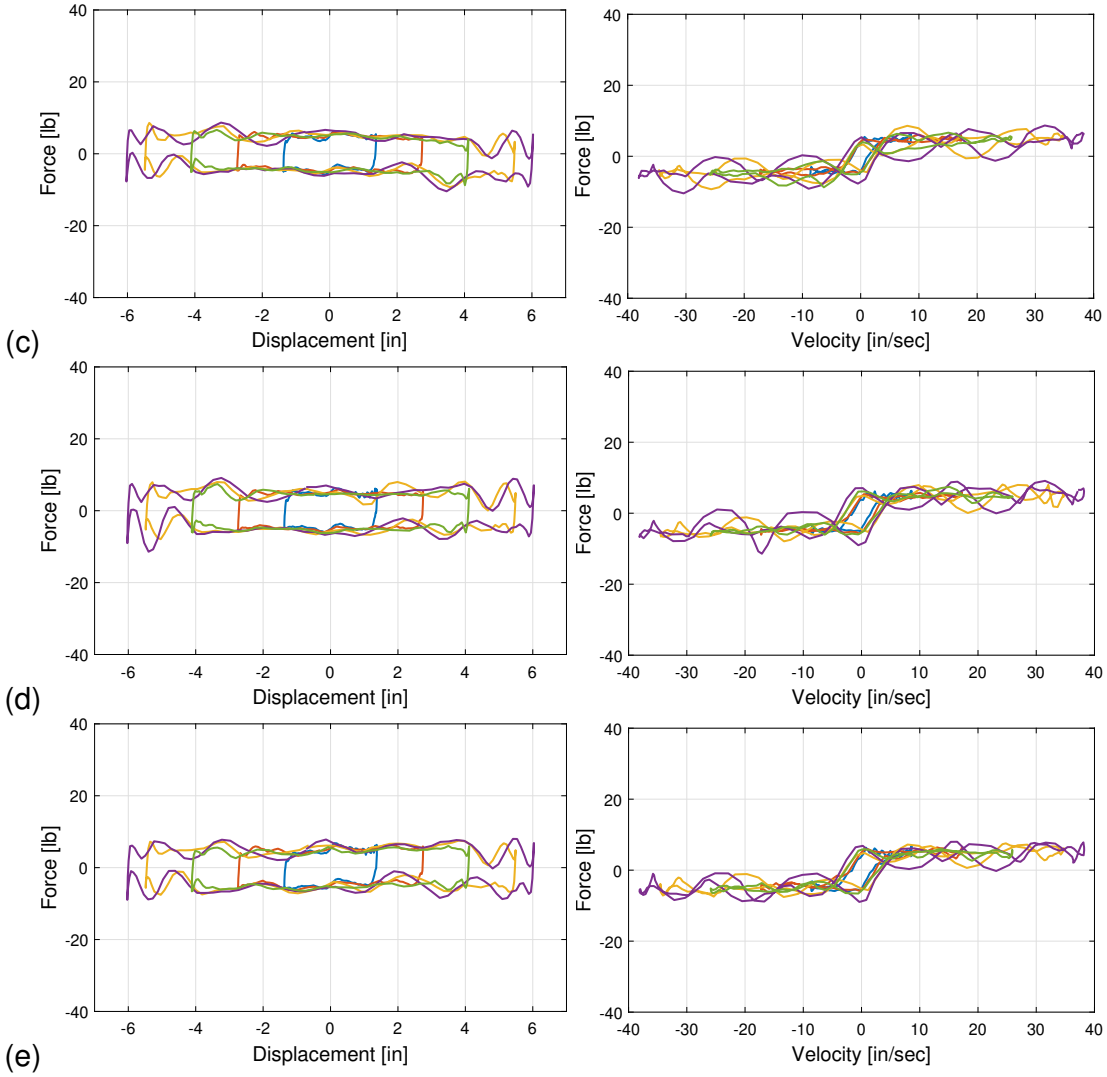

Figure A.6 (cont.): Load-deflection (left) and load-velocity (right) relationships of specimens (a) F0-143, (b) F1-143, (c) F2-143, (d) F3-143, and (e) F4-143 subject to 1-Hz characterization wave.

A.3 VERTEQ-II Results

A.3.1 143-lb Payload

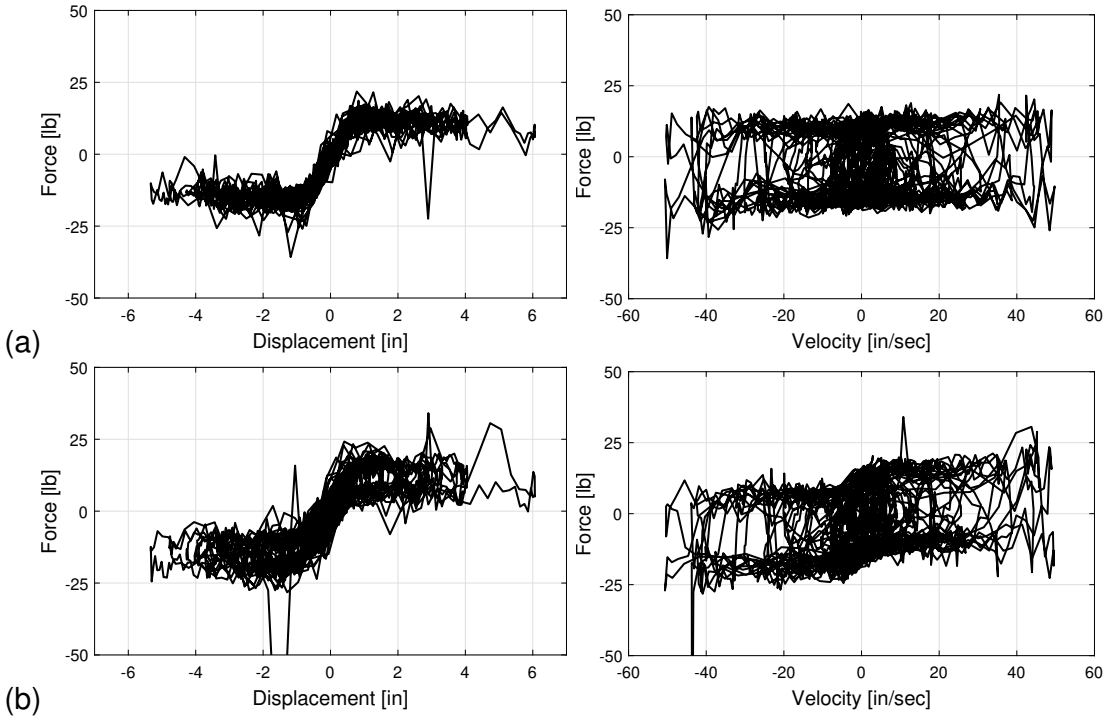

Figure A.7: Load-deflection (left) and load-velocity (right) relationships of specimens (a) F0-143, (b) F1-143, (c) F2-143, (d) F3-143, and (e) F4-143 subject to VERTEQ-II characterization wave

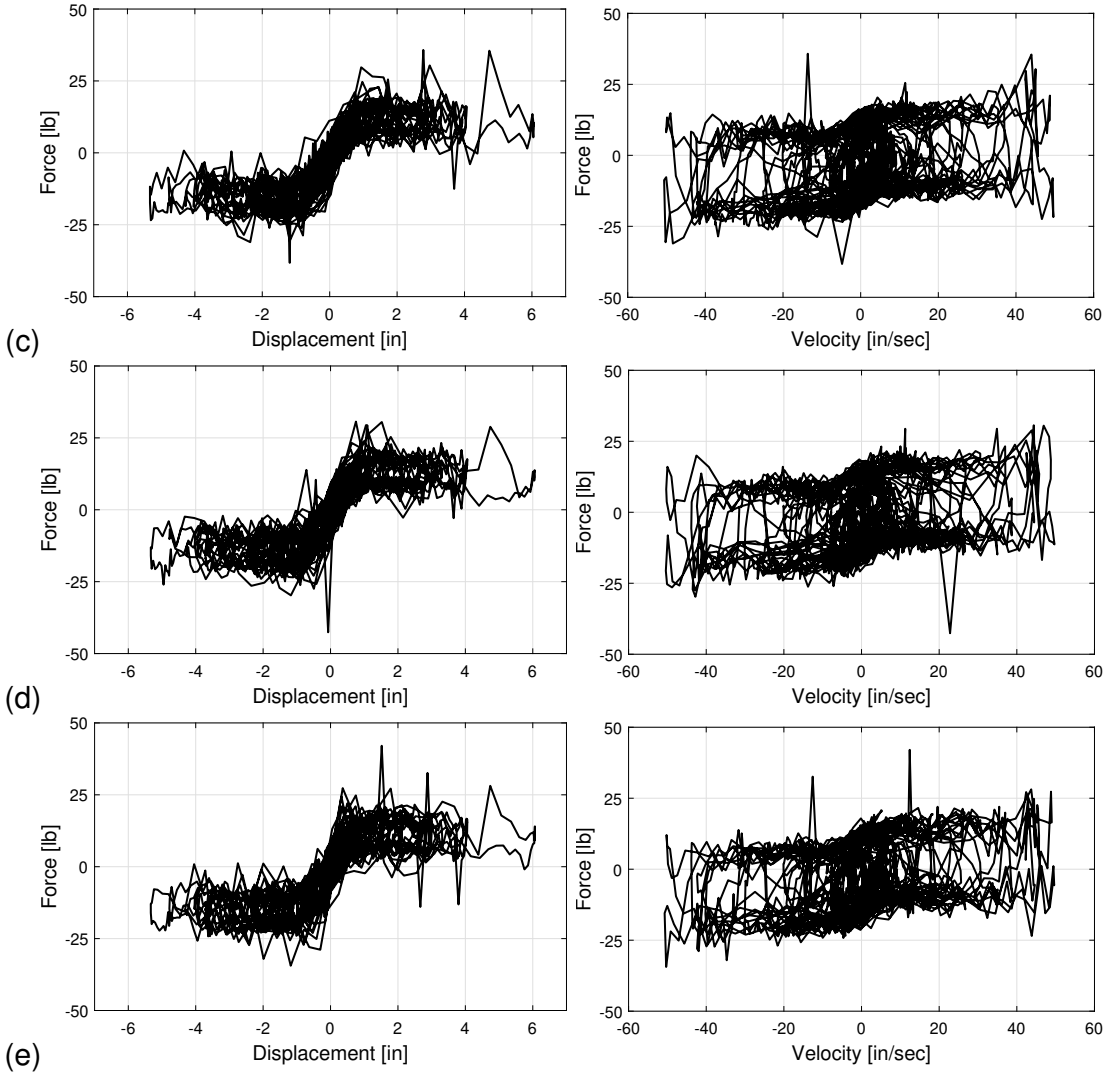

Figure A.7 (cont.): Load-deflection (left) and load-velocity (right) relationships of specimens (a) F0-143, (b) F1-143, (c) F2-143, (d) F3-143, and (e) F4-143 subject to VERTEQ-II characterization wave

A.3.2 240-lb Payload

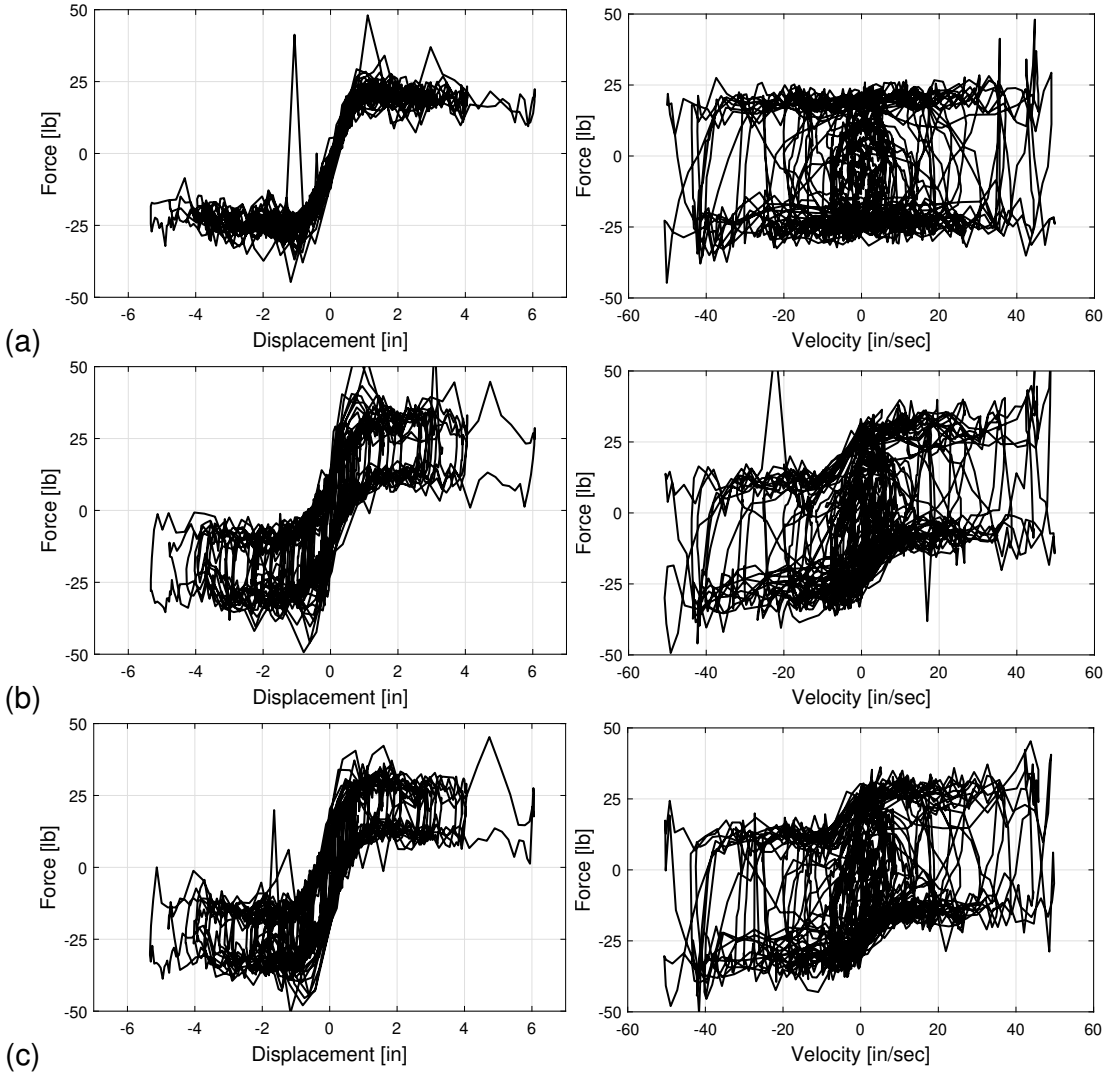

Figure A.8: Load-deflection (left) and load-velocity (right) relationships of specimens (a) F0-143, (b) F1-143, (c) F2-143, (d) F3-143, and (e) F4-143 subject to VERTEQ-II characterization wave

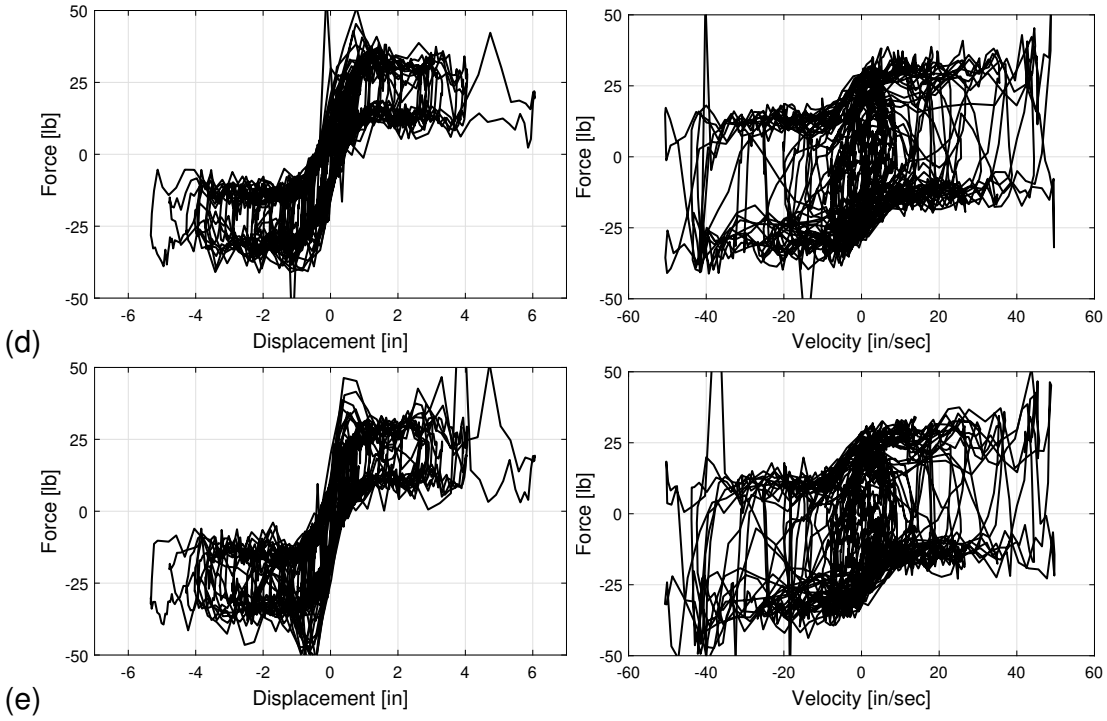

Figure A.8 (cont.): Load-deflection (left) and load-velocity (right) relationships of specimens (a) F0-143, (b) F1-143, (c) F2-143, (d) F3-143, and (e) F4-143 subject to VERTEQ-II characterization wave